



UNIVERSIDAD DE INVESTIGACIÓN DE TECNOLOGÍA EXPERIMENTAL YACHAY

Escuela de Ciencias Físicas y Nanotecnología

**TÍTULO: First-principles studies of the electronic and
mechanical properties of α -Al/ γ -Al₂O₃(111) multilayer
composite**

Trabajo de integración curricular presentado como requisito para la
obtención del título de Físico

Autor:

Vásconez López Edwin Marcelo

Tutor:

Ph.D Pinto Esparza Henry Paúl

Urcuquí, abril 2020

SECRETARÍA GENERAL
(Vicerrectorado Académico/Cancillería)
ESCUELA DE CIENCIAS FÍSICAS Y NANOTECNOLOGÍA
CARRERA DE FÍSICA
ACTA DE DEFENSA No. UITEY-PHY-2020-00006-AD

A los 21 días del mes de abril de 2020, a las 16:00 horas, de manera virtual mediante videoconferencia, y ante el Tribunal Calificador, integrado por los docentes:

Presidente Tribunal de Defensa	Dra. GONZALEZ VAZQUEZ, GEMA , Ph.D.
Miembro No Tutor	Dr. VACACELA GOMEZ, CRISTIAN ISAAC , Ph.D.
Tutor	Dr. PINTO ESPARZA, HENRY PAUL , Ph.D.

El(la) señor(ita) estudiante **VASCONEZ LOPEZ, EDWIN MARCELO**, con cédula de identidad No. **1804855631**, de la **ESCUELA DE CIENCIAS FÍSICAS Y NANOTECNOLOGÍA**, de la Carrera de **FÍSICA**, aprobada por el Consejo de Educación Superior (CES), mediante Resolución **RPC-SO-39-No.456-2014**, realiza a través de videoconferencia, la sustentación de su trabajo de titulación denominado: **First-principles studies of the electronic and mechanical properties of -Al/ -Al₂O₃ (111) multilayer composite**, previa a la obtención del título de **FÍSICO/A**.

El citado trabajo de titulación, fue debidamente aprobado por el(los) docente(s):

Tutor	Dr. PINTO ESPARZA, HENRY PAUL , Ph.D.
--------------	---------------------------------------

Y recibió las observaciones de los otros miembros del Tribunal Calificador, las mismas que han sido incorporadas por el(la) estudiante.

Previamente cumplidos los requisitos legales y reglamentarios, el trabajo de titulación fue sustentado por el(la) estudiante y examinado por los miembros del Tribunal Calificador. Escuchada la sustentación del trabajo de titulación a través de videoconferencia, que integró la exposición de el(la) estudiante sobre el contenido de la misma y las preguntas formuladas por los miembros del Tribunal, se califica la sustentación del trabajo de titulación con las siguientes calificaciones:

Tipo	Docente	Calificación
Presidente Tribunal De Defensa	Dra. GONZALEZ VAZQUEZ, GEMA , Ph.D.	9,8
Tutor	Dr. PINTO ESPARZA, HENRY PAUL , Ph.D.	10,0
Miembro Tribunal De Defensa	Dr. VACACELA GOMEZ, CRISTIAN ISAAC , Ph.D.	9,8

Lo que da un promedio de: **9.9 (Nueve punto Nueve)**, sobre 10 (diez), equivalente a: **APROBADO**

Para constancia de lo actuado, firman los miembros del Tribunal Calificador, el/la estudiante y el/la secretario ad-hoc.

Certifico que *en cumplimiento del Decreto Ejecutivo 1017 de 16 de marzo de 2020, la defensa de trabajo de titulación (o examen de grado modalidad teórico práctica) se realizó vía virtual, por lo que las firmas de los miembros del Tribunal de Defensa de Grado, constan en forma digital.*

VASCONEZ LOPEZ, EDWIN MARCELO
Estudiante



Firmado electrónicamente por:

**GEMA
 GONZALEZ**

Dra. GONZÁLEZ VAZQUEZ, GEMA , Ph.D.

Presidente Tribunal de Defensa



Firmado electrónicamente por:

**HENRY PAUL
 PINTO**

Dr. PINTO ESPARZA, HENRY PAUL , Ph.D.

Tutor



Firmado Digitalmente por: EDWIN MARCELO
 VASCONEZ LOPEZ
 Hora oficial Ecuador: 08/07/2020 23:39



Firmado electrónicamente por:
**CRISTIAN ISAAC
VACACELA GOMEZ**

Dr. VACACELA GOMEZ, CRISTIAN ISAAC , Ph.D.
Miembro No Tutor



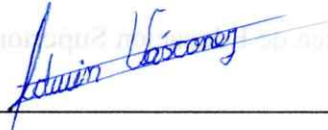
Firmado electrónicamente por:
**EVELYN CAROLINA
CIFUENTES TAFUR**

CIFUENTES TAFUR, EVELYN CAROLINA
Secretario Ad-hoc

AUTORÍA

Yo, **Edwin Marcelo Vásconez López**, con cédula de identidad 1804855631, declaro que las ideas, juicios, valoraciones, interpretaciones, consultas bibliográficas, definiciones y conceptualizaciones expuestas en el presente trabajo; así como, los procedimientos y herramientas utilizadas en la investigación, son de absoluta responsabilidad de el/la autora (a) del trabajo de integración curricular. Así mismo, me acojo a los reglamentos internos de la Universidad de Investigación de Tecnología Experimental Yachay.

Urcuquí, abril 2020.



Edwin Marcelo Vásconez López

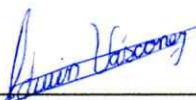
CI: 1804855631

AUTORIZACIÓN DE PUBLICACIÓN

Yo, **Edwin Marcelo Vásconez López**, con cédula de identidad 1804855631, cedo a la Universidad de Tecnología Experimental Yachay, los derechos de publicación de la presente obra, sin que deba haber un reconocimiento económico por este concepto. Declaro además que el texto del presente trabajo de titulación no podrá ser cedido a ninguna empresa editorial para su publicación u otros fines, sin contar previamente con la autorización escrita de la Universidad.

Asimismo, autorizo a la Universidad que realice la digitalización y publicación de este trabajo de integración curricular en el repositorio virtual, de conformidad a lo dispuesto en el Art. 144 de la Ley Orgánica de Educación Superior

Urcuquí, abril 2020.



Edwin Marcelo Vásconez López

CI: 1804855631

Agradecimiento

I acknowledge my advisor Henry Pinto for his recommendations, support, and especially for his confidence in me. I am grateful to my friends, who were my emotional support. Agradezco a mis padres Nicolay y Nelly, a mi hermana Nicole y a toda mi familia en general, por brindarme siempre su apoyo y fuerzas para seguir adelante.

Edwin Marcelo Vásquez López

Resumen

La fase γ -Alúmina (γ -Al₂O₃) se utiliza en las industrias electrónicas, automotrices y de catálisis debido a sus interesantes propiedades electrónicas y mecánicas. Estudios recientes encontraron que la multicapa α -Aluminio/ γ -Alúmina (α -Al/ γ -Al₂O₃) muestra una mejora de sus propiedades mecánicas en comparación con capas individuales. Sin embargo, la estructura atómica real de γ -Al₂O₃ es poco conocida y ha motivado una gran cantidad de estudios experimentales y teóricos. La presente investigación comenzó considerando la estructura sólida de γ -Al₂O₃ que ya se predijo utilizando la teoría del funcional de la densidad (DFT). Curiosamente, este modelo teórico predijo la descomposición de γ -Al₂O₃ (110) a nanofacetos (111) y esto ha sido verificado experimentalmente. El conocimiento sobre estas superficies se aplicó en la construcción de cuatro modelos atómicos para la multicapa α -Aluminio/ γ -Alúmina. El estudio consideró la reconstrucción de la interfase metal/óxido; cuya estructura se resolvió utilizando una simulación de recocido. Las propiedades electrónicas y mecánicas fueron calculadas para las estructuras multicapa más estables y se analizaron en base a los datos experimentales disponibles. Las propiedades electrónicas mostraron que el compuesto adquiere un comportamiento metálico. Las simulaciones presentadas en este trabajo predicen una mejora de las propiedades mecánicas en los modelos multicapa en buen acuerdo con los resultados experimentales.

Palabras Clave:

Estudios iniciales, Teoría de la densidad funcional, γ -Alúmina, Aluminio, Compuesto multicapa, interfaz.

Abstract

The γ -Alumina (γ -Al₂O₃) phase is mainly used in the catalysis, electronics and automotive industries due to its interesting electronic and mechanical properties. Recent experiments on multilayered α -Aluminum/ γ -Alumina (α -Al/ γ -Al₂O₃) are found to exhibit improvement of the mechanical properties in comparison with individual layers. However, the actual atomic structure of γ -Al₂O₃ is slightly known and has motivated a large number of experimental and theoretical studies. The proposed research will start considering the γ -Al₂O₃ bulk structure that was already predicted using density-functional theory (DFT). Interestingly, this theoretical model predicted the decomposition of the γ -Al₂O₃(110) surface to (111) nanofacets and has been already confirmed experimentally. The knowledge on these surfaces is applied in the construction of four atomic models for α -Al/ γ -Al₂O₃(111) multilayer. The study will consider the atomic interface reconstruction of the metal/oxide interface; which structure will be resolved using simulated annealing. The electronic and mechanical properties of the most stable multilayered structures obtained will be computed and analyzed in the light of available experimental data. The electronic properties showed that the composite acquires a metal-like behavior. The simulations presented in this work predict an enhancement of the mechanical properties in the multilayered models in good agreement with previous experimental results.

Keywords:

First-principles studies, Density-functional theory, γ -Alumina, Aluminum, Multilayer Composite, Interface.

Contents

List of Figures	viii
List of Tables	x
List of Papers	xi
1 Introduction	1
1.1 Problem Statement	2
1.2 General and Specific Objectives	2
1.3 Overview	3
2 Theoretical Background	5
2.1 Density Functional Theory	5
2.1.1 The Schrödinger equation	5
2.1.2 Born-Oppenheimer approximation	6
2.1.3 Hartree-Fock approximation	6
2.1.4 The Hohenberg-Kohn theorems	7
2.1.5 The Kohn-Sham equations	8
2.1.6 Self-consistent calculations	9
2.1.7 Exchange and correlation functionals	10
2.2 Computational methods	12
2.2.1 Periodic systems and plane waves	12
2.2.2 Pseudopotentials	14

2.2.3	Projector-augmented wave method	14
2.2.4	Computing the atomic forces and the Hellmann-Feymann theorem	15
2.2.5	<i>Ab initio</i> Molecular dynamics and simulating annealing	16
2.2.6	Introduction to VASP	16
2.3	The γ -Alumina Oxide	17
3	Methodology	21
3.1	Computational Details	21
3.1.1	Energy convergence and optimal parameters for VASP calculations	21
3.1.2	α -Al/ γ -Al ₂ O ₃ multilayer models	23
3.1.3	Mechanical properties	26
4	Results & Discussion	31
4.1	Bulk Structures	31
4.1.1	Structural and mechanical properties	31
4.1.2	Electronic properties	35
4.2	Interface Models	37
4.2.1	Structural and mechanical properties	37
4.2.2	Electronic properties	38
4.3	Theory versus Experiment	47
5	Conclusions & Outlook	49
A	Results of DFT calculations PDOS	51
	Bibliography	69
	Abbreviations	77

List of Figures

2.1	Kohn-Sham self-consistent process	10
2.2	γ -Al ₂ O ₃ monoclinic spinel-based model	18
2.3	γ -Al ₂ O ₃ (111) slabs	19
3.1	Convergence parameters for α -Al	22
3.2	Convergence parameters for γ -Al ₂ O ₃	22
3.3	Convergence parameters for α -Al/ γ -Al ₂ O ₃ (111) interface.	23
3.4	Initial configuration for the α -Al/ γ -Al ₂ O ₃ interface models	25
3.5	Knoop and Vickers Hardness tests	27
4.1	EOS and optimal primitive cell for α -Al.	32
4.2	EOS and optimal primitive cell for γ -Al ₂ O ₃	33
4.3	PDOS for α -Al and γ -Al ₂ O ₃	36
4.4	A1 model final atomic configuration and PDOS	39
4.5	A1 model electron charge density	40
4.6	A2 model final atomic configuration and PDOS	41
4.7	A2 model electron charge density	42
4.8	B1 model final atomic configuration and PDOS	43
4.9	B1 model electron charge density	44
4.10	B2 model final atomic configuration and PDOS.	45
4.11	B2 model electron charge density	46
4.12	Experimental and theoretical Al/Al ₂ O ₃ multilayers.	47

A.1	PDOS of the α -Aluminum (α -Al)	51
A.2	PDOS of the γ -Al ₂ O ₃ , Al contribution.	52
A.3	PDOS of the γ -Al ₂ O ₃ , O contribution.	53
A.4	PDOS of the interface A1, O contribution.	53
A.5	PDOS of the interface A1, Al _{α} contribution.	54
A.6	PDOS of the interface A1, Al _{γ} contribution.	54
A.7	PDOS of the interface A1, Al _{i} contribution.	55
A.8	PDOS of the interface A2, O contribution.	55
A.9	PDOS of the interface A2, Al _{α} contribution.	56
A.10	PDOS of the interface A2, Al _{γ} contribution.	56
A.11	PDOS of the interface A2, Al _{i} contribution.	57
A.12	PDOS of the interface B1, O contribution.	57
A.13	PDOS of the interface B1, Al _{α} contribution.	58
A.14	PDOS of the interface B1, Al _{γ} contribution.	58
A.15	PDOS of the interface B1, Al _{i} contribution.	59
A.16	PDOS of the interface B2, O contribution.	59
A.17	PDOS of the interface B2, Al _{α} contribution.	60
A.18	PDOS of the interface B2, Al _{γ} contribution.	60
A.19	PDOS of the interface B2, Al _{i} contribution.	61
A.20	Band structure α -Al	62
A.21	Band structure γ -Al ₂ O ₃	63
A.22	Band structure of the final A1 interface model	64
A.23	Band structure of the final A2 interface	65
A.24	Band structure of the final B1 interface	66
A.25	Band structure of the final B2 interface.	67

List of Tables

2.1	Surface energies for γ -Al ₂ O ₃ slabs	19
3.1	Optimal parameters for α -Al, γ -Al ₂ O ₃ and α -Al/ γ -Al ₂ O ₃ (111).	23
3.2	Crystallographic data for the initial configuration of the interface models	24
3.3	Hardnees of different materials.	28
4.1	Crystallographic data for α -Al	32
4.2	Crystallographic data for γ -Al ₂ O ₃	34
4.3	Structural and mechanical data for computed α -Al and γ -Al ₂ O ₃	35
4.4	PBEsol computed optimal structural properties obtained from the final atomic configuration of the interface models.	37
4.5	Computed mechanical properties obtained from the optimal structure of the interface models.	38

Chapter 1

Introduction

The interest shown in the study of metal/ceramic interfaces has growth with the development of new materials having better mechanical, thermal, or electric properties¹. Interfaces between metals and ceramics have a large number of applications: heterogeneous catalysis, microelectronic, thermal barriers, corrosion protection, among others^{2,3}. Metal/ceramic interfaces have unusual electronic and bonding nature because these types of interfaces combine two solids with completely different electronic structures^{3,4}. Aluminum is a metal regularly used in industry, in large part due to its superior strength to weight ratio, is one of the best electrodes, and having excellent electric conductivity^{5,6}. At the same time, Alumina (Al_2O_3) is a widely used ceramic with a pervasive series of applications, microporous catalysis, electronics, chemicals, aerospace industry, and other high-technology fields⁷⁻⁹. One industrially relevant metal/ceramic interface is that between aluminum and alumina. However, a minimal amount of data is available for the Al/ Al_2O_3 interface.

There is limited scientific knowledge about the Al/ Al_2O_3 , mainly because it is challenging to measure an atom-resolved interface structure. Besides, theoretically, first-principles calculations could be impractical for such non-well defined systems, and it is challenging to describe ionic/covalent and metallic bonding consistently. Nevertheless, recent experimental and theoretical approaches try to solve this interface structure, mainly applied to the construction of multilayers of Al/ Al_2O_3 ^{10,11}. Interestingly the experiment found an order of magnitude enhancement of the strength of Al/ Al_2O_3 multilayers after annealing, which might be associated with the precipitation of extremely fine γ -Alumina ($\gamma\text{-Al}_2\text{O}_3$)(111) in Al layers¹⁰. Contradictorily, many theoretical studies of the multilayered Al/ Al_2O_3 do not consider the γ -alumina because there is a debate about its atomic structure¹². Also, $\alpha\text{-Al}_2\text{O}_3$ is the preferred structure for theoretical calculations^{13,14}, because it is the most stable phase among the various Alumina polymorphs.

In the literature there are four mainly theoretically proposed atomic structures for γ -Al₂O₃ and used for theoretical calculations, namely: i) the cubic spinel model by Smrčok *et al.*¹⁵, ii) the monoclinic model by Digne *et al.*¹⁶, iii) the tetragonal nonspinel model by Paglia *et al.*¹⁷, and iv) the monoclinic spinel-based model by Pinto *et al.*¹⁸. Accordingly, Ref. 12 the tetragonal nonspinel and the spinel model describe a better γ -Al₂O₃ atomic structure. Besides, Kovarik *et al.*¹⁹ found that the γ -Al₂O₃ synthesized in their experiments is not atomically flat; instead it forms (111) nanofacets as discussed by Pinto *et al.*¹⁸.

It is essential to understand the structure and electronic properties of metal/oxide interfaces at the atomic scale, such as in the case of α -Aluminum/ γ -Alumina (α -Al/ γ -Al₂O₃). Since these metal/oxide interfaces frequently have peculiar structural, electronic, chemical, and mechanical properties associated with nanostructures. At this point, density-functional theory (DFT) appears as a useful first-principles tool for solving the properties of these metal/oxide interfaces.

1.1 Problem Statement

The problem to be tackled in this thesis is the lack of reliable atomic models for the α -Al/ γ -Al₂O₃ multilayered system that could describe the experiment. We consider that it is relevant to solve this problem because of the different mechanical and electrical properties that we can predict if we have a proper atomic representation of the α -Al/ γ -Al₂O₃ interface. Thus, we use DFT to investigate electronic and mechanical properties of the α -Al/ γ -Al₂O₃ interface multilayered structure to compare them with the experimental data available.

1.2 General and Specific Objectives

The general goal of this thesis is to propose realistic atomic models for the α -Al/ γ -Al₂O₃ interface multilayer structure and predict the electronic and mechanical properties using DFT.

- Model the bulk structures of α -Aluminum (α -Al), and γ -Al₂O₃.
- Analyze the mechanical and electronic properties of α -Al, and γ -Al₂O₃, using DFT.
- Create interface α -Al/ γ -Al₂O₃ structure models that can describe a multilayer system.
- Analyze the mechanical and electronic properties of the models using DFT
- Compare the final theoretical data with the experimental data available of the multilayer structure.

1.3 Overview

This thesis has five chapters and an appendix. The first chapter corresponds to this Introduction, where we introduce the context of the α -Al/ γ -Al₂O₃ multilayer structure, and the main objectives to solve this problem around this structure. In the second chapter, Theoretical Background, the basic concepts of DFT are presented. Additionally there is a description of the computational methods behind DFT. Also, we include a description of the γ -Al₂O₃. In the third chapter, Methodology, we describe the process to obtain the mechanical and electronic properties for the α -Al, γ -Al₂O₃, α -Al/ γ -Al₂O₃ interface models. In the fourth chapter, Results & Discussion, we analyze the mechanical and electronic properties of the bulk structures and the interface models. In the fifth chapter, Conclusions, we recapitulate the principal results and provide an outlook for future research.

Chapter 2

Theoretical Background

2.1 Density Functional Theory

Density-functional theory (DFT) is a successful quantum mechanical modeling method used in many fields like Physics, Chemistry, Materials Science, Geology, and Astrophysics; and it is applied to study the electronic structure of many-body systems, such as atoms, molecules, nanostructures, solids, surfaces, and interfaces. DFT method is another manner to achieve a solution to the many-body Schrödinger equation since the properties of a many-body system can be found by using just the functional of the electronic density. This method uses the electron density of a system to provide us the properties of the ground state.

2.1.1 The Schrödinger equation

The materials at the atomic scale are complicated collections of electrons and nuclei. Then, to understand the behavior of these quantum particles, we have to study the many-body Schrödinger equation²⁰,

$$\hat{H}\Psi(\mathbf{r}_1, \dots, \mathbf{r}_N; \mathbf{R}_1, \dots, \mathbf{R}_M) = E\Psi(\mathbf{r}_1, \dots, \mathbf{r}_N; \mathbf{R}_1, \dots, \mathbf{R}_M), \quad (2.1)$$

where \mathbf{r}_i are the coordinates for the N electrons, and \mathbf{R}_I are the coordinates for the M nuclei. E represents the ground state energy of the many-body system. Finally, \hat{H} is the many-body Hamiltonian represented as,

$$\hat{H} = -\frac{1}{2} \sum_i \nabla_{\mathbf{r}_i}^2 - \frac{1}{2} \sum_I \frac{1}{M_I} \nabla_{\mathbf{R}_I}^2 - \sum_i \sum_I \frac{Z_I}{|\mathbf{r}_i - \mathbf{R}_I|} + \frac{1}{2} \sum_{i \neq j} \frac{1}{|\mathbf{r}_i - \mathbf{r}_j|} + \frac{1}{2} \sum_{I \neq J} \frac{1}{|\mathbf{R}_I - \mathbf{R}_J|}. \quad (2.2)$$

The first two terms of Eq. 2.2 describe the kinetic energy of electrons and nuclei, where M_I represents the mass of the I -th nucleus. The third term represents the attractive Coulomb interaction potential between nuclei and electrons, where Z_I is the atomic number. The fourth term describes the repulsive potential due to the electron-electron interaction, and the last term is the repulsive interaction potential between nuclei. The equation 2.2 is represented in atomic units (*i.e.*, $e = \hbar = m_e = 4\pi\epsilon_0 = 1$).

2.1.2 Born-Oppenheimer approximation

The Born-Oppenheimer approximation (BOA)²¹ assumes the separation of the electronic motion and the nuclear motion in molecules. The nucleus mass is tree orders of magnitude bigger than m_e , then nuclei move much slower than electrons, and correspondingly the time scale of their motion. Thus the Hamiltonian can be simplified as,

$$\hat{H}_e = -\frac{1}{2} \sum_{i=1} \nabla_{\mathbf{r}_i}^2 + \frac{1}{2} \sum_{i \neq j} \frac{1}{|\mathbf{r}_i - \mathbf{r}_j|} + \sum_i V_n(\mathbf{r}_i), \quad (2.3)$$

where \hat{H}_e is known as the electronic Hamiltonian, and $V_n(\mathbf{r}_i)$ is the Coulomb potential of the nuclei experienced by the i th electron. The significance of the BOA is that it allows dividing the wave function into electronic and nuclear components, as follows,

$$\Psi(\mathbf{r}_1, \dots, \mathbf{r}_N; \mathbf{R}_1, \dots, \mathbf{R}_M) = \Psi_e(\mathbf{r}_1, \dots, \mathbf{r}_N) \otimes \Psi_n(\mathbf{R}_1, \dots, \mathbf{R}_M). \quad (2.4)$$

The independence of the electronic wave function from the nuclear coordinate dramatically simplifies the problem in that the trial wave function needs only to be a guess for the electronic wave function.

2.1.3 Hartree-Fock approximation

The number of degrees of freedom of the many-body Hamiltonian decreased after BOA. The standard approach to solve the Eq. 2.3 is using the Hartree-Fock (HF) approximation²², which relies on the assumption that electrons do interact indeed, but perhaps this interaction is not too strong. Given this premise, the many-body wave function is postulated as a Slater determinant²³,

$$\Psi(\mathbf{r}_1, \dots, \mathbf{r}_N) = \frac{1}{\sqrt{N!}} \begin{vmatrix} \phi_1(\mathbf{r}_1) & \dots & \phi_1(\mathbf{r}_N) \\ \vdots & \ddots & \vdots \\ \phi_N(\mathbf{r}_1) & \dots & \phi_N(\mathbf{r}_N) \end{vmatrix}, \quad (2.5)$$

where $\phi_i(\mathbf{r})$ represents the single-particle wavefunctions. The Slater determinant fulfills the antisymmetric feature of the wavefunction upon the interchange of the coordinates of two electrons. By using the variational method to

minimize the expectation value of the Hamiltonian in Eq. 2.3, $E = \langle \Psi | \hat{H} | \Psi \rangle$, with respect the functions $\phi_i(\mathbf{r})$ in the Slater determinant, and using the orthonormality constrain of these functions, one obtains the HF equations²⁴:

$$\left[-\frac{\nabla^2}{2} + V_n(\mathbf{r}) + V_H(\mathbf{r}) \right] \phi_i(\mathbf{r}) + \int d\mathbf{r}' V_X(\mathbf{r}, \mathbf{r}') \phi_i(\mathbf{r}') = \varepsilon_i \phi_i(\mathbf{r}), \quad (2.6)$$

$$n(\mathbf{r}) = \sum_i |\phi_i(\mathbf{r})|^2, \quad (2.7)$$

$$\nabla^2 V_H(\mathbf{r}) = -4\pi n(\mathbf{r}), \quad (2.8)$$

where $V_H(\mathbf{r})$ is called the Hartree potential, $V_X(\mathbf{r}, \mathbf{r}')$ represents the Fock exchange potential, and $n(\mathbf{r})$ is the electron charge density. The HF potential is non-local, and it depends on the spin orbitals. Thus, the HF equations must be solved self-consistently. Besides, the HF method demands a lot of computational operations and avoids the correlation between electrons.

2.1.4 The Hohenberg-Kohn theorems

In order to develop a theory that reduces the computational operations, we can consider expressing the system energy in terms of electron density instead of wave equations. This idea led to the development of density-functional theory (DFT), which is based on two essential theorems proposed by Hohenberg and Kohn (HK)²⁵.

Theorem 1 (Uniqueness). The ground-state electronic density $n(\mathbf{r})$ of a system of interacting electrons uniquely determines the external potential $V_n(\mathbf{r})$ in which the electrons evolve.

This $V_n(\mathbf{r})$ defines a unique Hamiltonian, and it also defines all properties of the ground state system. Therefore, this indicates that the total energy must be a functional of the density $E = F[n]$. In particular,

$$E[n] = \langle \Psi | \sum_i V_n(\mathbf{r}_i) | \Psi \rangle + \langle \Psi | \hat{T} + \hat{W} | \Psi \rangle, \quad (2.9)$$

using the relation between the wavefunction and the electron density we have

$$E[n] = \int d\mathbf{r} n(\mathbf{r}) V_n(\mathbf{r}) + \langle \Psi | \hat{T} + \hat{W} | \Psi \rangle. \quad (2.10)$$

where \hat{T} and \hat{W} represent the kinetic and the Coulomb energy, respectively. The dependence on the density in these terms is implicit.

Theorem 2 (Variational Principle). The universal functional for the energy $E[n(\mathbf{r})]$ is defined in terms of the electronic density $n(\mathbf{r})$. The ground-state is obtained for the density $n_0(\mathbf{r})$ that minimizes this functional.

As a result, the corresponding density $n(\mathbf{r})$ that minimizes the functional is the exact ground state density $n_0(\mathbf{r})$.

$$\frac{\delta}{\delta n} E[n] \Big|_{n=n_0} = 0 \quad (2.11)$$

and

$$E_0 = E[n_0]. \quad (2.12)$$

Therefore, the ground-state of the system can be obtained using conjugate gradient calculations or other iterative methods.

2.1.5 The Kohn-Sham equations

HK theorems give us the main idea behind DFT, the total energy of many electrons in the ground state is a functional of the electron density. In order to construct this functional we consider the Kohn-Sham (KS) ansatz. This ansatz proposed that the interacting many-body problem can be replaced by an auxiliary independent-particle problem²⁶. Precisely, the idea of Kohn and Sham was to split the implicit terms of Eq. 2.10 into the kinetic and Coulomb energy of independent electrons and all the remaining painful many-body effects of the interacting system:

$$E = F[n] \quad (2.13)$$

$$= \int d\mathbf{r} n(\mathbf{r}) V_n(\mathbf{r}) - \sum_i \int d\mathbf{r} \phi_i^*(\mathbf{r}) \frac{\nabla^2}{2} \phi_i(\mathbf{r}) + \frac{1}{2} \int \int d\mathbf{r} d\mathbf{r}' \frac{n(\mathbf{r})n(\mathbf{r}')}{|\mathbf{r} - \mathbf{r}'|} + E_{xc}[n], \quad (2.14)$$

where the first three terms represent the external potential, the kinetic energy, and the Hartree energy for the independent electrons approximations. The last term is called the exchange and correlation (xc) energy.

Using the second HK theorem with the additional constrain that the total number of electrons has to remain constant under any variation of the density, the ground-state density of the system, n_0 , is the function that minimizes the total energy, $E = F[n]$:

$$\frac{\delta F[n]}{\delta n} \Big|_{n_0} = 0. \quad (2.15)$$

Then the Hohenberg-Kohn variational principle leads to:

$$\left[-\frac{1}{2} \nabla^2 + V_n(\mathbf{r}) + V_H(\mathbf{r}) + V_{xc}(\mathbf{r}) \right] \phi_i(\mathbf{r}) = \varepsilon_i \phi_i(\mathbf{r}), \quad (2.16)$$

here the kinetic energy, the external nuclear potential, the Hartree potential and the xc potential are represented. The last term, V_{xc} is given by:

$$V_{xc}(\mathbf{r}) = \frac{\delta E_{xc}[n]}{\delta n} \Big|_{n(\mathbf{r})}. \quad (2.17)$$

Finally, the set of equations given by Eq. 2.16 are called KS equations²⁶. These equations define a self-consistent cycle to be solved. In addition this set of equation are the basis for computational methods for calculating materials properties from the first principles of quantum mechanics.

2.1.6 Self-consistent calculations

To solve the KS equations, we need to define the Hartree potential. To define the Hartree potential, we need to know the electron density. However, to find the electron density, we must know the single-electron wave functions, and to know these wavefunctions, we have to solve the KS equations. Then, this defines a self-consistent cycle to be solved. Thus, to break this cycle, the following algorithm can solve this problem^{27,28}:

1. Specify the nuclear coordinates to calculate the nuclear potential, V_n .
2. Propose an initial guess for the electron density, $n(\mathbf{r})$.
3. Estimate the Hartree V_H and xc potentials V_{xc} , and from there, the total potential V_{tot} .
4. Solve the KS equations to find the single-particle wavefunctions, $\phi_i(\mathbf{r})$.
5. Calculate the electron density defined by the KS single-particle wavefunctions from the previous step, $n_{KS}(\mathbf{r}) = \sum_i |\phi_i(\mathbf{r})|^2$.
6. Compare the calculated electron density, $n_{KS}(\mathbf{r})$, with the initial guess used in solving the KS equations, $n(\mathbf{r})$. If the two densities are the same, then this is the ground-state electron density, and it can be used to calculate the total energy. If the two densities are different, then the trial electron density must be renewed. Once this is done, the process begins again from step 3.

This process is repeated until the new density agrees with the old density within the desired tolerance; at that point, we have obtained self-consistency, and with this final density it is possible to calculate the total energy using Eq. 2.14. The procedure is showed in Figure 2.1.

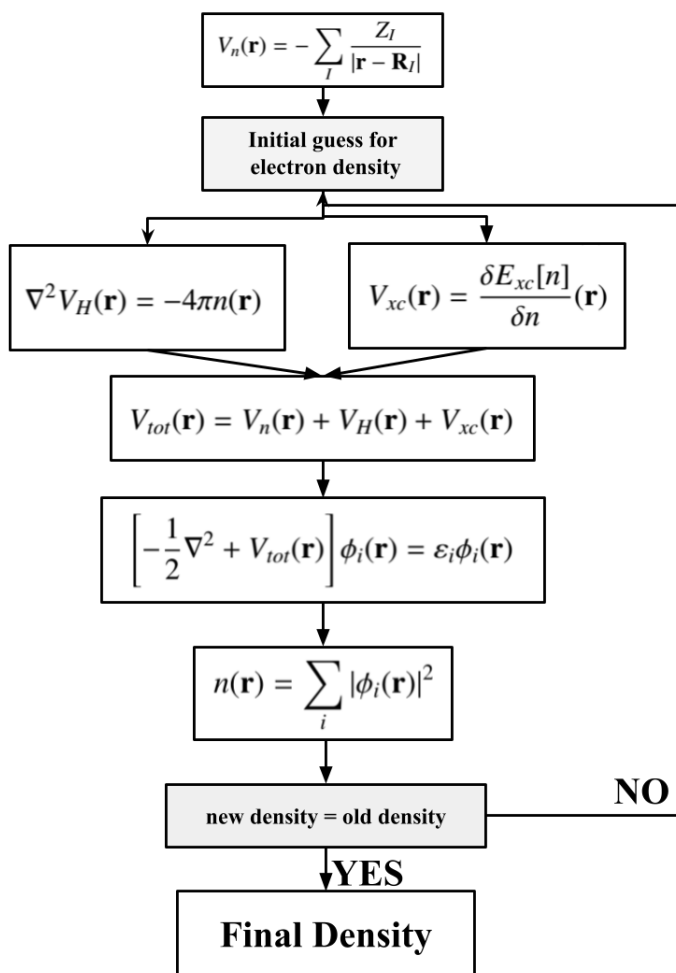


Figure 2.1: Kohn-Sham self-consistent process. Adapted from Ref. 28.

2.1.7 Exchange and correlation functionals

Until now, it should be possible to perform self-consistent calculations using KS equations. However, there is still a problem, the xc functional is not known. Then, for a proper application of DFT, we need a good approximation of the xc functional. Thus, many approximations with different complexity were created in the scientific community as follows.

The local density approximation

The local density approximation (LDA) is the simplest method to approximate xc functionals^{29,30}. The principal idea of this model is to consider a uniform electron gas. Then, the xc energy is achieved by assuming that it depends locally on the xc energy density of the homogeneous electron gas, $\epsilon_{xc}^{\text{HEG}}(n(\mathbf{r}))$. The total xc energy is calculated by integrating the exchange-correlation energy density over the volume of the system:

$$E_{xc}^{\text{LDA}}[n(\mathbf{r})] = \int d^3\mathbf{r} \epsilon_{xc}^{\text{HEG}}[n(\mathbf{r})]n(\mathbf{r}). \quad (2.18)$$

Despite the approximations involved in the LDA, it has been shown to give consistent structural properties such as bond lengths, lattice parameters and atomic positions within 1 or 2 % over a wide range of systems³¹. The reason why the LDA works so surprisingly well is that the exchange-correlation hole fulfills all the sum rules and that for reliable results, the exact shape of the xc hole is not required; only its average is of significance¹³. Unfortunately, this approximation is not reliable for all the properties. Excited states and band gap energy are poorly described within LDA³².

The generalized gradient approximation

The generalized gradient approximation (GGA) proposes to improve the LDA functional by including terms of both the density and its gradient into the xc energy functional. The GGA functional is usually defined by^{33,34},

$$E_{xc}^{\text{GGA}}[n_{\uparrow}, n_{\downarrow}] = \int d^3\mathbf{r} \epsilon_{xc}^{\text{HEG}}[n_{\uparrow}, n_{\downarrow}, \nabla n_{\uparrow}, \nabla n_{\downarrow}]n(\mathbf{r}). \quad (2.19)$$

Then, a more simple way to represent this functional is to separate it in exchange and correlation contribution, as follows^{33,35}:

$$E_x^{\text{GGA}}[n(\mathbf{r})] = \int d^3\mathbf{r} \epsilon_x^{\text{HEG}}[n(\mathbf{r})]F_x[s(\mathbf{r})] \quad (2.20)$$

here E_x^{GGA} is the GGA exchange functional, $n(\mathbf{r})$ is the electronic density, ϵ_x^{HEG} is the exchange energy density, F_x is an enhancement factor, and s is defined as,

$$s = \frac{|\nabla n|}{2k_F n}, \quad (2.21)$$

with $k_F = (3\pi^2 n)^{1/3}$. The enhancement factor can be represented as,

$$F_x[s] = 1 + \mu s^2 + \dots \quad (s \rightarrow 0). \quad (2.22)$$

In the same way we can define the correlation functional as^{33,35}:

$$E_c^{\text{GGA}}[n(\mathbf{r})] = \int d^3\mathbf{r} \left\{ \epsilon_c^{\text{HEG}}[n(\mathbf{r})] + \frac{\pi k_F}{2} \beta s^2 [n(\mathbf{r})] + \dots \right\} \quad (2.23)$$

where ϵ_c^{HEG} is the correlation energy and β is a coefficient.

Moreover, some of the GGA methods that were developed often have been empirically calibrated to optimize the precision of the atomization energies of standard sets of molecules and have successfully produced the structural and energetic features of various systems. The generally used GGA functional was proposed by Perdew, Burke and Ernzerhof (PBE) in 1996³³. The PBE functional used the following fundamental constants,

$$\mu = 0.21951 \text{ and } \beta = 0.0066725. \quad (2.24)$$

The PBEsol functional is an upgrade of the PBE GGA that improves predictions of equilibrium properties of packed solids and their surfaces³⁶. For this functional only the fundamental constants change to

$$\mu = \mu_{GE} = 0.1235 \text{ and } \beta = 0.046, \quad (2.25)$$

where μ_{GE} is used to obtain an accurate gradient expansion. The PBEsol functional was used to solve the metal/oxide interface studied in this thesis.

2.2 Computational methods

Computational methods in materials science are demanded to supply specific quantities that can be used to predict features of materials and their behavior during deformation or other physical processes. First-principle methods infer the required quantities from the computed electronic structure. The first-principles method obtains the solution to the Schrodinger equation through a series of approaches and simplifications.

2.2.1 Periodic systems and plane waves

In a solid, the infinitely large number of electrons represents a problem at the moment to calculate its properties. Computationally, a solid is represented as a perfect crystal repeated periodically in space. Because of this periodic arrangement of ions, the electrons change their effective potential that has the same periodicity as the crystal. The physical system is characterized by the coordinates of the atoms in the primitive unit cell and the primitive translation vectors ($\mathbf{a}_1, \mathbf{a}_2, \mathbf{a}_3$) that determine how the unit cell is repeated²⁷.

By definition of the periodic crystal, any real space property $f(\mathbf{r})$ of the system such as its electronic density or some potential energy is invariant under any translation of the primitive translation vectors and integer combinations of them³⁷:

$$f(\mathbf{r} + \mathbf{R}) = f(\mathbf{r}) \quad (2.26)$$

with $\mathbf{R} = n_1 \mathbf{a}_1 + n_2 \mathbf{a}_2 + n_3 \mathbf{a}_3$, and $n_1, n_2, n_3 \in \mathbb{Z}$.

As a periodic quantity, $f(\mathbf{r})$ can be expressed as a Fourier series³⁸

$$f(\mathbf{r}) = \sum_{\mathbf{G}} f_{\mathbf{G}} e^{\mathbf{G} \cdot \mathbf{r}} \quad (2.27)$$

in which $\mathbf{G} = m_1 \mathbf{b}_1 + m_2 \mathbf{b}_2 + m_3 \mathbf{b}_3$ ($m_1, m_2, m_3 \in \mathbb{Z}$) is a reciprocal space vector and $(\mathbf{b}_1, \mathbf{b}_2, \mathbf{b}_3)$ are the reciprocal space primitive vectors defined as

$$\mathbf{b}_1 = \frac{\mathbf{a}_2 \times \mathbf{a}_3}{V_{cell}}, \quad \mathbf{b}_2 = \frac{\mathbf{a}_3 \times \mathbf{a}_1}{V_{cell}}, \quad \text{and} \quad \mathbf{b}_3 = \frac{\mathbf{a}_1 \times \mathbf{a}_2}{V_{cell}} \quad (2.28)$$

where $V_{cell} = \mathbf{a}_1 \cdot (\mathbf{a}_2 \times \mathbf{a}_3)$ is the volume of the primitive cell. In reciprocal space, it is possible to define a Wigner-Seitz cell, here it is called the Brillouin zone since many cell properties appear if we consider it³⁸.

The Fourier coefficients $f_{\mathbf{G}}$ in Eq. 2.27 are obtained as

$$f_{\mathbf{G}} = \frac{1}{V_{cell}} \int_{V_{cell}} d\mathbf{r} f(\mathbf{r}) e^{-i\mathbf{G} \cdot \mathbf{r}}. \quad (2.29)$$

The periodicity of the effective potential of the system implies that it must verify the condition of Eq. 2.26. Then, a direct consequence is the Bloch theorem³⁸:

Theorem 3 (Bloch). In a perfect crystal, one can choose the eigenfunctions of a Schrödinger equation in a periodic potential $V(\mathbf{r})$ to be written as the product of a plane wave part $e^{i\mathbf{k} \cdot \mathbf{r}}$ and a periodic function $u_{\mathbf{k}}(\mathbf{r})$ with the same periodicity as the potential:

$$\phi_{\mathbf{k}}(\mathbf{r}) = e^{i\mathbf{k} \cdot \mathbf{r}} u_{\mathbf{k}}(\mathbf{r}) \quad (2.30)$$

where

$$u_{\mathbf{k}}(\mathbf{r} + \mathbf{R}) = u_{\mathbf{k}}(\mathbf{r}) \quad (2.31)$$

and \mathbf{k} is a reciprocal space vector which the quantum number resulting from the translational symmetry of the potential.

Using the Fourier description and the Bloch theorem leads to reformulate the wavefunction of a system as²⁷

$$\phi_{\mathbf{k}}(\mathbf{r}) = \frac{1}{V_{cell}} \sum_{\mathbf{G}} c_{\mathbf{k}+\mathbf{G}} e^{i(\mathbf{k}+\mathbf{G}) \cdot \mathbf{r}} \quad (2.32)$$

where the sum in principle is infinite but in practice, the basis set defined by the set of \mathbf{G} vectors used is truncated and include plane waves up to a given kinetic energy cutoff E_{cut} :

$$\frac{|\mathbf{k} + \mathbf{G}|^2}{2} < E_{cut}. \quad (2.33)$$

The truncation in the set of \mathbf{G} vectors induces errors in the computed properties. This error can be reduced by improving the E_{cut} for a desired accuracy. It should be noted that the all-electron wavefunction of a system has an extensive oscillatory behavior close to the nuclei. Therefore, a significant kinetic energy cut-off and hence a high computational cost. Therefore, one usually makes another assumption about the separation of core and valence electrons leading to the pseudopotential approximation.

2.2.2 Pseudopotentials

The pseudopotentials are based on the idea that the valence electrons mostly determine the chemical and physical properties; the core electrons are tightly bonded to the nucleus. Moreover, for DFT calculations, we can approximate the core electrons by pseudopotentials^{39,40}. If we do not have a smooth and weak pseudopotential, it becomes complicated to expand wave functions using a reasonable number of plane waves.

The criterion for choosing a pseudopotential lies in the character of the bonding between the ions in the system and how well it reproduces the results of accurate all-electron calculations⁴¹. One problem of pseudopotential calculations is that it needs non-linear core corrections since of the non-linearity of the exchange interaction between core and valence electrons⁴². This obstacle may be eliminated using the projector-augmented wave method.

2.2.3 Projector-augmented wave method

The projector augmented wave (PAW) method, developed originally by Blöchl⁴³, combines the ideas of a smooth pseudopotential $|\tilde{\psi}_n\rangle$, and all-electrons wavefunctions $|\psi_n\rangle$, using a linear transformation:

$$|\psi_n\rangle = |\tilde{\psi}_n\rangle + \sum_i (|\phi_i\rangle - |\tilde{\phi}_i\rangle) \langle \tilde{p}_i | \tilde{\psi}_n \rangle; \quad (2.34)$$

the pseudo-wave functions $|\tilde{\psi}_n\rangle$ are the variational quantities which are expanded in plane waves, where n represents the band index. The wavefunctions $|\tilde{\psi}_n\rangle$ and $|\psi_n\rangle$ are identical outside augmentation spheres enclosing the atoms. Inside the spheres $|\tilde{\psi}_n\rangle$ are a bad approximation to the exact form of the wave functions. The all-electron partial waves, ϕ_i are solutions of the spherical scalar-relativistic Schrödinger equation for a non-spinpolarized atom. The pseudo-partial waves $\tilde{\phi}_i$ are node-less and identical to ϕ_i outside a radius approximately equal to half the nearest-neighbor distance and match continuously inside these spheres. Finally, the projector functions \tilde{p}_i are restricted to be dual to the partial waves^{41,44}.

Within the PAW method the charge density is composed of three contributions,

$$n(\mathbf{r}) = \tilde{n}(\mathbf{r}) - n^*(\mathbf{r}) + n(\mathbf{r}), \quad (2.35)$$

where

$$\tilde{n}(\mathbf{r}) = \langle \tilde{\Psi}_n | \mathbf{r} \rangle \langle \mathbf{r} | \tilde{\Psi}_n \rangle \quad (2.36)$$

is a pseudo charge density expanded in a plane wave basis, while

$$n^*(\mathbf{r}) = \sum_{i,j} \langle \tilde{\phi}_i | \mathbf{r} \rangle \langle \mathbf{r} | \tilde{\phi}_j \rangle \langle \tilde{\Psi}_n | \tilde{p}_i \rangle \langle \tilde{p}_j | \tilde{\Psi}_n \rangle \quad (2.37)$$

and

$$n(\mathbf{r}) = \sum_{i,j} \langle \phi_i | \mathbf{r} \rangle \langle \mathbf{r} | \phi_j \rangle \langle \tilde{\Psi}_n | \tilde{p}_i \rangle \langle \tilde{p}_j | \tilde{\Psi}_n \rangle \quad (2.38)$$

are pseudo and all-electron on-site charge densities expanded as atom-centered radial grids. This decomposition of the wave functions and the charge density provides the basic principle of the PAW method: A node-less pseudo wave function and the corresponding pseudo charge density are determined as a solution of the KS equation in a plane wave basis⁴¹.

2.2.4 Computing the atomic forces and the Hellmann-Feymann theorem

One important thing when we do DFT calculations is to predict the equilibrium structure of material starting from the first principles of quantum mechanics. The equilibrium structures of solids are described at zero-temperature since this is often enough approximation for describing materials at room temperature. This equilibrium structure corresponds to the situation where the total force acting on each nucleus vanishes. As a result, nuclei positions do not change²⁸.

The determination of equilibrium structures of materials requires the minimization of the total potential energy, U , concerning all the $3M$ nuclear degrees of freedom,

$$\mathbf{F}_I = -\frac{\partial U}{\partial \mathbf{R}_I}, \quad (2.39)$$

where \mathbf{F} represents the force acting on the I -th nucleus, and U is defined as,

$$U(\mathbf{R}_1, \dots, \mathbf{R}_M) = \frac{1}{2} \sum_{I \neq J} \frac{Z_I Z_J}{|\mathbf{R}_I - \mathbf{R}_J|} + E(\mathbf{R}_1, \dots, \mathbf{R}_M), \quad (2.40)$$

here $E(\mathbf{R}_1, \dots, \mathbf{R}_M)$, is the total energy of the electrons when the nuclei are held immobile in positions $\mathbf{R}_1, \dots, \mathbf{R}_M$. Solving these two last equations are proven to be very time-consuming and demands $3M + 1$ calculations²⁸. Then, the Hellmann-Feynman theorem is used to replace all these number of calculations by one single calculation.

The Hellmann-Feynman^{45,46} theorem, allows us to calculate the atomic forces as follows:

$$\mathbf{F}_I = Z_I \left[\int d\mathbf{r} n(\mathbf{r}) \frac{\mathbf{r} - \mathbf{R}_I}{|\mathbf{r} - \mathbf{R}_I|^3} - \sum_{J \neq I} Z_J \frac{\mathbf{R}_J - \mathbf{R}_I}{|\mathbf{R}_J - \mathbf{R}_I|^3} \right]. \quad (2.41)$$

This equation let us know that the calculation of the forces for all M atoms in our system can be determined by the electron density, $n(\mathbf{r})$, for one set of nuclear coordinates.

2.2.5 *Ab initio* Molecular dynamics and simulating annealing

The basic concept of *ab initio* Molecular Dynamics (MD) is that the potential energy of a system can be calculated using quantum mechanics. In other words, we can perform MD by calculating $U(\mathbf{R}_1, \dots, \mathbf{R}_M)$ using DFT. *Ab initio* MD refers to any method that advances the positions of nuclei along trajectories defined by classical mechanics from forces calculated from DFT²⁷.

In 1985, Car and Parrinello⁴⁷ proposed a *ab initio* MD method. The main feature of this method is that the total energy of the system depends on the dynamics of nuclei and electronic KS orbitals. The Lagrangian according to *ab initio* MD is expressed as:

$$L = \sum_I \frac{1}{2} m_I \mathbf{R}_I^2 + \mu \sum_i f_i \int d\mathbf{r} |\psi_i(\mathbf{r})|^2 - E_{KS}[\psi_i(\mathbf{r}), \mathbf{R}] + \sum_i f_i \sum_j \Lambda_{ij} \left[\int d\mathbf{r} \psi_i^*(\mathbf{r}) \psi_j(\mathbf{r}) - \delta_{ij} \right], \quad (2.42)$$

where the first term is the kinetic energy of the I -th nuclei, the second term indicates the fictitious dynamic of KS orbitals via the fictitious electron mass, μ . The third term represents the KS energy at the instantaneously fixed nuclear configuration; the last term ensures the orthonormality of KS orbitals during the simulation by the Lagrange multipliers Λ_{ij} , the coefficient f_i accounts for the occupations numbers of associated orbitals²⁷.

Ab initio MD helps us to generate a model that mimic the experimental process to obtain a material. For example, to simulate annealing to very high temperatures and then quenching of an multilayer system of a metal/oxide interface.

2.2.6 Introduction to VASP

Vienna *ab initio* simulation package (VASP)⁴⁸⁻⁵¹ is a plane wave code that performs density functional calculations. VASP is currently the DFT plane wave code most cited within scientific community. VASP determines structural and electronic properties different systems such as solid states and condensed matters. VASP determines the electronic ground state configuration using pseudopotentials with a plane wave basis set and the PAW method. Additionally, the code uses efficient matrix diagonalization techniques that allow performing energy calculations and structural optimizations for systems with thousands of atoms. This code is applied to study structure and phase

stability, mechanical and dynamical properties, among others for metals, semiconductors, and insulators in surfaces, interfaces, or thin films⁴¹. In this thesis, we used this code to solve a metal /oxide interface.

A standard VASP calculation requires at minimum four basic input files⁵²:

INCAR includes the simulation parameters. Also, it decides what calculation needs to be done and how they should be done, e.g., cutoff energy, functional, relaxation process, annealing process, and others.

POSCAR specifies the atomic position of the atoms and the lattice parameters of the system to study. The number of each type atom need to be written in one line in accordance to how the elements appears in the POTCAR file.

POTCAR contains the potentials for every atom species sorted in accordance of how the elements appears in the POSCAR file.

KPOINTS includes the set of k -points within of the Brillouin zone. The choice of the k -points depends on the type and size of the studied system.

The outcome of this standard calculation will produce several files, the most relevant are⁵²:

CONTCAR includes the position of the atoms in the system given in direct coordinates, it is similar to POSCAR file. After a structural relaxation, the file will be reach to the energetically most stable configuration.

CHGCAR and CHG are files with the total charge density multiplied by the cell volume.

DOSCAR specifies the data for the density of states (DOS) and patial density of states (PDOS).

EIGENVAL contains the KS eigenvalues for all k -points.

OUTCAR includes all the details of the calculation, input parameters and outcome of the simulation.

WAVECAR is a binary file and contains the wavefunctions, the number of bands, the eigenvalues of the computed system.

2.3 The γ -Alumina Oxide

Among the various transition alumina polymorphs, γ -Alumina (γ -Al₂O₃) is the most important in catalysis and different industries like automotive and petroleum^{19,53}. The structural properties of γ -Al₂O₃ changes according to the preparation technique used to synthesize it^{53,54}. However, the most used technique to obtain γ -Al₂O₃ is by thermal decomposition at 600 to 800 °C of Boehmite (AlOOH)^{19,55,56}.

Even though there are many theoretically investigations of γ -Al₂O₃, there is still the debate of which atomic structure describes better the properties of this crystal¹². In the literature there are four mainly proposed atomic structures of γ -Al₂O₃ used for theoretical calculations: i) the cubic spinel model by Smrčok *et al.*¹⁵, ii) the monoclinic

model by Digne *et al.*¹⁶, iii) the tetragonal nonspinel model by Paglia *et al.*¹⁷, and iv) the monoclinic spinel-based model by Pinto *et al.*¹⁸. According to Ref. 12, the tetragonal nonspinel and the spinel model describe better γ -Al₂O₃ atomic structure. Moreover, Kovarik *et al.*¹⁹ found that the γ -Al₂O₃ synthesized in their experiments is not atomically flat. Instead, it forms (111) nanofacets, as predicted by Pinto *et al.*¹⁸ model. Thus, in the present work, we used the model proposed by Pinto *et al.*¹⁸, showed in Fig. 2.2.

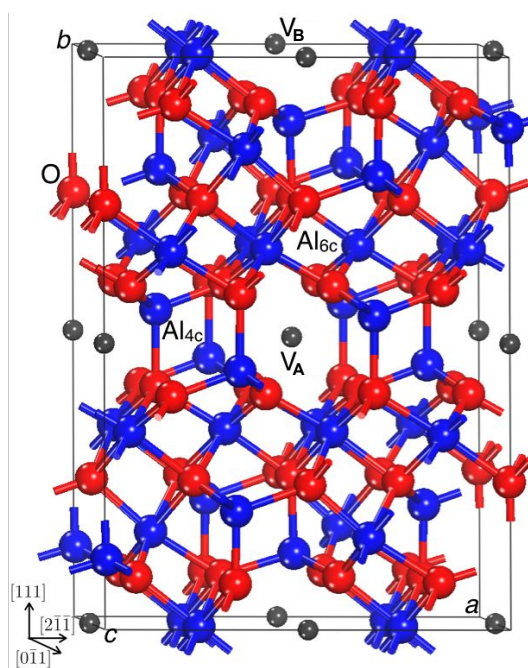


Figure 2.2: The γ -Al₂O₃ monoclinic spinel-based crystal model, the blue, red and grey spheres represent the Al, O, and Al-vacancy sites (V_A and V_B); notice the structure is composed of an array of tetrahedral Al_{4c} and octahedral Al_{6c} sites. The axes are oriented, considering the perfect cubic spinel structure. Adapted from Ref. 18.

According to Pinto *et al.*¹⁸, γ -Al₂O₃ is a defective spinel structure where two octahedral Al are extracted, forming the nonequivalent V_A and V_B vacancy sites as displayed in Fig. 2.2. The GGA-PW91 predicted structure is monoclinic that belongs to the space group $C2/m$, No. 12. The GGA-PW91 computed bulk modulus for γ -Al₂O₃ is 209 GPa. The computed electronic structure is reported with a bandgap of 3.97 eV¹⁸. In addition, Pinto *et al.*¹⁸ computed the energy of γ -Al₂O₃, they investigated the (111), (001), (110), and (150) surfaces. It is important to mention that along the {111} planes, they considered two surfaces: (111)a formed by cleaving through a plane that

crosses the V_A sites as displayed in Fig. 2.3(a), and (111)b, formed by cleaving through a plane that crosses the V_B sites as displayed in Fig. 2.3(b). The reported surface energies are showed in Table 2.1. The surfaces highlighted with yellow were those we selected to study in this work: the γ -(111)a as the most likely surface reported and the surface of the same family, the γ -(111)b.

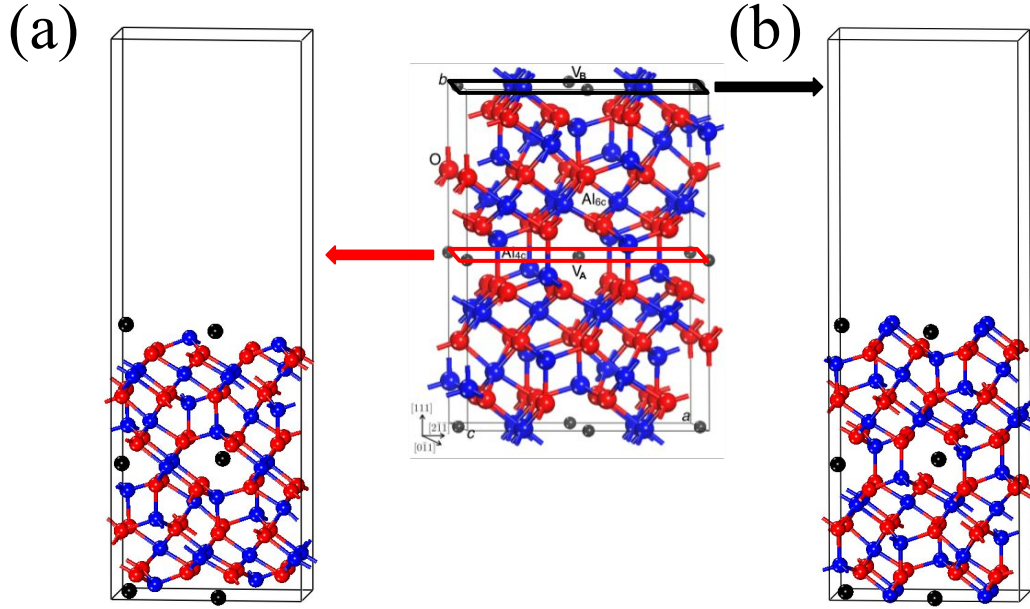


Figure 2.3: γ - Al_2O_3 (a) (111)a, and (b) (111)b slabs; the blue and red spheres represent the Al and O, while the black spheres are the Al-vacancy sites.

Table 2.1: Surface energies for γ - Al_2O_3 , after (σ_R) and before (σ_S) full relaxation, slabs. Adapted for Ref. 18.

Surface	$\sigma_R(\text{J/m}^2)$	$\sigma_S(\text{J/m}^2)$
γ -(111)a	0.95	1.62
γ -(111)b	1.85	3.57
γ -(001)	1.05	2.97
γ -(110)	1.53	3.43
γ -(150)	1.91	2.79

Chapter 3

Methodology

3.1 Computational Details

The plane wave Vienna *ab initio* simulation package (VASP) was used for the density-functional theory (DFT) calculations^{50,51}. This package uses a plane-waves basis set ideal for crystalline systems. The necessary parameters for the simulations are: the revised Perdew-Burke-Ernzerhof GGA (PBEsol) functional was employed to treat the exchange and correlation (xc) energy³³, core electrons were described with projector augmented wave (PAW) potential^{43,44}, where the potential for the aluminium and oxygen atoms were generated in the electron configuration [Ne] 3s² 3p¹ and [1s²] 2s² 2p⁴, respectively; square brackets denote the core electron configurations. Depending on the system, appropriate cutoff energy and k -points mesh were chosen to converge the total energy to < 1 meV/atom and ionic relaxations to < 0.01 eV Å⁻¹ (see below for details). Using those parameters, we computed the equation of state (EOS) for α -Aluminum (α -Al), γ -Alumina (γ -Al₂O₃) and α -Aluminum/ γ -Alumina (α -Al/ γ -Al₂O₃)(111) multilayer models.

3.1.1 Energy convergence and optimal parameters for VASP calculations

Before we start to simulate the systems of interest for this study, we need to find out the optimal parameters for α -Al, γ -Al₂O₃ and α -Al/ γ -Al₂O₃(111) systems. In Figure 3.1 is displayed the convergence test for α -Al; we observe that total energy converges to <1 meV/atom for cut-off energy E_{cut} of 400 eV and above, in our study we use $E_{\text{cut}}=500$ eV (*cf.* Fig.3.1(a)). Using that value for E_{cut} we proceed to compute the convergence of the total energy with respect

to the k -point mesh or Δk separation, considering the result displayed in Fig.3.1(b), we chose $\Delta k/2\pi=0.021 \text{ \AA}^{-1}$ that corresponds to the k -point mesh $21 \times 21 \times 21$.

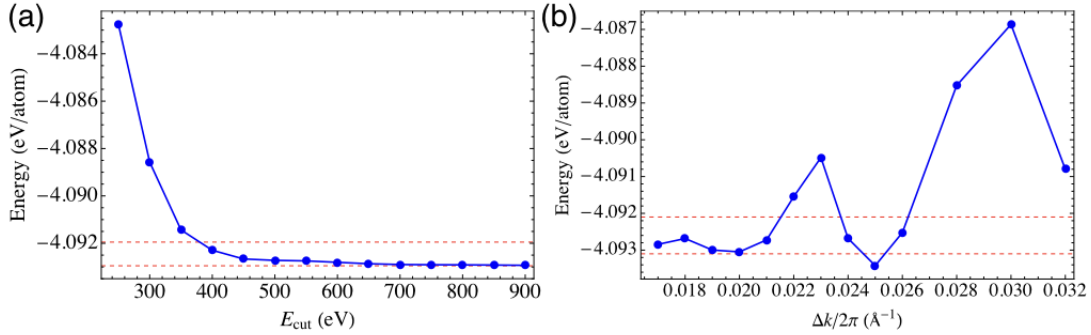


Figure 3.1: Convergence of the total energy for α -Al with respect to (a) the cut-off energy E_{cut} and (b) Δk separation of the k -points in the reciprocal space. In both figures, the horizontal red dashed lines delimit the energy range of 1 meV/atom.

The convergence test for γ - Al_2O_3 is showed in Figure 3.2 . We notice that the total energy converges to <1 meV/atom for cut-off energy E_{cut} of 700 eV. Using that value of E_{cut} , we computed the convergence of the total energy with respect to the k -point mesh, then observe that the total energy converges to <1 meV/atom for $\Delta k/2\pi$ of 0.06 \AA^{-1} and below, in our case we use $\Delta k/2\pi=0.04 \text{ \AA}^{-1}$ that corresponds to the k -point mesh $5 \times 5 \times 2$, see Fig. 3.2(b).

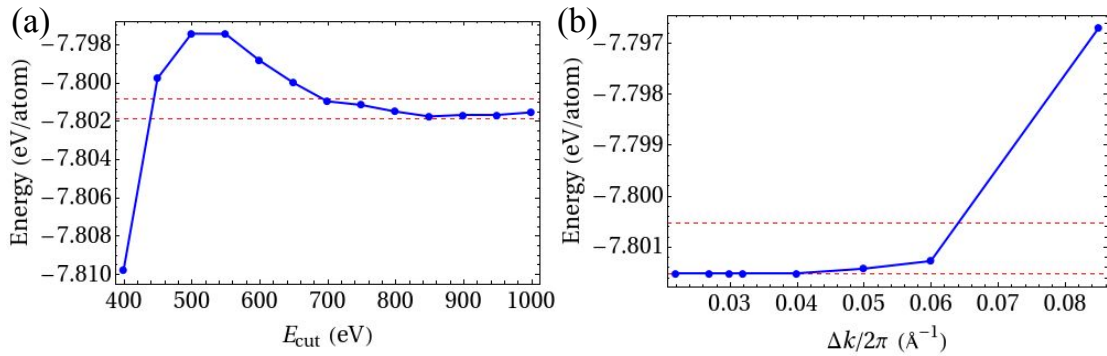


Figure 3.2: Convergence of the total energy for γ - Al_2O_3 with respect to (a) the cut-off energy E_{cut} and (b) Δk separation of the k -points in the reciprocal space. In both figures, the horizontal red dashed lines delimit the energy range of 1 meV/atom.

In order to estimate the optimal parameters E_{cut} and k -point mesh for the α -Al/ γ -Al₂O₃(111) multilayered system, we used a typical model as displayed in Fig. 3.4. The convergence is displayed in Fig. 3.3 and the optimal parameters that converge the total energy to <1meV/atom are $E_{\text{cut}}=700$ eV and $\Delta k/2\pi=0.035$ Å⁻¹ that corresponds to the k -point mesh $3 \times 5 \times 1$.

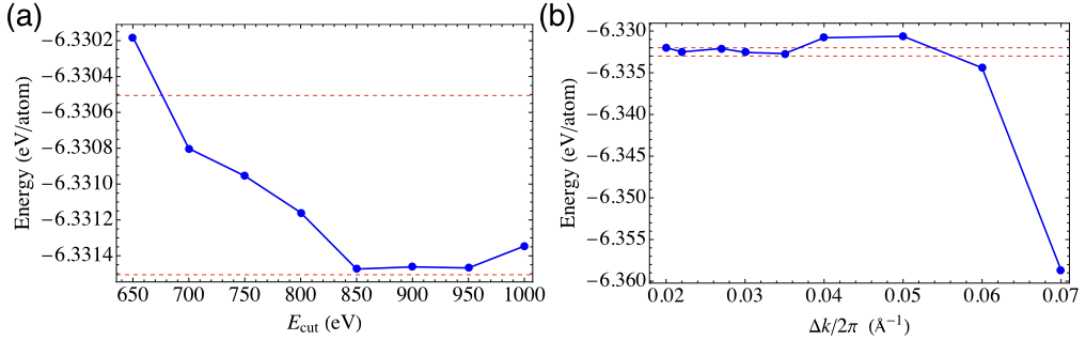


Figure 3.3: Convergence of the total energy for α -Al/ γ -Al₂O₃(111) multilayered with respect to (a) the cut-off energy E_{cut} and (b) Δk separation of the k -points in the reciprocal space. In both figures, the horizontal red dashed lines delimit the energy range of 1 meV/atom.

The summary of the optimal parameters obtained from convergence test are presented in Table 3.1.

Table 3.1: Optimal parameters used in VASP for α -Al, γ -Al₂O₃ and α -Al/ γ -Al₂O₃(111) to converge the total energy to <1 meV/atom.

Optimal Parameters	α -Al	γ -Al ₂ O ₃	α -Al/ γ -Al ₂ O ₃ (111)
E_{cut} (eV)	500	700	700
$\Delta k/2\pi$ (Å ⁻¹)	0.021	0.040	0.035
k -points mesh	$21 \times 21 \times 21$	$5 \times 5 \times 2$	$3 \times 5 \times 1$

3.1.2 α -Al/ γ -Al₂O₃ multilayer models

In this work we consider only the case of α -Al(111)/ γ -Al₂O₃(111) multilayer where the α -Al and γ -Al₂O₃(111) have approximately the same thickness, 13.5 Å, along the crystallographic direction [111]. More specifically, the multilayer models were built using γ -Al₂O₃ slabs γ -Al₂O₃(111)a and γ -Al₂O₃(111)b showed in Fig 2.3; those were joined to α -Al(111) slabs using the configurations α -Al(111)₁ and α -Al(111)₂. α -Al(111)₁ represents a 8 layer

α -Al(111) slab after a $C_4=90^\circ$ rotation, while α -Al(111)₂ represents a 7 layer α -Al(111) slab without any rotation. In addition, the some Al atoms at the interface were removed and the remaining moved by hand to resembling the bulk environment of the γ -Al₂O₃ phase (*cf.* Fig. 3.4).

Table 3.2: Crystallographic data for the initial configuration of the interface models

Model	size (atoms)	$a(\text{\AA})$	$b(\text{\AA})$	c/a	$\alpha = \beta = \gamma(^{\circ})$	Volume (\AA^3)
A1	120	9.691	5.642	3.01	90	1597.08
A2	132	9.691	5.642	3.01	90	1592.94
B1	118	9.691	5.642	2.83	90	1504.42
B2	128	9.691	5.642	2.83	90	1501.40

Figure 3.4 and Table 3.2 show the initial configuration and crystallographic data for the four multilayer models analyzed in this thesis, where A1 represents α -Al(111)₁/ γ -Al₂O₃(111)a, A2 represents α -Al(111)₂/ γ -Al₂O₃(111)a, B1 represents α -Al(111)₁/ γ -Al₂O₃(111)b, and B2 represents α -Al(111)₂/ α -Al(111)b.

The search for the most stable atomic configuration followed three stages. 1. In the first stage, a set of CONTCAR files were obtained for different volumes close to the initial volume given by each of the structures of Fig 3.4. For this, a relaxation was performed for each of the volumes using cutoff energy of 700 eV and a k -point mesh of $(3 \times 5 \times 1)$.

2. In the second stage, we used the previous CONTCAR files to performing simulated annealing in order to solve the metal/oxide atomic interface. The systems were heated to 1000 K and then cooled down to O K, followed by full relaxation. For the annealing process, and the relaxation, a cutoff energy of 700 eV and a k -point mesh of $(3 \times 4 \times 1)$ were used to speed up the simulations. Then we selected, for each multilayer model, the structure with the lowest energy. In other words, we selected the CONTCAR file with the lowest convergence energy after relaxation and used as input structure in the next stage, for each multilayer model.

3. In the third stage, we proceed to compute the EOS and the ground state state properties of the optimal multilayer model. For this, we start considering the CONTCAR files of the previous stage as input; then we performed a new relaxation for a series of volume values. We used a cutoff energy of 700 eV and a k -point mesh of $(3 \times 5 \times 1)$. Then, we obtain the data necessary to compute the EOS using the third order Birch-Murnaghan (BM) equation, and finally obtain the optimal volume for each of the interface models. Using this optimal volume, we proceed to calculate the structural, electronic and mechanical properties of each multilayer model.

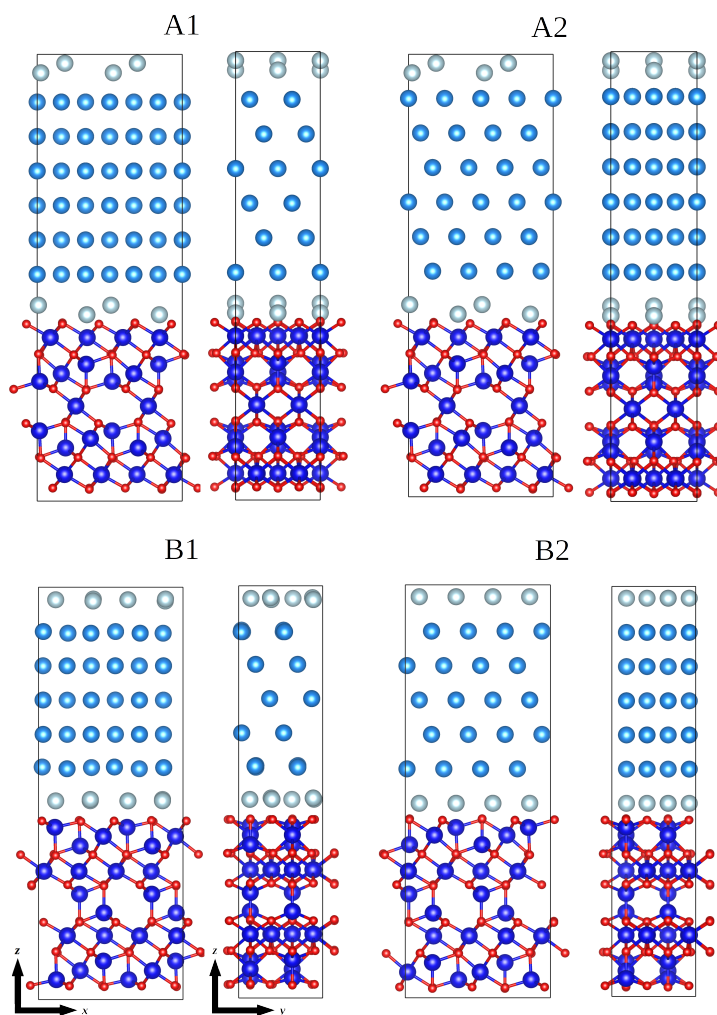


Figure 3.4: Initial configuration for the α -Al/ γ -Al₂O₃ interface models. A1 represents α -Al(111)₁/ γ -Al₂O₃(111)a, A2 represents α -Al(111)₂/ γ -Al₂O₃(111)a, B1 represents α -Al(111)₁/ γ -Al₂O₃(111)b, and B2 represents α -Al(111)₂/ α -Al(111)b; the blue and red spheres represent the Al _{γ} and O of the γ -Al₂O₃. The light blue spheres represent the Al _{α} of the α -Al, and the cyan spheres represent the Al atoms at the interface, Al _{i} . In all the figures, the black box delimits the periodic supercell.

3.1.3 Mechanical properties

Birch-Murnaghan equation of state

The equation of states (EOS) describes the properties of a system mathematically at certain thermodynamical conditions such as total energy E , volume V temperature T and pressure P . The EOS is efficiently obtained by numerical fitting of the calculated E as a function of the volume V . Solids are characterized under high pressures using the isothermal BM EOS.

The third order BM EOS^{57,58} is widely used in DFT studies. It is based on Taylor's expansion of the energy in terms of the finite strain in the crystal. It is represented as follows,

$$E(V) = E_0 + \frac{9V_0B_0}{16} \left\{ \left[\left(\frac{V_0}{V} \right)^{2/3} - 1 \right]^3 B'_0 + \left[\left(\frac{V_0}{V} \right)^{2/3} - 1 \right]^2 \left[6 - 4 \left(\frac{V_0}{V} \right)^{2/3} \right] \right\} \quad (3.1)$$

where, E_0 represents the ground state energy, V_0 is the ground state volume, V the volume of the studied solid, B_0 is the bulk modulus, and B'_0 is the bulk modulus pressure derivative. Therefore, the optimal volume can be figure out as the volume that corresponds to the total energy minimum of the BM EOS. Furthermore, the bulk modulus is defined as,

$$B_0 = \left[V \frac{\partial^2 E(V)}{\partial V^2} \right]_{V \rightarrow V_0} \quad (3.2)$$

We used these equations to obtain the optimal structural properties of the different structures analyzed in this thesis.

Knoop and Vickers Hardness

The Knoop hardness (KH)⁵⁹ test is a measure of the microhardness of a material. In other words, it is a mechanical test used particularly for very brittle materials or thin sheets. KH test uses a pyramidal diamond tip to pressed onto the surface of the sample to measure the indentation produced. KH is calculated by dividing the load by the projected area. Experimentally, the KH is given by the formula:

$$H_K = \frac{14.229P}{d^2}, \quad (3.3)$$

here P is the indentation load, and d is the length of the long diagonal of the pyramidal shape indentation⁶⁰.

The Vickers hardness⁶¹ is a test of the hardness of a material, measured from the size of an impression generated under load by a pyramid-shaped diamond indenter. Vickers hardness is computed by dividing the force by the

contacting surface area. Experimentally, the Vickers hardness is given by the formula:

$$H_V = \frac{1.8544F}{d^2} \quad (3.4)$$

where F is the force employed to the diamond in kilograms-force, and d is the average length of the diagonal left by the indenter in millimeters⁶⁰.

In Figure 3.5 is showed the differences between these two hardness tests.

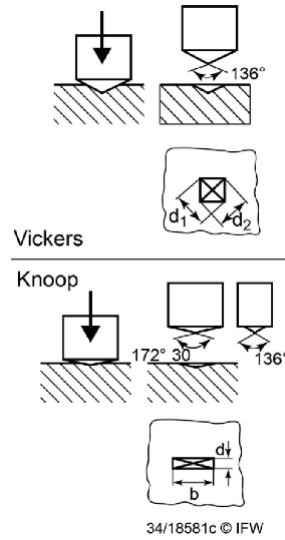


Figure 3.5: Knoop and Vickers Hardness test. Adapted from Ref. 62

In the present work, we use the method develop by Li *et al.*⁶³ and later by Lyakhov and Oganov⁶⁴ to calculate the KH. This method involves the knowledge of the optimal crystal structure that DFT can compute with high accuracy. Then, the KH is calculated using the formula:

$$H_K(\text{GPa}) = \frac{423.8}{V} n \left(\prod_n^{k=1} N_k X_k e^{-2.7f_k} \right)^{1/n} - 3.4 \quad (3.5)$$

where V is the volume of the unit cell and N_k is the number of bonds of the type k in the unit cell. X_k and f_k are the electron-holding energy of the bond k and its ionicity indicator, which are defined as in the original work of Ref. 63 as,

$$X_k = \sqrt{\frac{X_i^k X_j^k}{CN_i^k CN_j^k}}; \quad f_k = \frac{X_i^k - X_j^k}{4\sqrt{X_i^k X_j^k}} \quad (3.6)$$

X_i^k, X_j^k are the electronegativities of atoms i, j in bonds as defined by Ref. 64. CN_i^k, CN_j^k are effective coordination numbers of atoms i and j defined as $CN_i^k = v_i/s_i^k$, where v_i is the valence of atom i , and s_i^k is the bond valence computed using the classical Brown's bond valence model⁶⁵,

$$s_i^k = \frac{v_i \cdot e^{(-\Delta_k/0.37)}}{\sum_{k'} e^{(-\Delta_{k'}/0.37)}} \quad (3.7)$$

here the sum goes over all bonds k' in which atom i participates, Δ is deviation from reference covalent bond length. The calculated hardness has units of Giga Pascal (GPa). Table 3.3 shows some hardness values for different materials using the Lyakhov and Oganov⁶⁴ method compared with experimental data.

Table 3.3: Hardness of different materials in GPa using Knoop hardness test: theory H_K versus experiment. Adapted from Ref. 64.

Material	H_K (GPa)	Expt.
Diamond	89.7	90
Graphite	0.17	0.14
Rutile, TiO ₂	14	8-11
β -Si ₃ N ₄	23.4	21
Stishovite, SiO ₂	33.8	32
α -Al	1.03 ⁺	0.25-1.09*
γ -Al ₂ O ₃	22.26 ⁺	19-20.29*

* Data obtained from references: 66–68.

+ Data obtained in the present work.

Cohesive energy

The cohesive energy of a solid refers to the energy required to separate its constituent atoms and isolated them to an assembly of neutral free atoms⁶⁹. The cohesive energy is defined as follows³⁷:

$$E_{\text{coh}} = \sum_i E_i^{\text{isolated}} - \frac{E_{\text{solid}}}{N} \quad (3.8)$$

where i represent the different atoms that constitute the solid, and N represent the total number of atoms in the solid. We used this equation to calculate the cohesive energy of structures analyzed in this work.

Interface energy

Interface energy γ_{int} explains the interaction between two materials A and B to form an A/B interface⁷⁰. A different way to view the γ_{int} , is the energy involve to built the interface A/B from the bulk material A an B. Therefore, this energy associates the interfacial bonds to the bonding of the bulk material. Consequently, the interface energy can be defined as⁷¹:

$$\gamma_{\text{int}} = \frac{E_{A/B} - N_A E_{A,\text{bulk}} - N_B E_{B,\text{bulk}}}{2A} \quad (3.9)$$

where N_A and $E_{A,\text{bulk}}$ (N_B and $E_{B,\text{bulk}}$) are the number of atoms and bulk energy of system A (B), $E_{A/B}$ is the total energy of the interface system, A is the interfacial area, and the factor 2 accounts for the two identical interfaces in the multilayered composite. Notice that this estimation does not take into account the vibrational energy contribution as is expected to be small compared with the 0 K energies that VASP computes.

Equation 3.9 was used to obtain the interface energy in order to describe the metal/oxide interface described in this work.

Chapter 4

Results & Discussion

The Results & Discussion chapter is divided in three main sections: the first section presents and discusses the computed structural, mechanical, and electronic properties of both the α -Aluminum (α -Al), and γ -Alumina (γ -Al₂O₃) bulk structure. The second section corresponds to the results and discussions of the structural, mechanical, and electronic properties of the four interface models A1, A2, B1, and B2. Finally, the last section compares and discusses the results with experimental data.

4.1 The α -Al and γ -Al₂O₃ bulk properties

4.1.1 Structural and mechanical properties

We start considering the calculation of fcc α -Al crystal using PBEsol with VASP. The EOS is displayed in Fig. 4.1, from this result we obtained the optimal structure for α -Al as displayed in Table 4.1

Table 4.1: PBEsol computed crystallographic data for optimal primitive cell of α -Al; here u , v and w are in fractional coordinates

Property		Calculated (PBEsol)		
Space group		$Fm\bar{3}m$		
$a = b = c$ (\AA)		2.840		
$\alpha = \beta = \gamma$ ($^\circ$)		60		
Volume (\AA^3)		16.198		
B_0 (GPa)		81.59		
Sites	u	v	w	
Al	0.0	0.0	0.0	

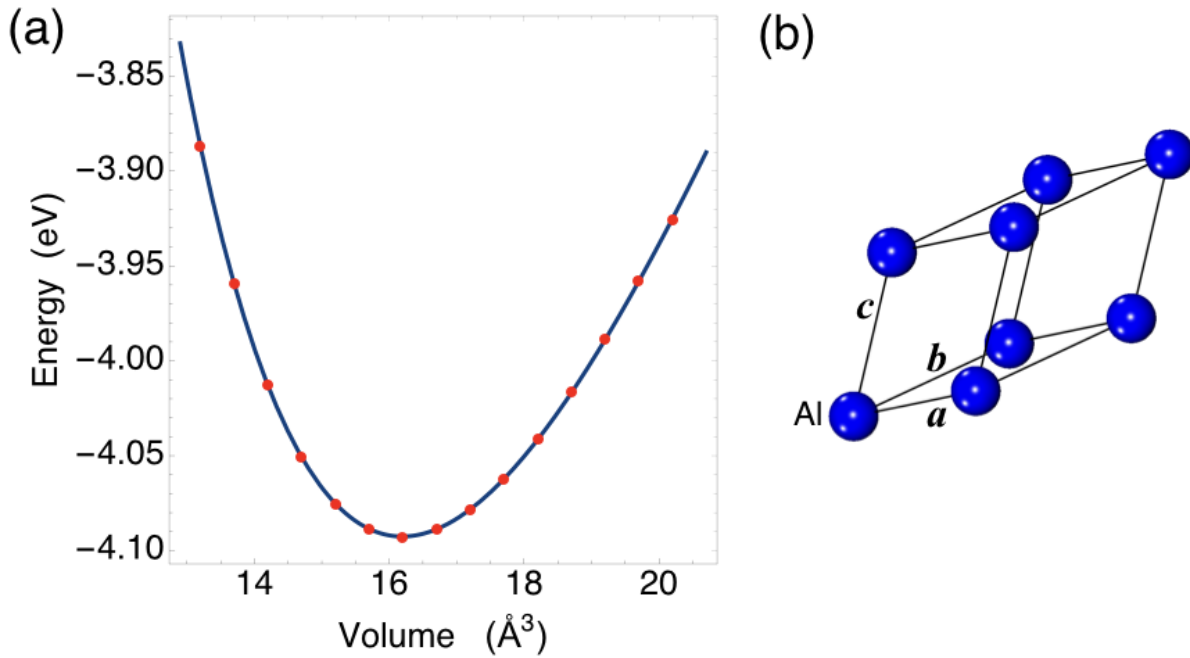


Figure 4.1: (a) PBEsol computed EOS for α -Al using the optimal parameters as displayed in Table 3.1. The red dots are the computed values and the blue curve is the fitted function using the third-order BM EOS from Eq. 3.1. (b) Optimal primitive cell of fcc α -Al, the details of this structure is presented in Table 4.1.

In the same fashion, in Fig. 4.2 is shown the PBEsol computed EOS for the monoclinic γ - Al_2O_3 bulk structure, from this result is estimated the optimal structure which crystallographic data is displayed in Table 4.2.

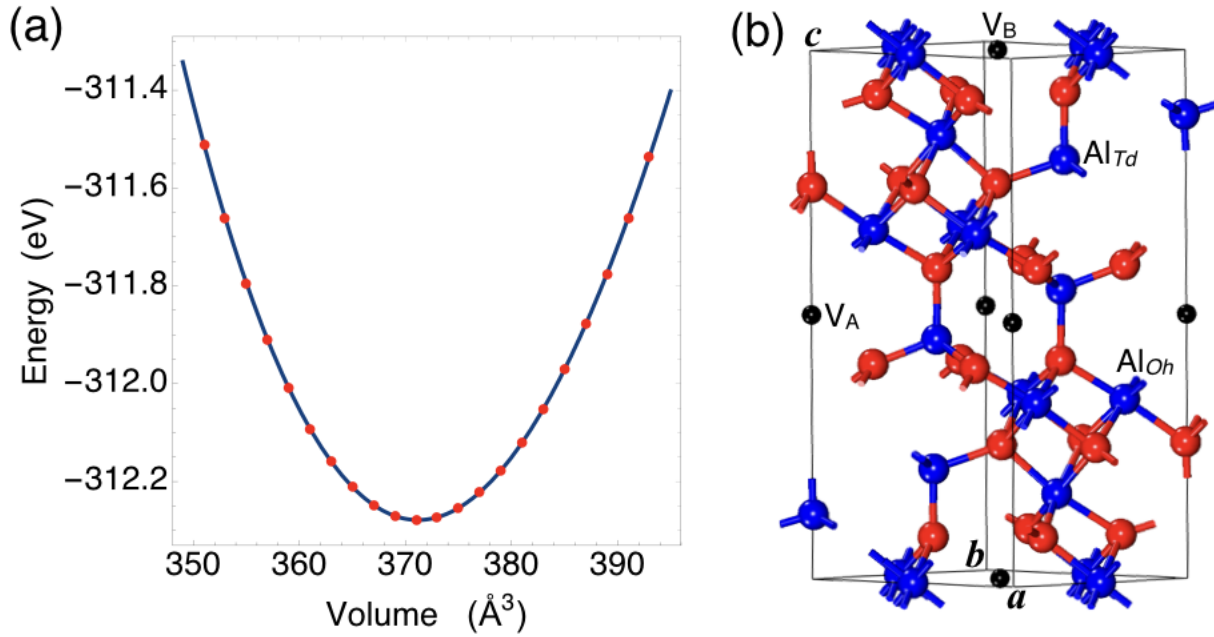


Figure 4.2: (a) PBEsol computed EOS for monoclinic γ - Al_2O_3 using the optimal parameters as displayed in Table 3.1. The red dots are the computed values and the blue curve is the fitted function using the third-order BM EOS, Eq. 3.1. (b) Optimal primitive cell of γ - Al_2O_3 . The red and blue spheres represent the O and Al atoms, while the black spheres represent the Al-vacancies sites, V_A and V_B .

Table 4.2: PBEsol computed crystallographic data for optimal primitive cell of γ -Al₂O₃; here u , v and w are in fractional coordinates. The location of the Al vacancies are also included for reference.

Property	Calculated (PBEsol)		
Space group	$C2/m$		
$a = b$ (Å)	5.607		
c (Å)	13.578		
$\alpha = \beta$ (°)	90.58		
γ (°)	60.41		
Volume (Å ³)	371.191		
B_0 (GPa)	204.05		
Sites	u	v	w
Al _{Td}	0.3242	0.3242	-0.7926
Al _{Td}	0.0029	0.0029	-0.8776
Al _{Td}	0.6666	0.6666	-0.4527
Al _{Oh}	0.6759	0.1653	-0.3399
Al _{Oh}	0.6522	0.6522	-0.8396
Al _{Oh}	0.1661	0.1661	-0.3392
Al _{Oh}	0.0	0.5	0.0
O	0.8445	0.3465	-0.9141
O	0.4888	0.0322	-0.2545
O	0.8366	0.3313	-0.4064
O	0.8229	0.8229	-0.9163
O	0.6785	0.6785	-0.0790
O	0.4944	0.4944	-0.2526
O	0.8360	0.8360	-0.4063
O	0.3357	0.3357	-0.4126
O	0.0036	0.0036	-0.2582
V _A	0.0	0.0	0.5
V _B	0.5	0.5	0.0

A summary of some computed properties of α -Al and γ -Al₂O₃ crystals are given in Table 4.3. The obtained bulk modulus B_0 by using Eq. 3.2 for both structures suggest that γ -Al₂O₃ is more resistance to compression than α -Al, also the obtained cohesive energy E_{coh} indicates that it requires more energy to split γ -Al₂O₃ crystal to its atomic constituents than for the fcc α -Al crystal. According to Ref. 72, insulators, as γ -Al₂O₃, have high cohesive energies because these solids are bounded strongly and have great mechanical strength. On the contrary, metals with electrons in sp-bond, as α -Al, have tiny cohesive energies because this type of metallic bond is weak. As a result, metals such as aluminum or magnesium should be alloyed with other metals with strong metallic bonds. In addition, E_{coh} is independent of the crystal arrangement in metals bound with the electrons from sp-shells⁷². The computed Knoop hardness H_K from Eq. 3.5 suggests that γ -Al₂O₃ is harder than the α -Al structure in good agreement with the experiments.

Table 4.3: Structural and mechanical data for computed α -Al and γ -Al₂O₃. In parenthesis are the corresponding experimental values.

System	$V_0(\text{\AA}^3)$	$B_0(\text{GPa})$	$E_{coh}(\text{eV/atom})$	$H_K(\text{GPa})$
α -Al	16.198	81.59 (69 ± 4) ⁷³	3.89 (3.39) ³⁷	1.03 (0.25-1.09) ^{66,67}
γ -Al ₂ O ₃	371.191 (371.35) ⁷⁴	204.05 (250 ± 9) ⁷⁵	5.76	22.26 (19-20.29*) ^{66,68}

* Data for corundum α -Al₂O₃.

Our α -Al cohesive energy is in agreement with other theoretical results, refs.: 37,76. Furthermore, the structural properties obtained for the fcc α -Al are similar to the data for aluminum⁷⁷ storage in Materials Project⁷⁸ database. Our calculated crystal lattice constant, and bulk modulus B_0 for the γ -Al₂O₃ are similar to some theoretical and experimental values, refs.: 16–18,79–81. Finally, the value of the Knoop hardness (KH), H_K , for the γ -Al₂O₃ is in good agreement to the measured value for corundum α -Al₂O₃ that ranges between 19 to 20.29 GPa^{66,68}. In overall the predicted values are in good agreements with experiments and other theoretical studies, thus these results validate our theoretical approach to the structural and electronic structures of the multilayered models studied in this work.

4.1.2 Electronic properties

The PBEsol computed density of states (DOS) for the bulk α -Al, and γ -Al₂O₃ are plotted in Fig 4.3, where the Fermi level E_F is aligned to 0 eV on the x -axis.

The computed DOS for the α -Al (Fig. 4.3(a)) is nonzero at the Fermi energy, confirming that Al is metallic.

The bottom of the band below E_F has mainly Al-3s character, whereas, above E_F , the band has a combination of Al 3s+3p states (*cf.* Fig. A.1). The computed band structure is displayed in Fig. A.20.

The DOS for the γ -Al₂O₃ is shown in Fig. 4.3(b). The system is an insulator with a band gap of 4.1 eV; this value is in agreement with other theoretical calculations, refs.: 17,18,80. The lower valence band (LVB), located in the energy range between -20.4 and -16.4 eV, has mainly an O-2s character. The upper valence band (UVB), located within the energy range -8.6 eV to E_F is formed mainly by O-2p states with a minor contribution of Al 3s+3p states. The lower part of the conduction band (CV), the electronic structure has a composition of Al 3s+3p and O 2s+2p states (*cf.* Fig. 4.3(b) and Figs. A.3, A.5). The computed band structure is showed in Fig. A.21, it presents a direct band gap of 4.1 eV along the Γ point; the reported experimental value is 8.5 eV⁸², a well known limitation of standard DFT calculations. Moreover, the flatness of the occupied bands at E_F reflects the electron localization on the O-2p orbitals near to the vacancy sites V_{A,B}.

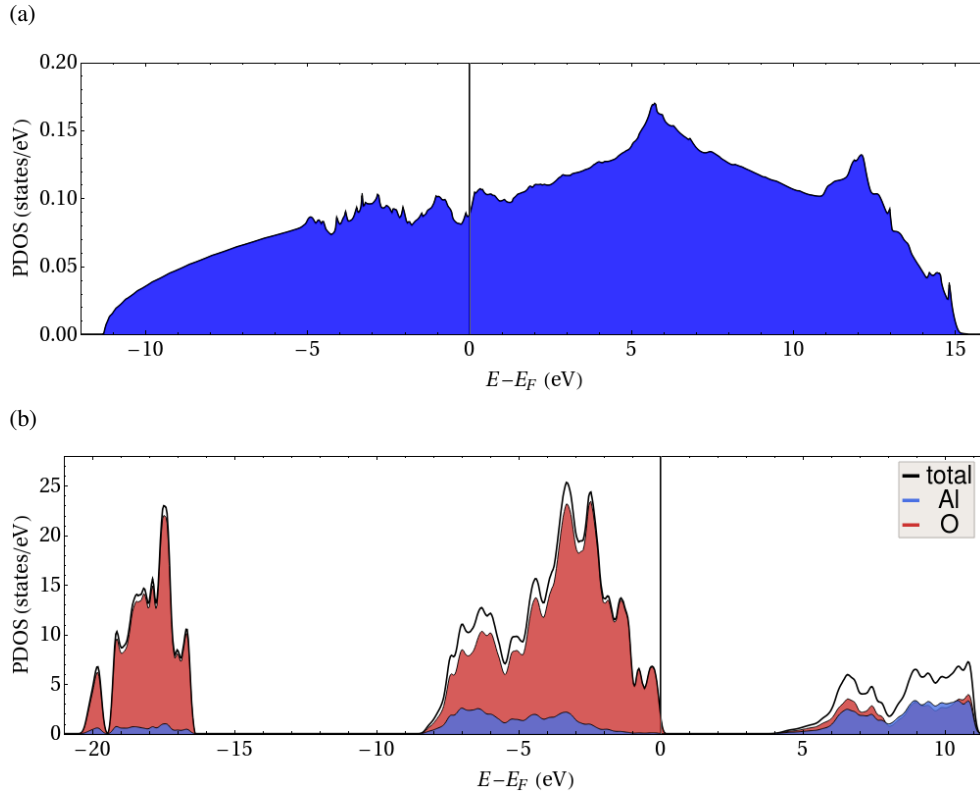


Figure 4.3: PDOS for a) α -Al and b) γ -Al₂O₃. The Fermi level is represented as a black solid line.

4.2 α -Al/ γ -Al₂O₃(111) multilayer models

4.2.1 Structural and mechanical properties

The PBEsol computed optimal structures for multilayer models are shown in Table 4.4, whereas the computed mechanical properties are shown in Table 4.5. The final structure configuration for the four models is illustrated in part a) of Figures 4.4, 4.6, 4.8, 4.10.

In Table 4.4, all the computed optimal multilayer models have a space group $P1$. The lattice parameters a and b of all the optimal models almost remain constant in comparison to the original configuration (*cf.* Table 3.2), while the ratio c/a changes in the multilayer models A1 and B1. We noticed that in the structures A1 and B1, the lattice angles change more than in the other models, especially in A1. The optimal volume of the models shows the following trend: $V_0(\text{B1}) < V_0(\text{A1}) < V_0(\text{B2}) < V_0(\text{A2})$.

Table 4.4: PBEsol computed optimal structural properties obtained from the final atomic configuration of the multilayer models. All the structures belong to a monoclinic $P1$ space group.

Model	$a(\text{\AA})$	$b(\text{\AA})$	c/a	$\alpha(^{\circ})$	$\beta(^{\circ})$	$\gamma(^{\circ})$	$V_0(\text{\AA}^3)$
A1	9.543	5.606	2.83	93.1	92.3	90.0	1439.88
A2	9.673	5.606	3.12	90.1	87.2	90.0	1634.55
B1	9.694	5.608	2.62	96.4	92.6	90.0	1372.42
B2	9.784	5.628	2.84	90.0	93.6	90.0	1527.34

According to Table 4.5, among the composites, B2 has the highest B_0 . Moreover, the bulk modulus shows the trend $B_0(\alpha\text{-Al}) < B_0(\text{A1}) < B_0(\text{A2}) < B_0(\text{B1}) < B_0(\text{B2}) < B_0(\gamma\text{-Al}_2\text{O}_3)$. This means that the resistance to compression of the multilayered $\alpha\text{-Al}/\gamma\text{-Al}_2\text{O}_3(111)$ shows values in between their parents $\alpha\text{-Al}$ and $\gamma\text{-Al}_2\text{O}_3$, *i.e.*, the composite enhance B_0 compared to $\alpha\text{-Al}$ alone. The computed micro hardness H_K present the trend $H_K(\alpha\text{-Al}) < H_K(\text{A1}) < H_K(\text{A2}) < H_K(\text{B1}) < H_K(\text{B2}) < H_K(\gamma\text{-Al}_2\text{O}_3)$; the model B2 as the hardness composite but again the values of H_K for $\text{Al}/\gamma\text{-Al}_2\text{O}_3(111)$ models indicates that the composite is harder than $\alpha\text{-Al}$ alone but softer than pristine $\gamma\text{-Al}_2\text{O}_3$. Interestingly, we notice a proportionality between B_0 and H_K ; the higher the bulk modulus the higher the Knoop hardness. The trend for the computed cohesion energy is $E_{\text{coh}}(\gamma\text{-Al}_2\text{O}_3) < E_{\text{coh}}(\text{B1}) < E_{\text{coh}}(\text{B2}) < E_{\text{coh}}(\text{A2}) < E_{\text{coh}}(\text{A1}) < E_{\text{coh}}(\alpha\text{-Al})$; this indicates that model B1 has the higher value among the composites but certainly lower than the pristine $\gamma\text{-Al}_2\text{O}_3$. It is important to recall that E_{coh} is related with the bonding strength of

the material. The interfacial energy trend is $\gamma_{\text{int}}(\text{A2}) < \gamma_{\text{int}}(\text{B2}) < \gamma_{\text{int}}(\text{A1}) < \gamma_{\text{int}}(\text{B1})$, suggesting how likely is to form a given multilayer $\alpha\text{-Al}/\gamma\text{-Al}_2\text{O}_3(111)$ compound under the same conditions of annealing and layer thickness; basically the lower the value the higher probability to form the composite; then the results suggest the system B1 as the most likely structure to be formed and A2 is the less favorable. Finally, we observe the following trend in the density $\delta(\alpha\text{-Al}) < \delta(\text{A2}) < \delta(\text{A1}) < \delta(\text{B2}) < \delta(\text{B1}) < \delta(\gamma\text{-Al}_2\text{O}_3)$; the composite A2 is the less dense; in general, all the composites have densities in between their parents. It is important to stress the importance of light and strong materials based on aluminum for applications in the automotive and aerospace industry.

Table 4.5: PBEsol computed mechanical properties obtained from the optimal structure of the interface models, we include the values for bulk $\alpha\text{-Al}$ and $\gamma\text{-Al}_2\text{O}_3$ from Table 4.3 for easy comparison. The values of the total energy E_s are displayed for reference only.

System	B_0 (GPa)	H_K (GPa)	E_s (eV)	E_{coh} (eV/atom)	δ (g/cm ³)	γ_{int} (eV/Å ²)
A1	108.47	6.672	-718.43	3.95	3.13	20.82
A2	112.04	8.471	-829.75	4.24	3.08	22.79
B1	113.07	8.505	-771.05	4.49	3.21	19.65
B2	128.98	12.11	-810.65	4.29	3.18	21.17
$\alpha\text{-Al}$	81.59	1.03	-4.09	3.89	2.77	-
$\gamma\text{-Al}_2\text{O}_3$	204.05	22.26	-312.27	5.76	3.65	-

4.2.2 Electronic properties

A1 model

DOS and partial density of states (PDOS): The PBEsol computed DOS and PDOS for the optimal structure for the multilayered A1 model is displayed in Figure 4.4 b). We can note that the system is metallic, there is not an energy gap between the conduction and valence band in the total DOS, black solid line. The LVB, located within the energy range -23 to -19 eV, has mainly a O-2s character with a very small contribution of 3s+3p states for the Al_γ and Al_i (see Fig. A.7). The band within -11 to 4.9 eV is crossed by the Fermi level at 0 eV. The occupied states are formed mainly by O-2p states with minor contribution of Al_γ , Al_α and Al_i 3s+3p states. Interestingly, we observe a depletion of O-2p+ Al_γ 3s+3p states within the range from -2.2 to 2.1 eV where dominates the Al_α -3s+3p. Above 2.7 eV, the electronic structure has a composition of a combination of Al_α 3s+3p, Al_γ 3s+3p and small contribution of

Al_i 3s+3p states. The band structure for model A1 is showed in Fig. A.22, which confirms the analysis of the PDOS.

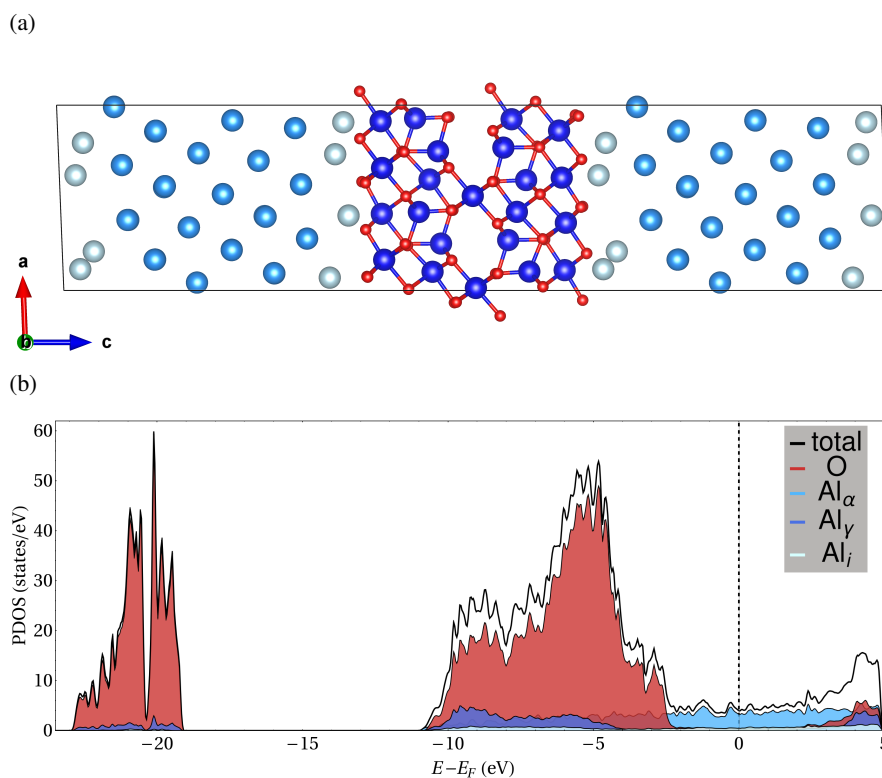


Figure 4.4: PBEsol predicted A1 model. (a) Optimal crystal structure; the blue and red spheres represent the Al_γ and O of the γ - Al_2O_3 . The lightblue spheres represent the Al_α of the α -Al and the cyan spheres represent the Al atoms in the interface, Al_i . The black box delimits the periodic supercell. (b) PBEsol computed PDOS, the Fermi level is represented as a black dashed line.

Electron charge density: Figure 4.5 shows the electron charge density for the optimal structure A1 model. The electron density contours are displayed from 0 to $1.2 e/\text{\AA}^3$. We note first the difference between the metal, oxide and interfacial regions. In the α -Al metal region there is no evidence of strongly localized electrons, $0.2 e/\text{\AA}^3$. This is characteristic of the homogeneous electrons gas and metallic bonding. In contrast, γ - Al_2O_3 consist mainly of regions of low charge density, $0.1 e/\text{\AA}^3$, with most electrons localized on the O atoms. This implies some ionic type of bonding. The interfacial region, the black rectangle in Fig. 4.5 a), b), d) gives evidence for a directional Al-Al bonding with some covalent character across the metal/ceramic interface. This can be seen in the Fig. 4.5 c).

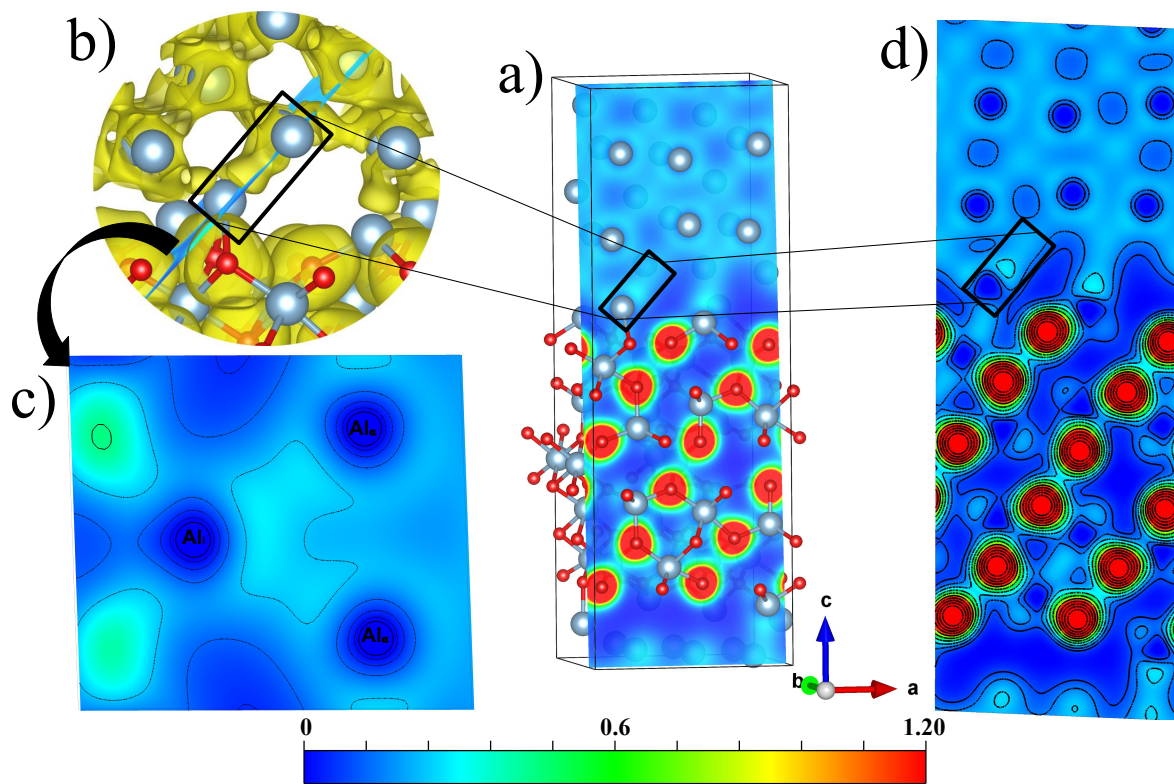


Figure 4.5: Electron charge density for A1 model. (a) Electron charge density across (010) plane crossing certain Al and O atoms.. The light blue and red spheres represent the Al and O atoms. (b) Close-up of section showing a iso-charge density in yellow for the A_{v} and A_{i} bond. (c) Contour plot across a plane showing the electron charge density in the interface region pointed by the black arrow in (b). (d) Contour plot of electron charge density across (010) plane as displayed in (a). The colored scale bar below ranges between 0 to $1.20 e/\text{\AA}^3$

A2 model

DOS and PDOS: The PBEsol computed DOS and PDOS for the optimal structure for the multilayered A2 model is displayed in Figure 4.6 b). The system is metallic, as we can see in the total DOS. The LVB, located within the energy range -23.6 to -20 eV, has mainly a O-2s character. The band within -11.6 to 4.4 eV is crossed by the Fermi level at 0 eV. The occupied states are formed mainly by O-2p states with minor contribution of Al_γ , Al_α and Al_i 3s+3p states. In the A2 model, we observe the depletion of O-2p+ Al_γ 3s+3p states within the range from -3.2 to 1.2 eV where dominates the Al_α -3s+3p. Above 1.3 eV, the electronic structure has a composition of a combination of Al_α 3s+3p, Al_γ 3s+3p and small contribution of Al_i 3s+3p states (*cf.* Figs. A.9 to A.11). The band structure for model A2 is showed in Fig. A.23, which confirms the analysis of the PDOS.

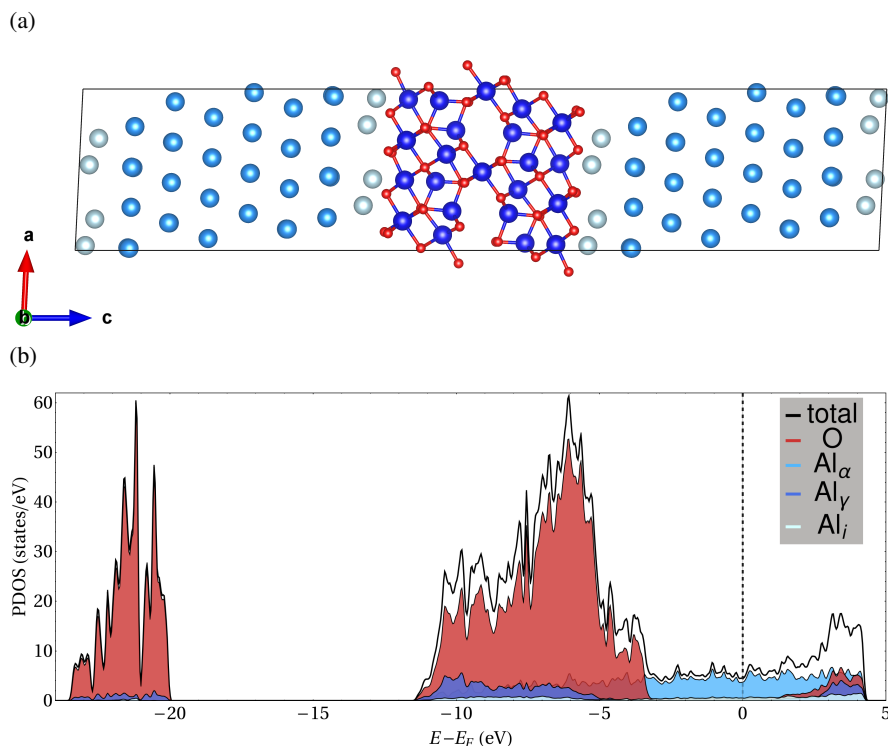


Figure 4.6: PBEsol predicted A2 model. (a) Optimal crystal structure; the blue and red spheres represent the Al_γ and O of the γ - Al_2O_3 . The lightblue spheres represent the Al_α of the α -Al and the cyan spheres represent the Al atoms in the interface, Al_i . The black box delimits the periodic supercell. (b) PBEsol computed PDOS, the Fermi level is represented as a black dashed line.

Electron charge density: Figure 4.7 shows the electron charge density for the optimal structure A2 model. The electron density contours are displayed from 0 to $1.2 e \text{ \AA}^{-3}$. We note first the difference between the metal, oxide and interfacial region layers. In the α -Al metal region there is a homogeneous distribution of electron density, characteristic of a metallic bonding. The γ -Al₂O₃ the electron density is mostly localized on the O atoms suggesting some ionic type of bonding. The interfacial region, the black rectangle in Figs. 4.7 a), b), d) gives evidence for a directional Al-Al bonding with covalent character across the metal/ceramic interface; this is evident in Fig. 4.5 c). The covalent bond of the model A2 is the strongest one of all the interface models.

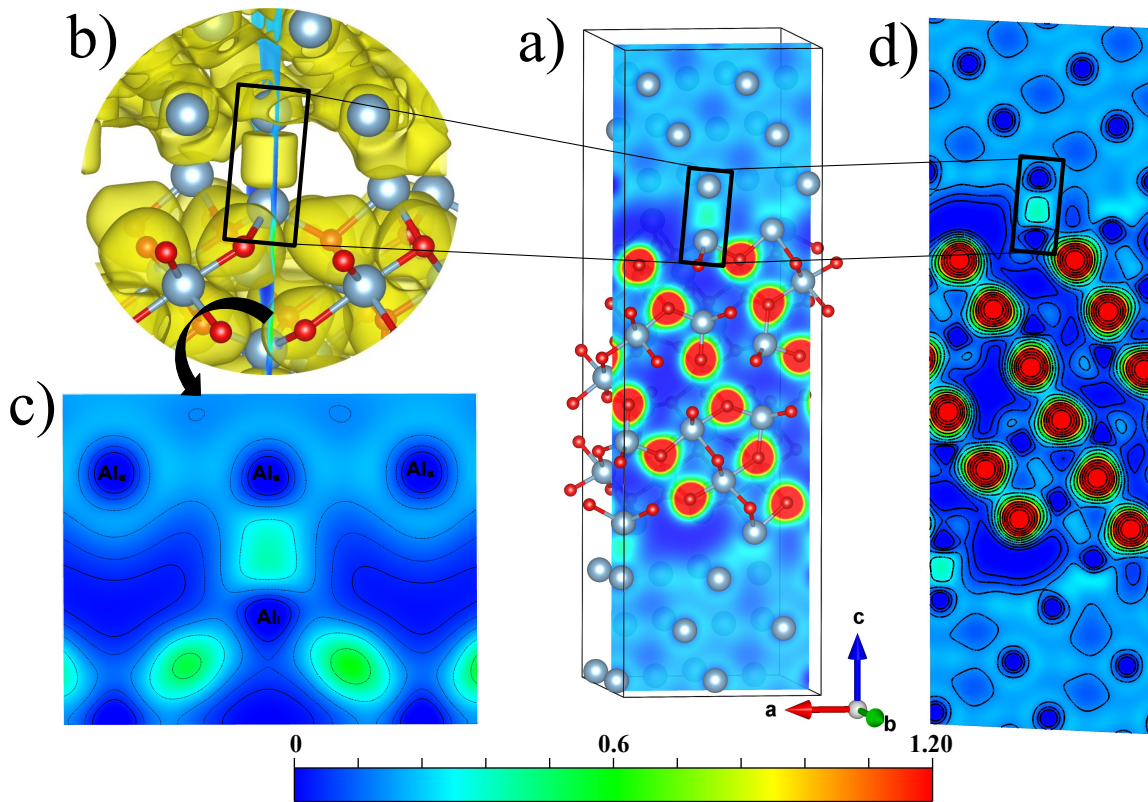


Figure 4.7: Electron charge density for A2 model. (a) Electron charge density across (010) plane crossing certain Al and O atoms. The light blue and red spheres represent the Al and O atoms. (b) Close-up of section showing a iso-charge density in yellow for the Al_α and Al_i bond. (c) Contour plot across a plane showing the electron charge density in the interface region pointed by the black arrow in (b). (d) Contour plot of electron charge density across (010) plane as displayed in (a). The colored scaled bar below ranges between 0 to $1.2 e/\text{\AA}^3$.

B1 model

DOS and PDOS: The PBEsol computed DOS and PDOS for the optimal structure of B1 model is displayed in Figure 4.8 b). We can see that the system is metallic according to the total DOS. The LVB, located within the energy range -24.3 to -20.3 eV, has mainly a O-2s character. The band within -12.1 to 4.3 eV is crossed by the Fermi level at 0 eV. The occupied states are formed mainly by O-2p states with minor contribution of Al_γ , Al_α and Al_i 3s+3p states. In the B1 model, we observe the depletion of O-2p+ Al_γ 3s+3p states within the range from -3.8 to 1.3 eV where dominates the Al_α -3s+3p. Above 1.3 eV, the electronic structure has a composition of a combination of Al_α 3s+3p, Al_γ 3s+3p and small contribution of Al_i 3s+3p states. (cf. Figs. A.13 to A.15). The band structure for model B1 is showed in Fig. A.24, which confirms the analysis of the PDOS.

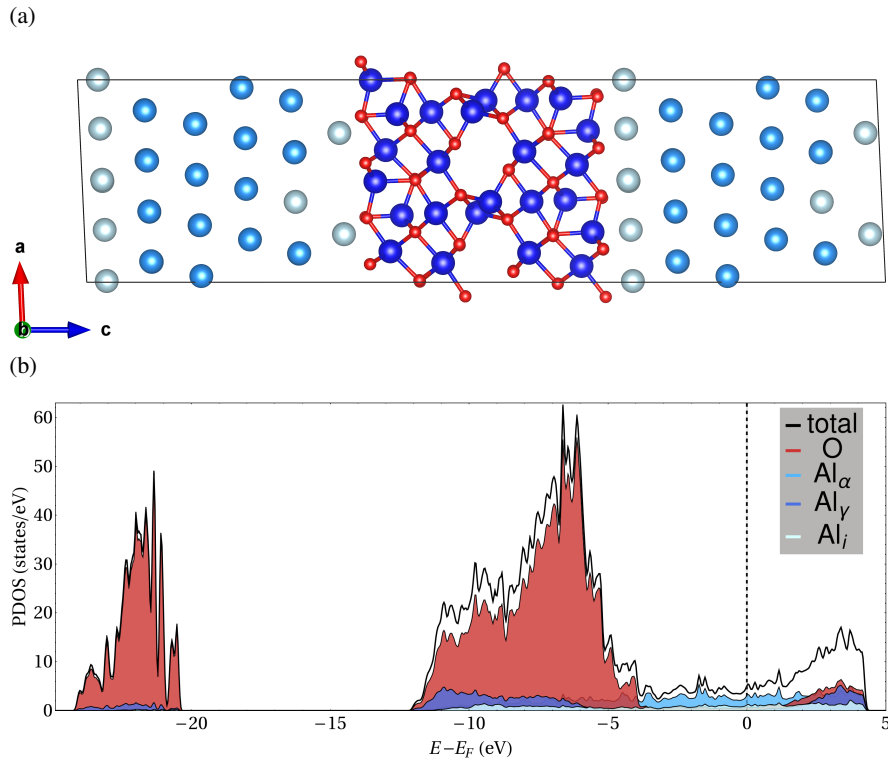


Figure 4.8: PBEsol predicted B1 model. (a) Optimal crystal structure; the blue and red spheres represent the Al_γ and O of the γ - Al_2O_3 . The lightblue spheres represent the Al_α of the α -Al and the cyan spheres represent the Al atoms in the interface, Al_i . The black box delimits the periodic supercell. (b) PBEsol computed PDOS, the Fermi level is represented as a black dashed line.

Electron charge density: Figure 4.9 shows the electron charge density for the optimal structure B1 model. The electron density contours are displayed from 0 to $1.2 e \text{ \AA}^{-3}$. Similarly to the other systems, it is clear the α -Al metal region with homogeneous electrons gas, the γ -Al₂O₃ region that shows electrons localized around the O atoms with some ionic type of bonding. Across the metal/ceramic interfacial region shows some directional bonding. The black rectangle in Fig. 4.9 a), b), d) gives evidence for a Al-Al bonding with some covalent character. This can be seen in the Fig. 4.9 c).

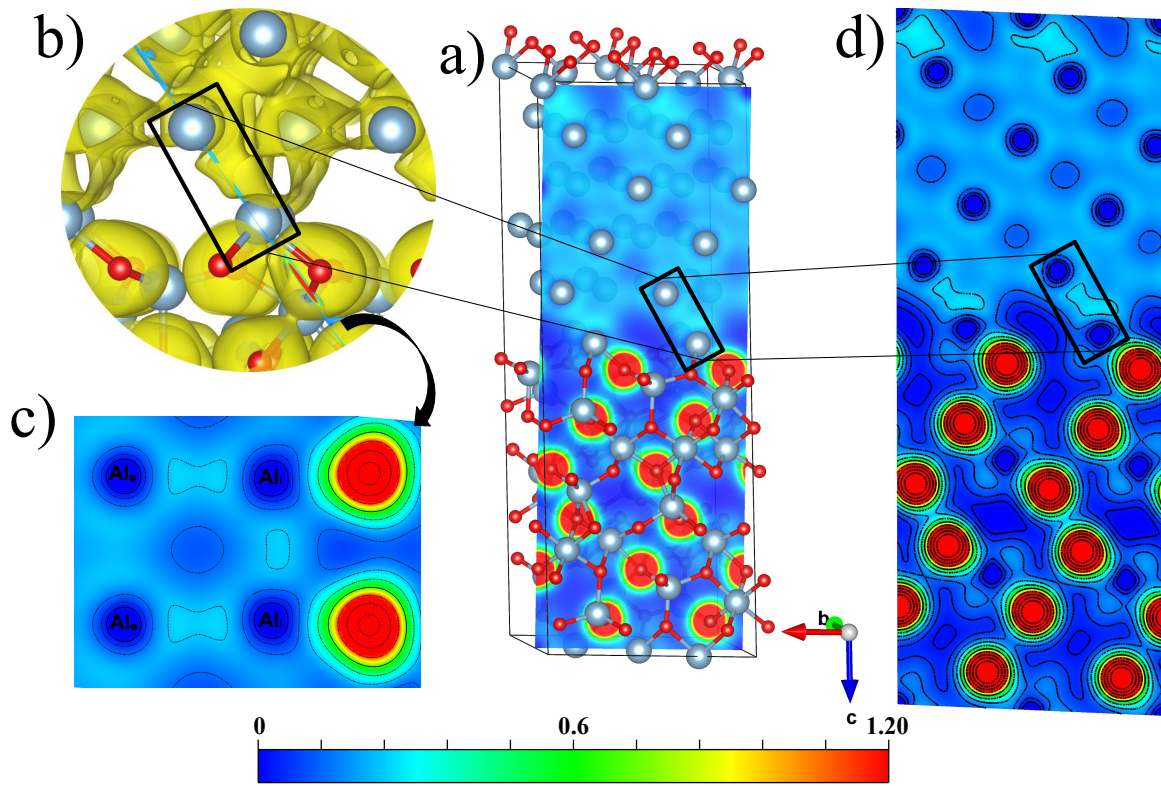


Figure 4.9: Electron charge density for B1 model. (a) Electron charge density across (010) plane crossing certain Al and O atoms. The light blue and red spheres represent the Al and O atoms. (b) Close-up section showing a iso-charge density in yellow for the A_a and A_i bond. (c) Contour plot of electron charge density across (010) plane as displayed in (a). (d) Contour plot of electron charge density across (010) plane as displayed in (a). The colored scaled bar below ranges between 0 to $1.2 e/\text{\AA}^3$.

B2 model

DOS and PDOS: The PBEsol computed DOS and PDOS for the optimal structure of B2 model is displayed in Figure 4.10 (b). The system is also metallic. The LVB, located within the energy range -24.6 to -21.1 eV, has mainly a O-2s character with a very small contribution of 3s+3p states for the Al_γ and Al_i (see Fig. A.11). The band within -12.5 to 3.9 eV is crossed by the Fermi level at 0 eV. The occupied states are formed mainly by O-2p states with minor contribution of Al_γ , Al_α and Al_i 3s+3p states. The B2 depletion of O-2p+ Al_γ 3s+3p states is within the range from -4.5 to 0.6 eV where dominates the Al_α -3s+3p. Above 1.6 eV, the electronic structure has a composition of a combination of Al_α 3s+3p, Al_γ 3s+3p and small contribution of Al_i 3s+3p states (*cf.* Figs. A.17 to A.19). The band structure for model B2 is showed in Fig. A.25, which confirms the analysis of the PDOS.

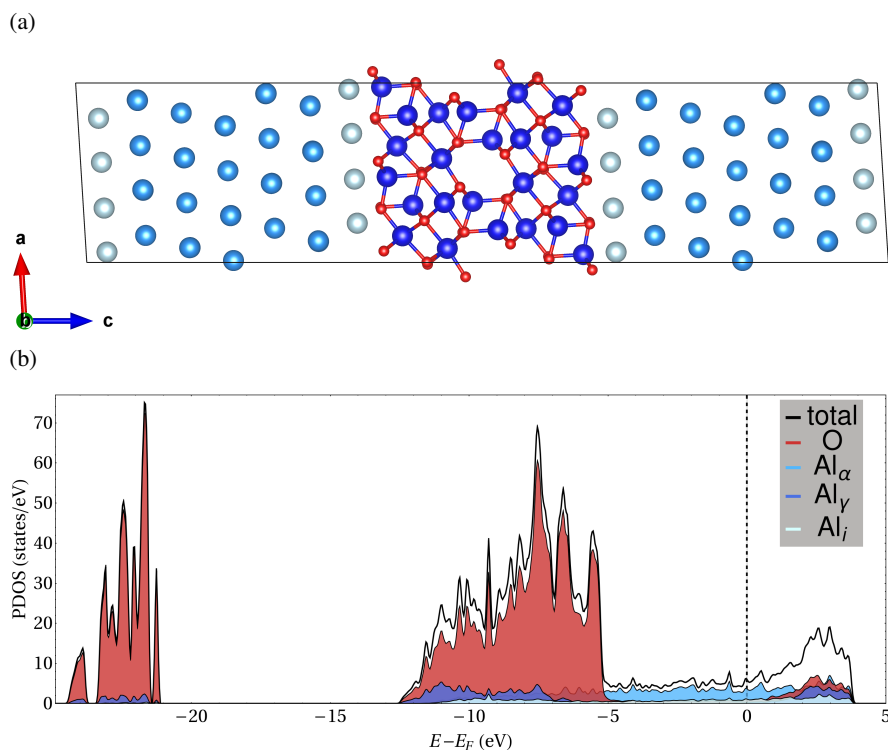


Figure 4.10: PBEsol predicted B2 model. (a) Optimal crystal structure; the blue and red spheres represent the Al_γ and O of the γ - Al_2O_3 . The lightblue spheres represent the Al_α of the α -Al and the cyan spheres represent the Al atoms in the interface, Al_i . The black box delimits the periodic supercell. (b) PBEsol computed PDOS, the Fermi level is represented as a black dashed line.

Electron charge density: Figure 4.11 shows the electron charge density for the optimal structure B2 model. The electron density contours are displayed from 0 to $1.2 e \text{ \AA}^{-3}$. Similar to the other systems; there is a region of homogeneous electrons gas corresponding to α -Al, region with electrons localized on the O atoms that corresponds to the γ - Al_2O_3 region and the interfacial region showing directional bondings with some covalent character. The black rectangle in Fig. 4.11 a), b), d) gives evidence for a Al-Al bonding. This can be seen in the Fig. 4.11 c).

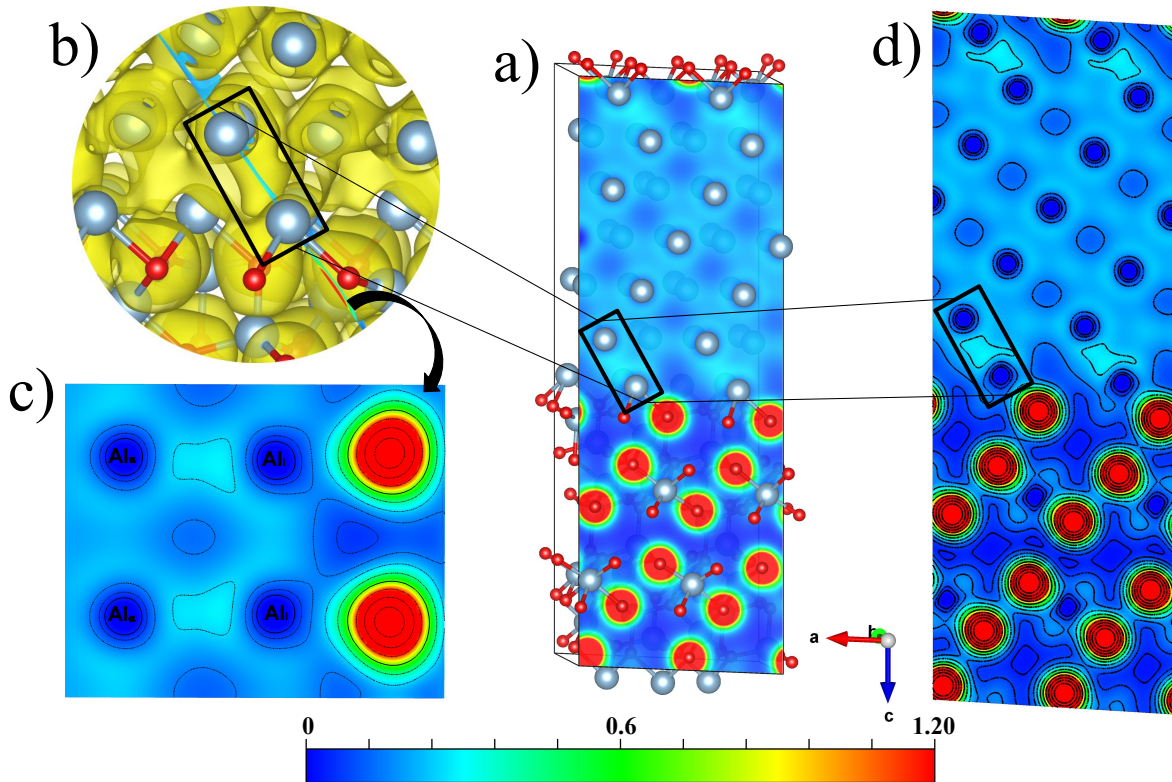


Figure 4.11: Electron charge density for B2 model. (a) Electron charge density across (010) plane crossing certain Al and O atoms. The light blue and red spheres represent the Al and O atoms. (b) Close-up section showing a iso-charge density in yellow for the A_a and A_i bond. (c) Contour plot of electron charge density across (010) plane as displayed in (a). (d) Contour plot of electron charge density across (010) plane as displayed in (a). The colored scaled bar below ranges between 0 to $1.2 e/\text{\AA}^3$.

In summary, the electronic properties of the α -Aluminum/ γ -Alumina (α -Al/ γ - Al_2O_3)(111) multilayer models show us that the composites obtain a metal-like behavior, in all the cases. According, the PDOS, there is not a

bandgap between the valence band and the conduction band. Also, the electron density of the multilayer models identifies the formation of covalent bonds between the metal and the insulator. Here, we can notice that the type of bounding of the models B1 and B2 are different from the models A1 and A2. That difference can be related to the fact that the model B2 is the hardest and the most resistant under compression. Besides, the composites have an insulator-like behavior along the c axis, but a conductive response along the planes due to α -Al phase sublayers.

4.3 Theory versus Experiment

In this section we compare the data calculated for our interface structure models with the experimental available data for the multilayered system.

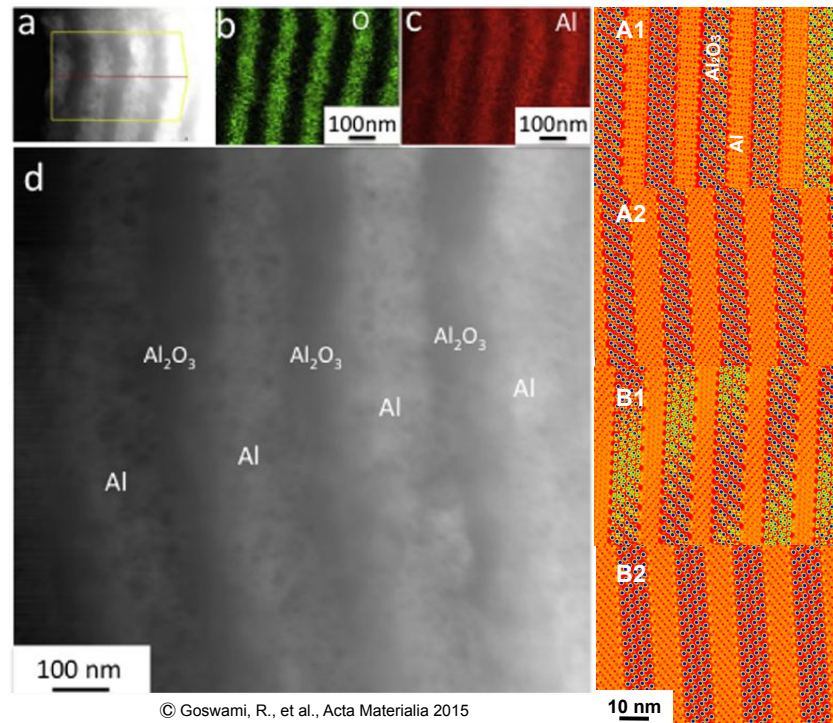


Figure 4.12: Left side: a) HAADF image of post annealed Al/Al₂O₃ multilayers, b) and c) EDS maps of Al and O. d) HAADF image showing the dark dots of Al₂O₃. Adapted from Ref. 10. Right side: theoretical multilayer α -Al/ γ -Al₂O₃(111) models; notice the scale of the layers: the thickness of the experiment, in nanometers (nm), is two orders of magnitude bigger than theoretical models.

The experimental work of Goswami *et al.*¹⁰ reported that Al/Al₂O₃ multilayers enhanced their strength after annealing, because of precipitation of extremely fine γ -Al₂O₃ in Al layers. The annealed structures of this experiment are shown in Fig. 4.12. Also, they find a value of Vickers hardness equal to 3.43 GPa for the interface. In our calculations, for the Knoop hardness we find values between 6.67 to 12.11 GPa, in particular, the B2 (A1) model shows the highest (lowest) value of hardness of 12.11 (6.67) GPa. We are aware that at the moment we can not make a direct comparison between the experiment and our models since the experiments the nanolayer thickness are two orders of magnitude larger than in our model but provides an interesting suggestion: the smaller the nanolayer thickness, the stronger can become the composite. This hypothesis is under study, we are simulating composites with twice the thickness presented in this work.

Chapter 5

Conclusions & Outlook

In this thesis, we have conducted a first-principles study of the α -Aluminum/ γ -Alumina (α -Al/ γ -Al₂O₃)(111) metal/ceramic interface using the slabs of α -Aluminum (α -Al) and γ -Alumina (γ -Al₂O₃). For this, we studied four models that describe the mechanical and electronic properties of this interface. We first validate our theoretical approach finding the optimal mechanical and electronic properties for both α -Al and γ -Al₂O₃ bulk structures, using density-functional theory (DFT). We found that the structure model we used in this thesis for γ -Al₂O₃, monoclinic spinel-based model, describes with high accuracy the structural, mechanical, and electronic properties of the γ -Al₂O₃. Then, we create our four models to describe the α -Al/ γ -Al₂O₃(111) interface. We applied simulated annealing using DFT that recreate in a significant way the experimental process to obtain multilayer α -Al/ γ -Al₂O₃ interfaces. Therefore we analyzed the data obtained from the interface models properties.

Thus, according to the mechanical properties studied, we found that although all structures have almost the same bulk modulus and microhardness, the B2 model is the most resistant under compression and the hardest. In the same way, we found that A1 is the most compressible and softest system. Besides, based on the data of the cohesion and interface energy, the most stable structure is the B1. However, these energy values are almost the same for all models. Then, the study of the electronic properties of the interface models gives as a result that the composite acquires a metal-like behavior. The reason is that electrons of the metal phase populates the bandgap of the insulator. The analysis of the electron density suggest the formation of directional bonds with some covalent character.

Ongoing studies are considering multilayer interface models with a different ratio thickness of the γ -Al₂O₃ and α -Al. Finally, as a concluding remark, the theoretical research of interfaces gives exciting results of novelty materials properties that can be corroborated by experiments or vice versa, this is the reason of the relevancy of DFT.

Appendix A

Results of DFT calculations

α -Al PDOS

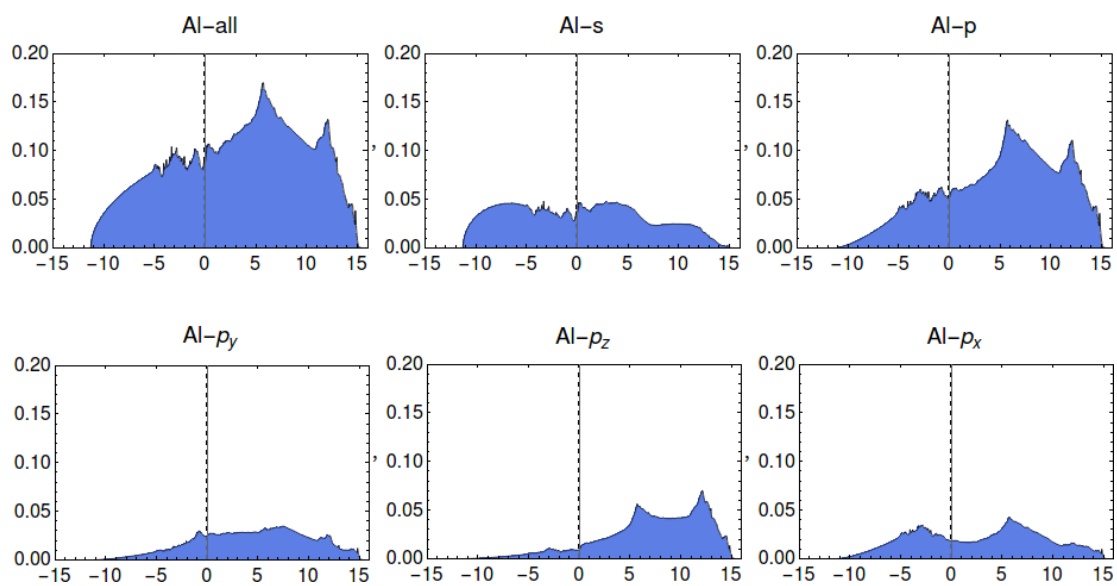
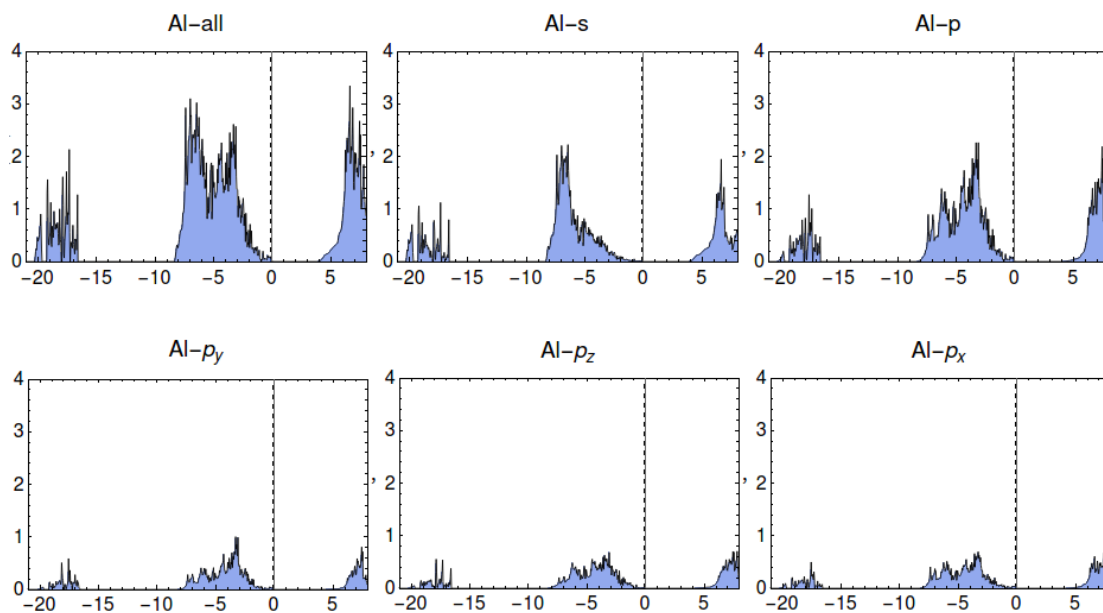


Figure A.1: PDOS of the α -Al.

γ -Al₂O₃ PDOSFigure A.2: PDOS of the γ -Al₂O₃, Al contribution.

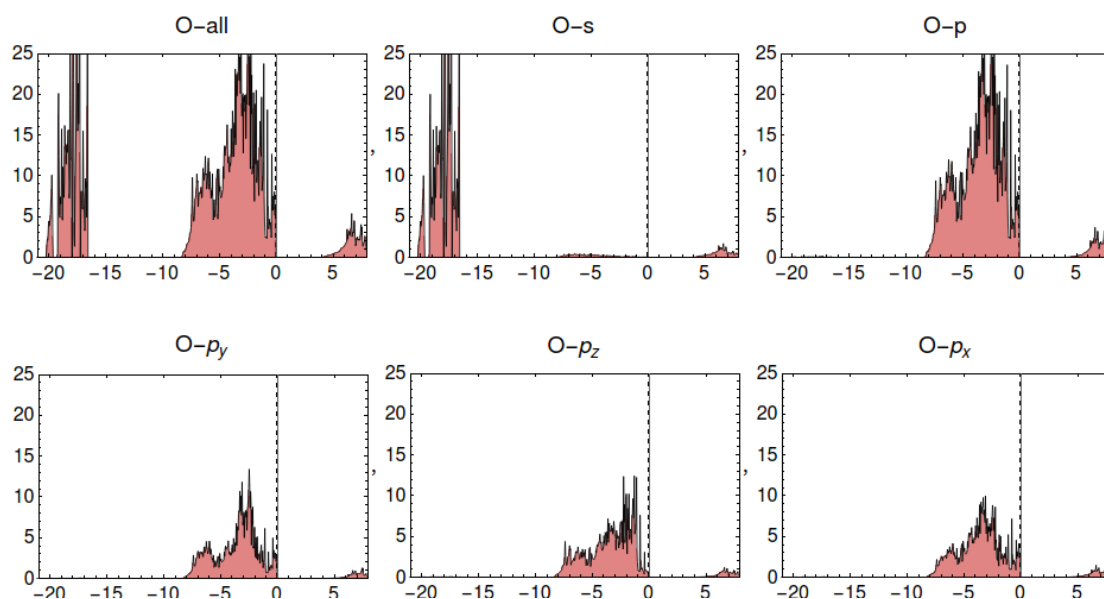
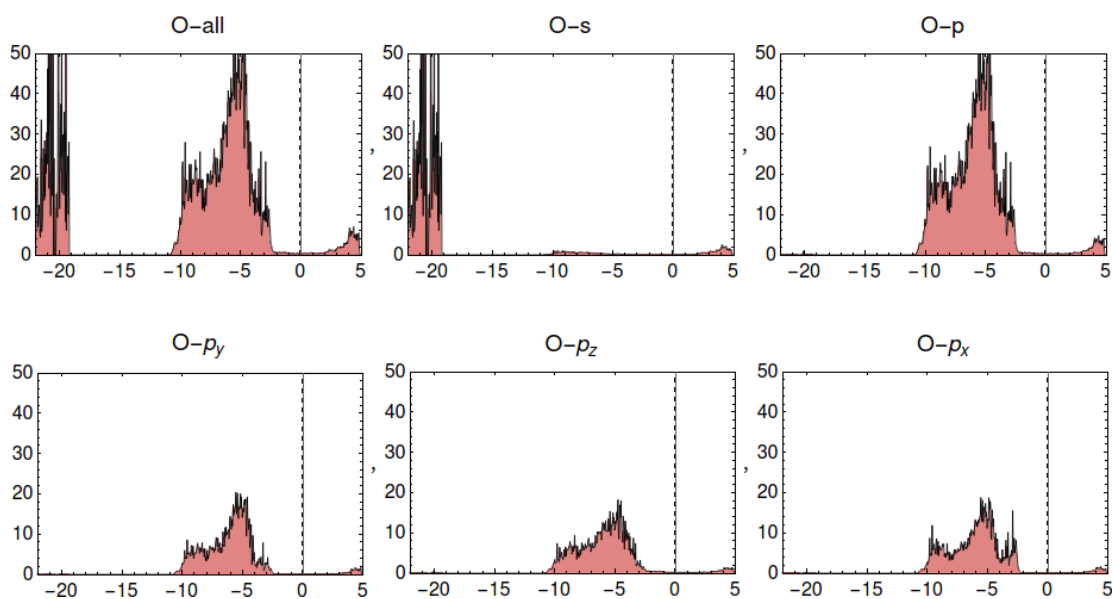
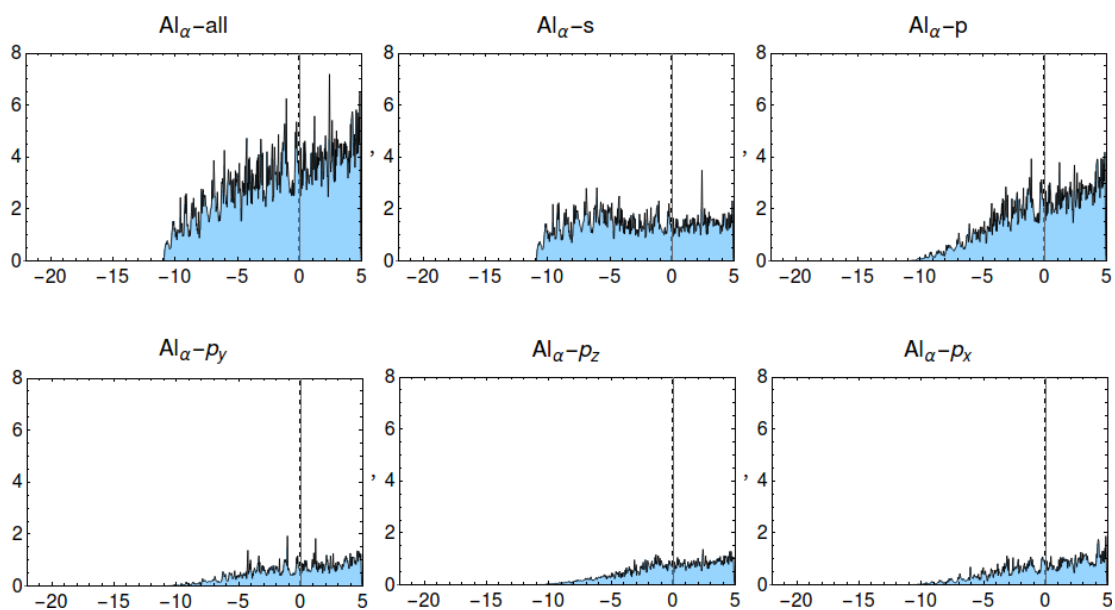
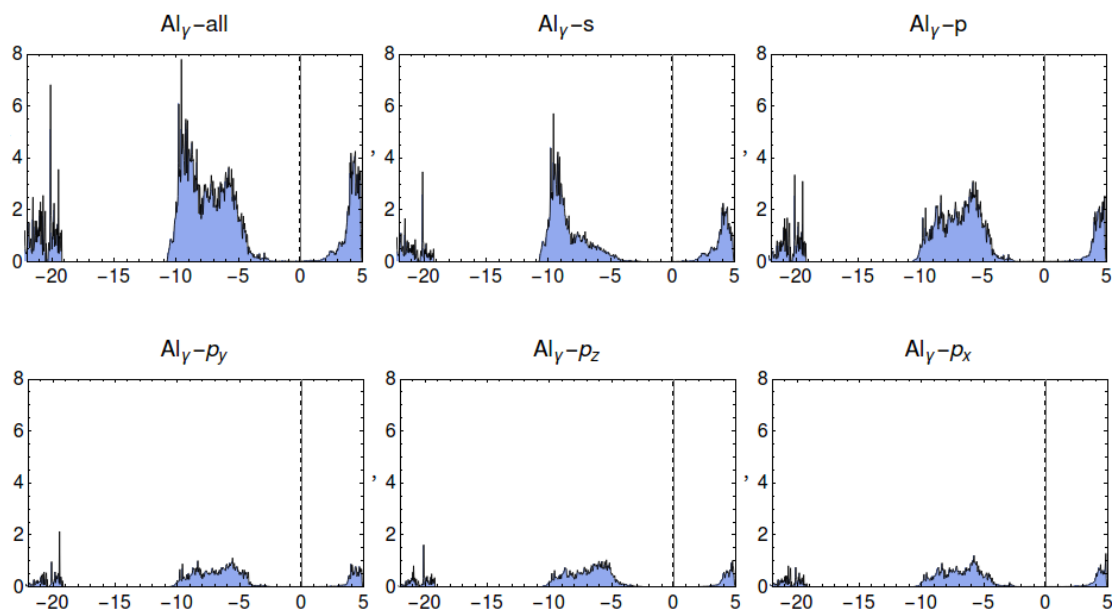
Figure A.3: PDOS of the $\gamma\text{-Al}_2\text{O}_3$, O contribution.**Model A1 PDOS**

Figure A.4: PDOS of the interface A1, O contribution.

Figure A.5: PDOS of the interface Al, Al_α contribution.Figure A.6: PDOS of the interface Al, Al_γ contribution.

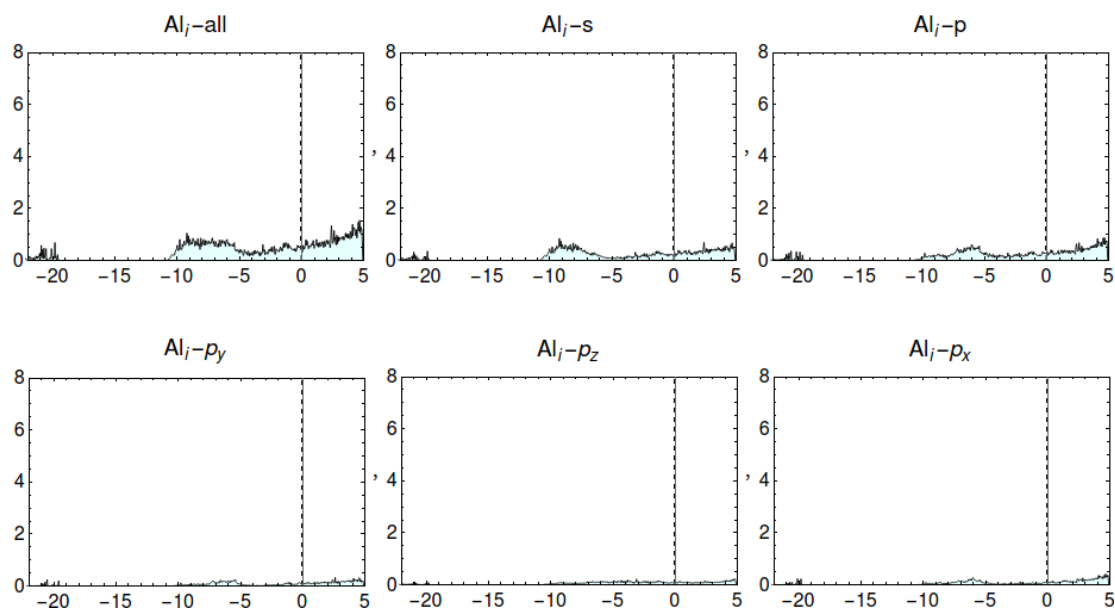
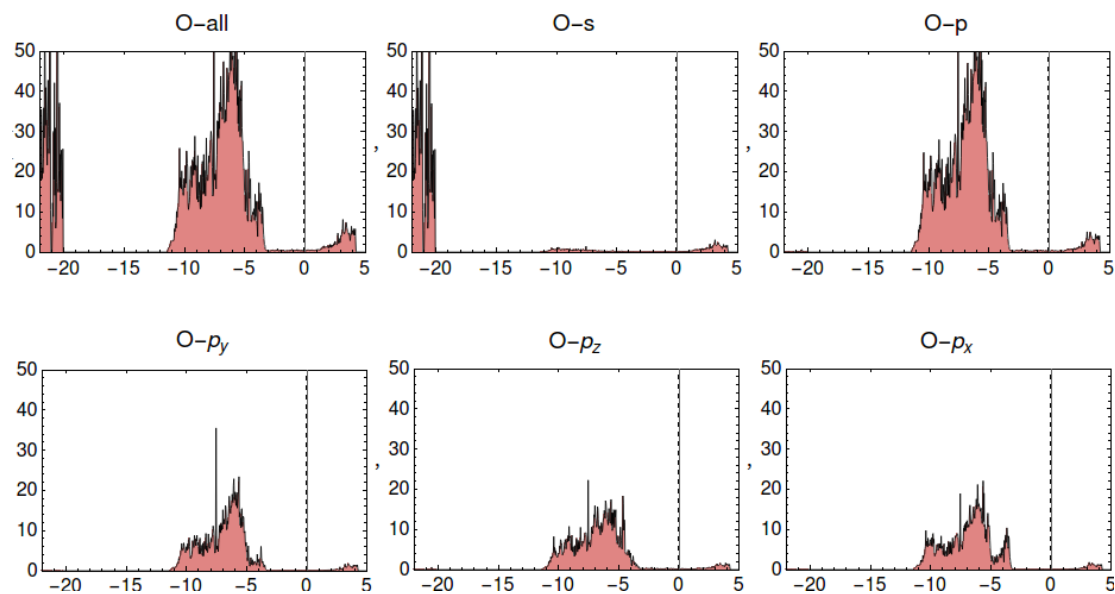
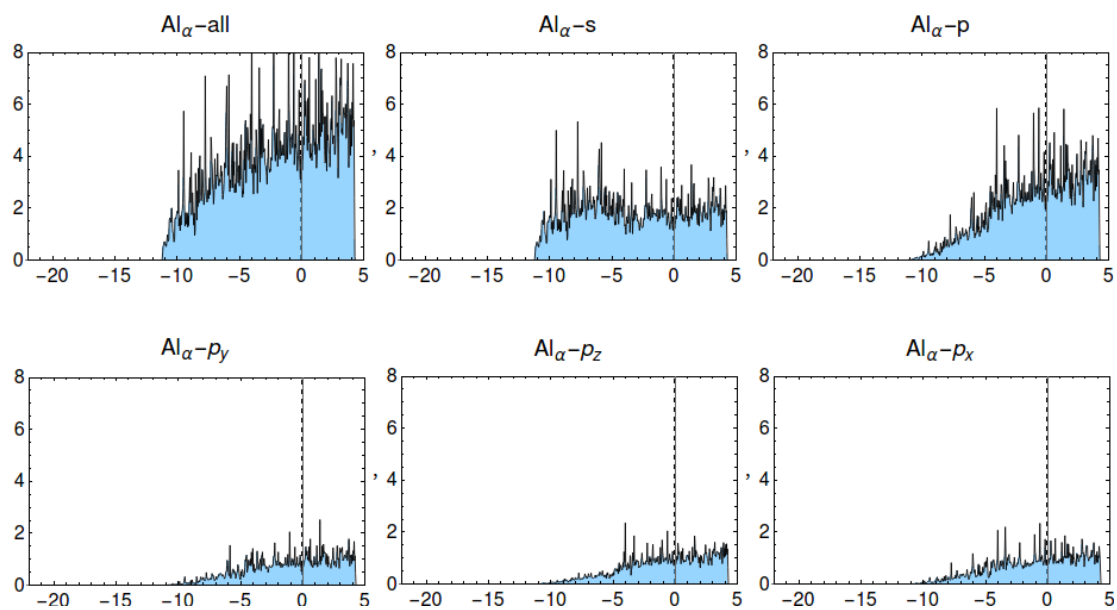
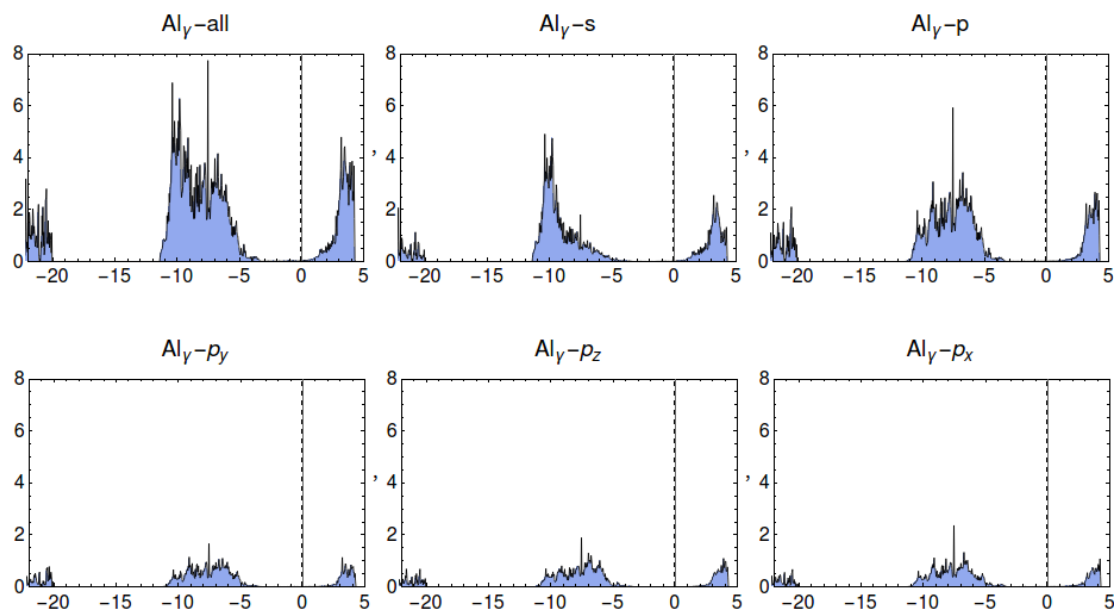
Figure A.7: PDOS of the interface A1, Al_i contribution.**Model A2 PDOS**

Figure A.8: PDOS of the interface A2, O contribution.

Figure A.9: PDOS of the interface A2, Al_α contribution.Figure A.10: PDOS of the interface A2, Al_γ contribution.

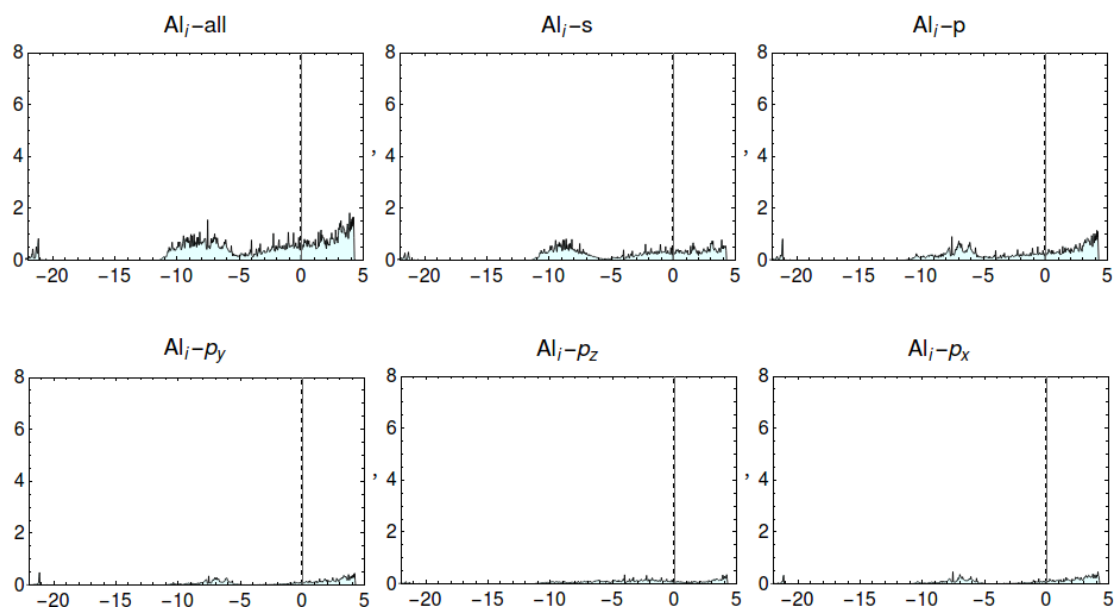
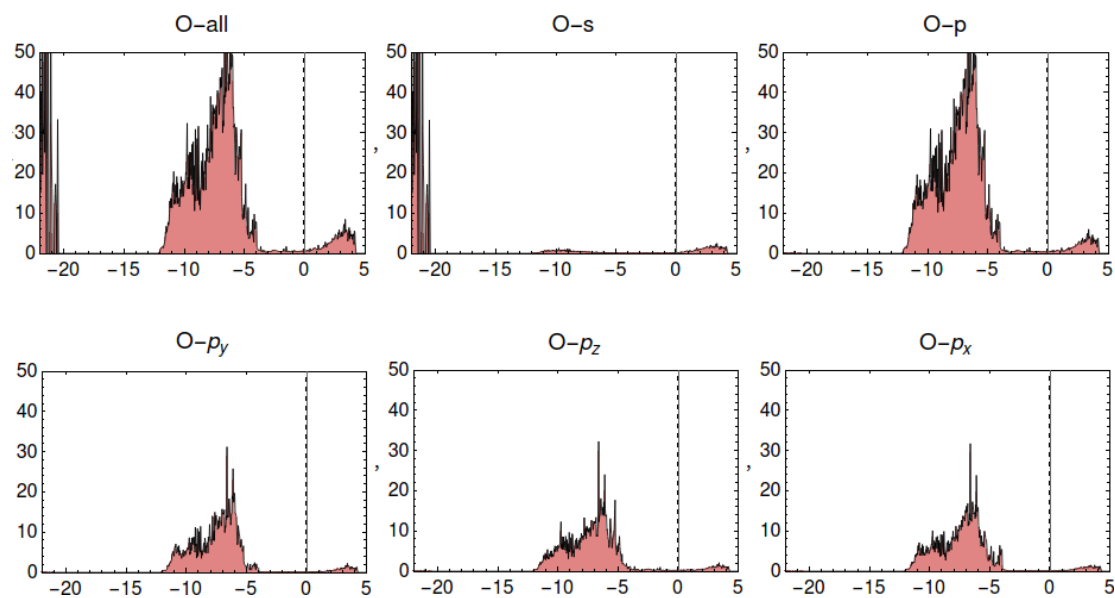
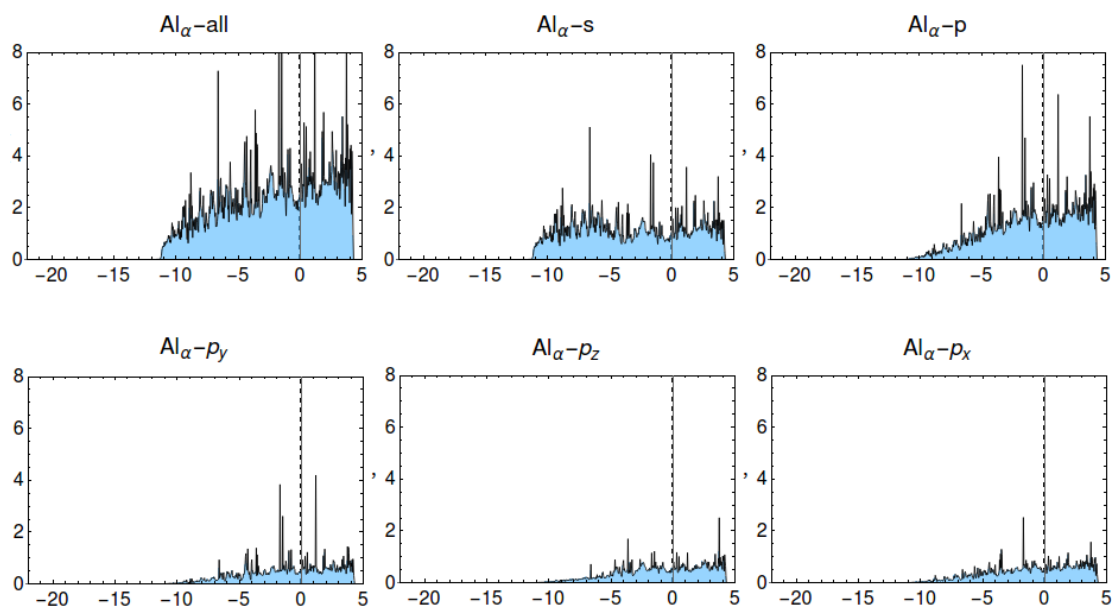
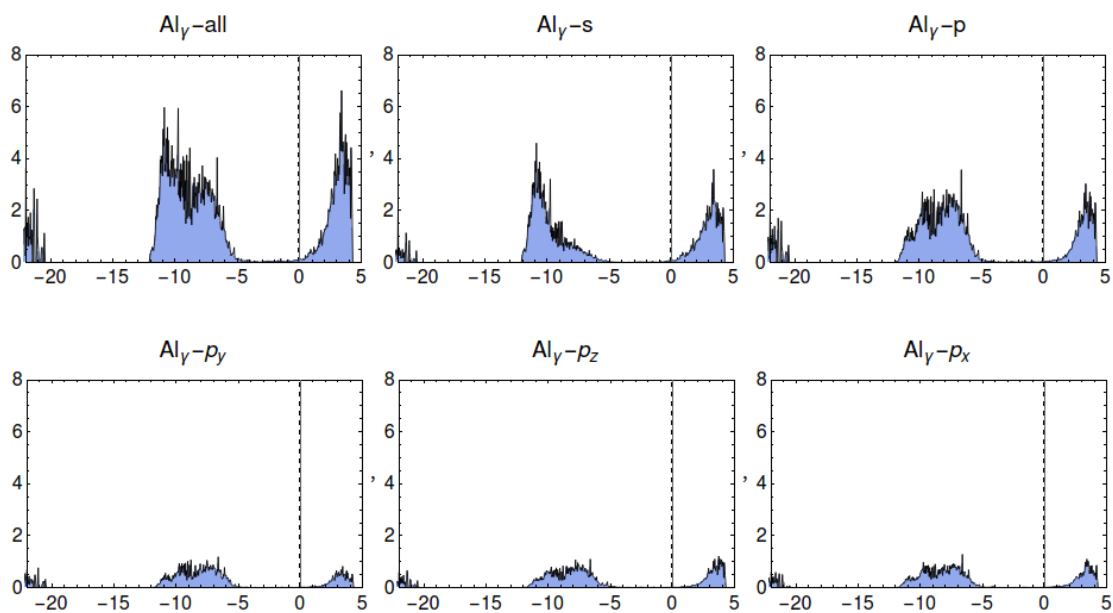
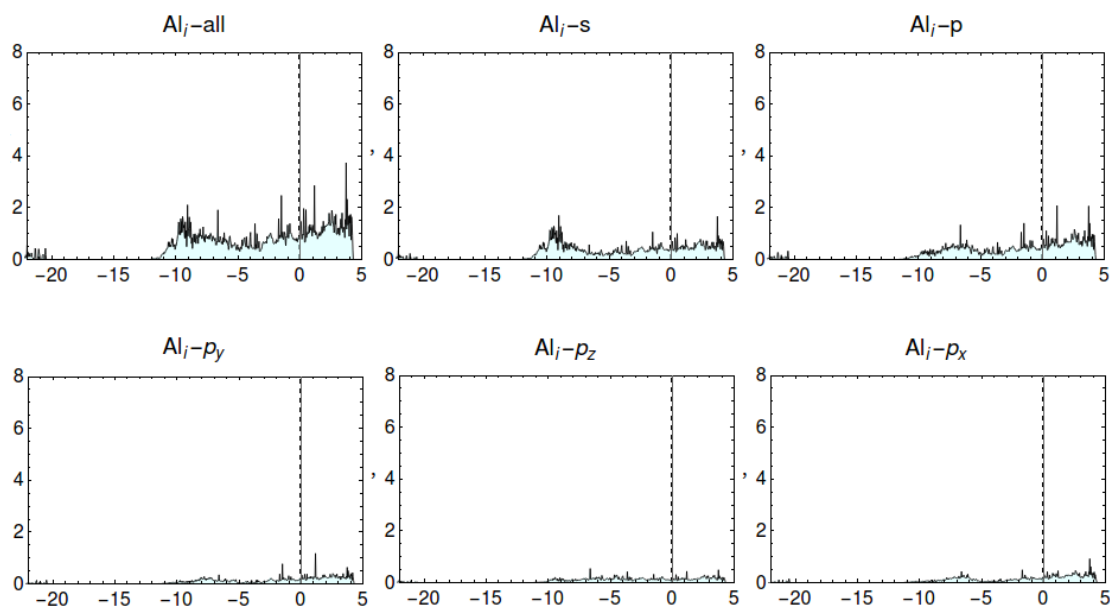
Figure A.11: PDOS of the interface A2, Al_i contribution.**Model B1 PDOS**

Figure A.12: PDOS of the interface B1, O contribution.

Figure A.13: PDOS of the interface B1, Al_α contribution.Figure A.14: PDOS of the interface B1, Al_γ contribution.

Figure A.15: PDOS of the interface B1, Al_i contribution.

Model B2 PDOS

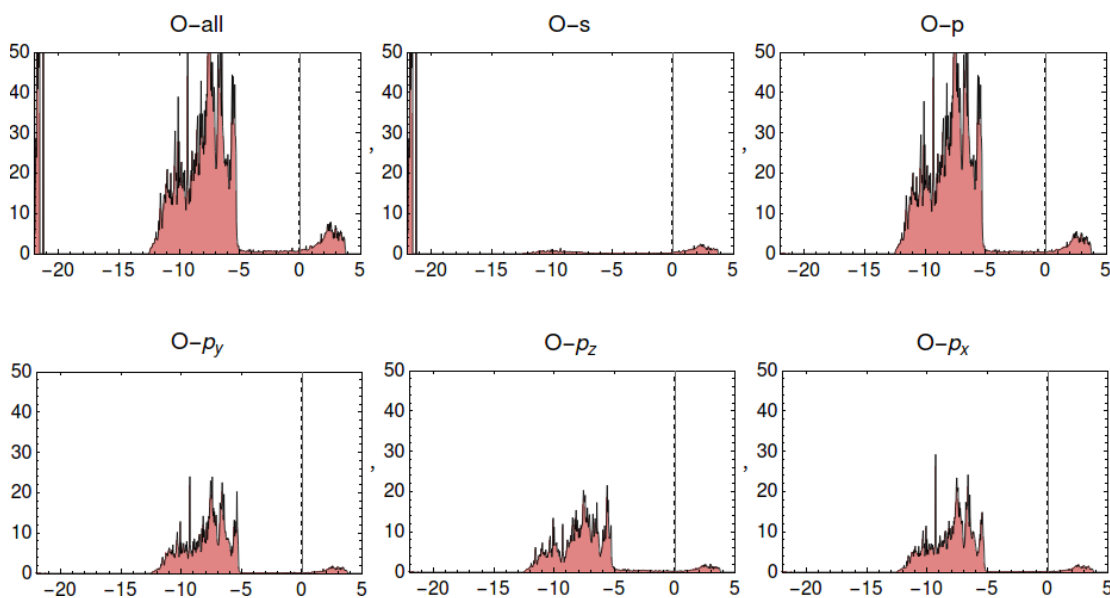
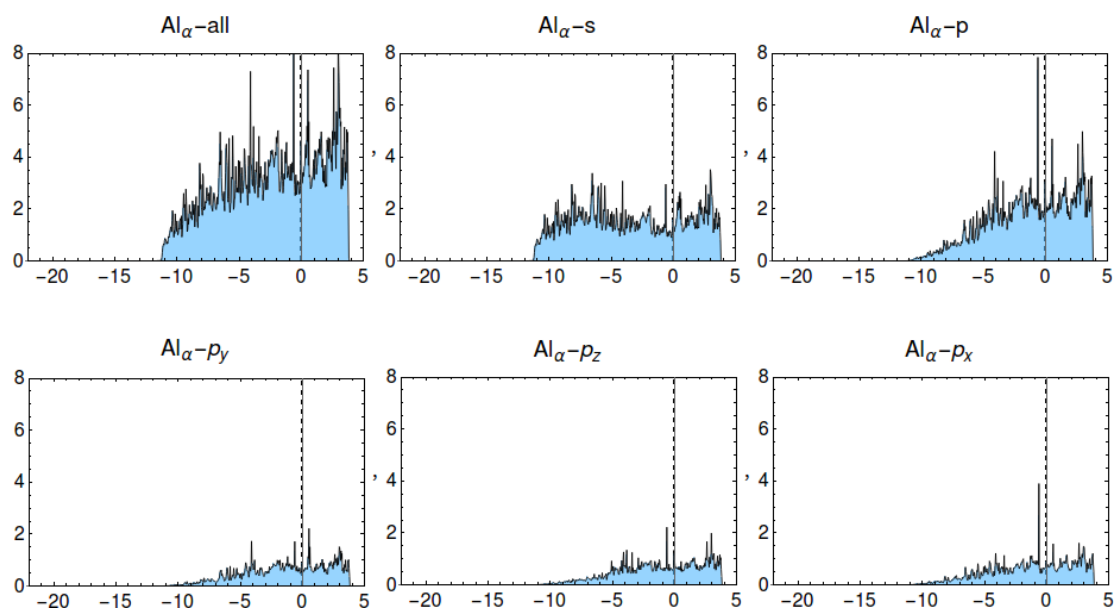
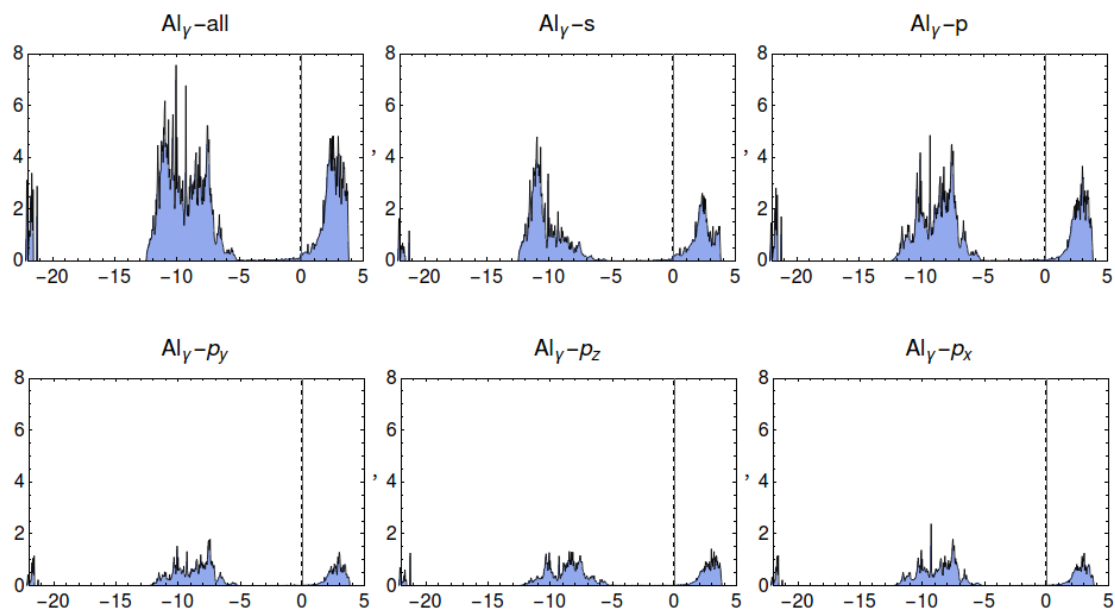
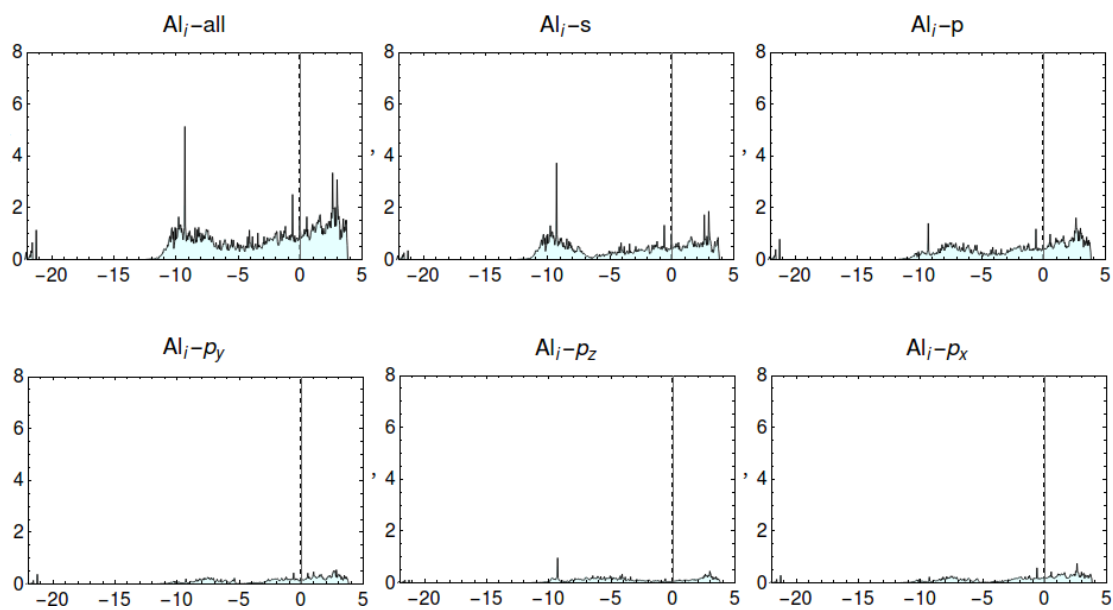


Figure A.16: PDOS of the interface B2, O contribution.

Figure A.17: PDOS of the interface B2, Al_α contribution.Figure A.18: PDOS of the interface B2, Al_γ contribution.

Figure A.19: PDOS of the interface B2, Al_i contribution.

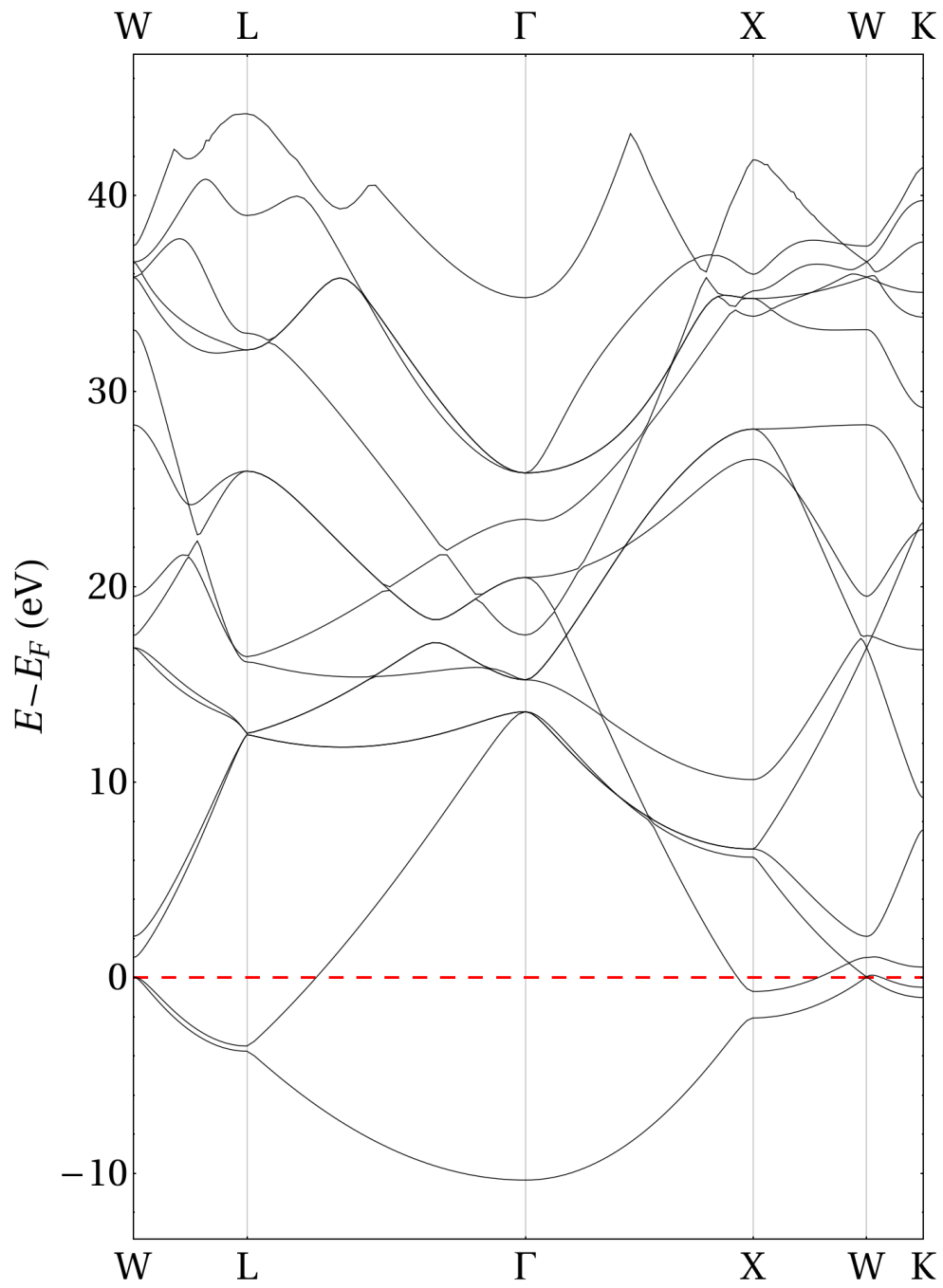


Figure A.20: Band structure α -Al, the Fermi level represented as a red dashed line.

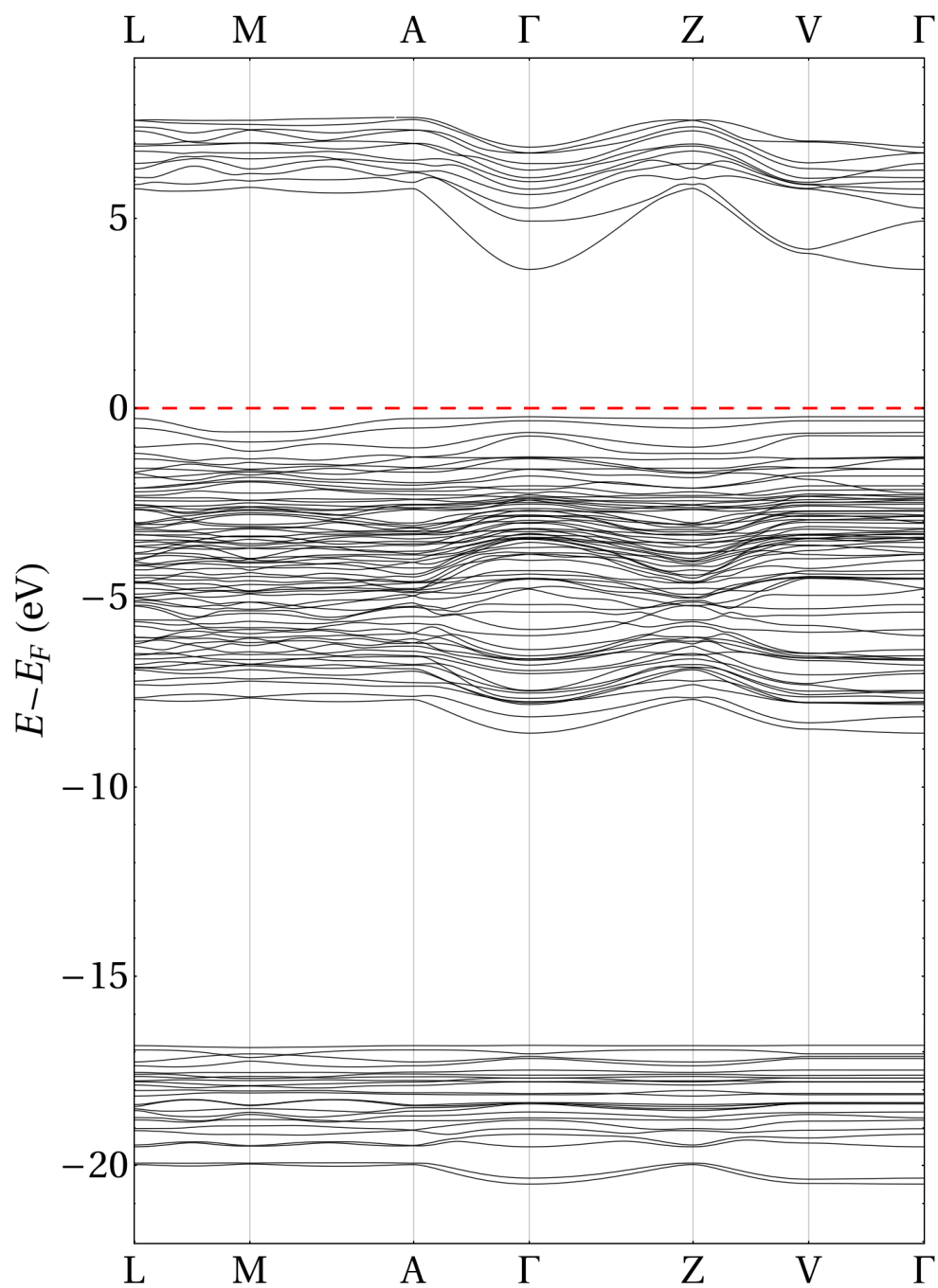


Figure A.21: Band structure $\gamma\text{-Al}_2\text{O}_3$, the Fermi level represented as a red dashed line.

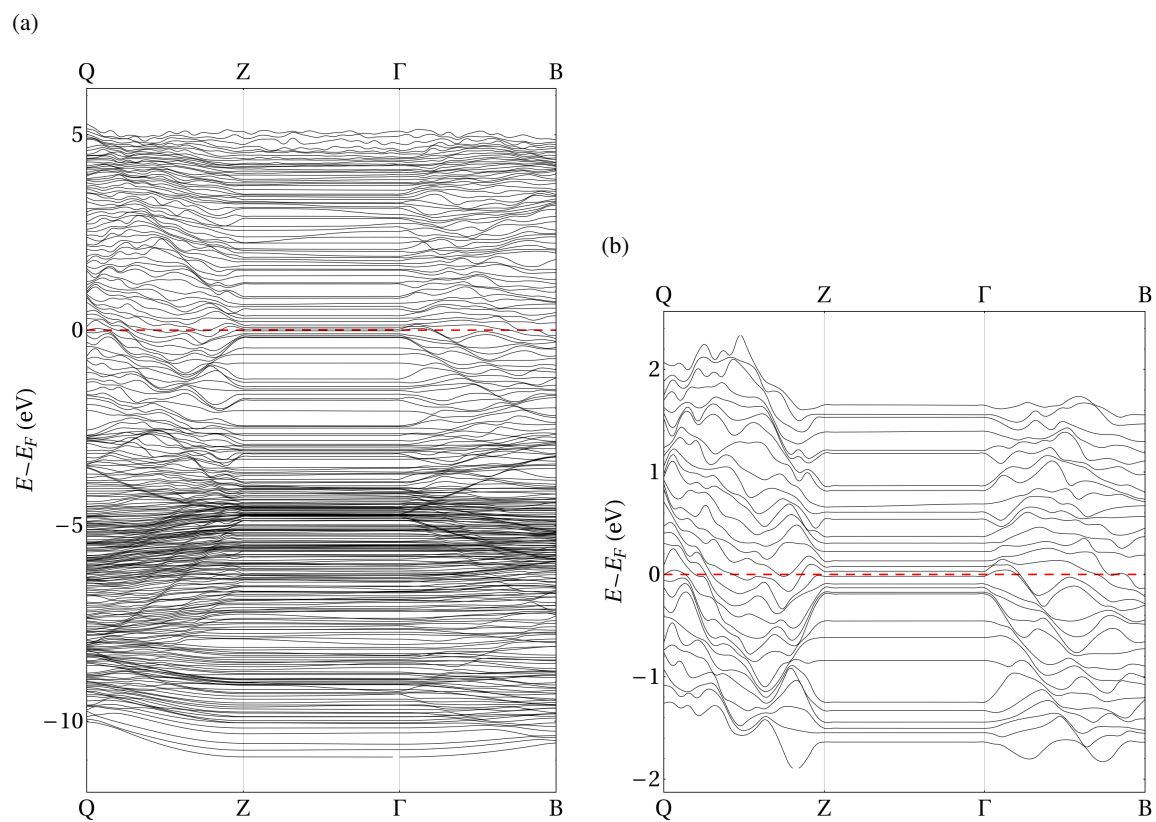


Figure A.22: Band structure of the final A1 interface model a) for the upper valence band and the conduction band and b) bands near the Fermi level represented as a red dashed line.

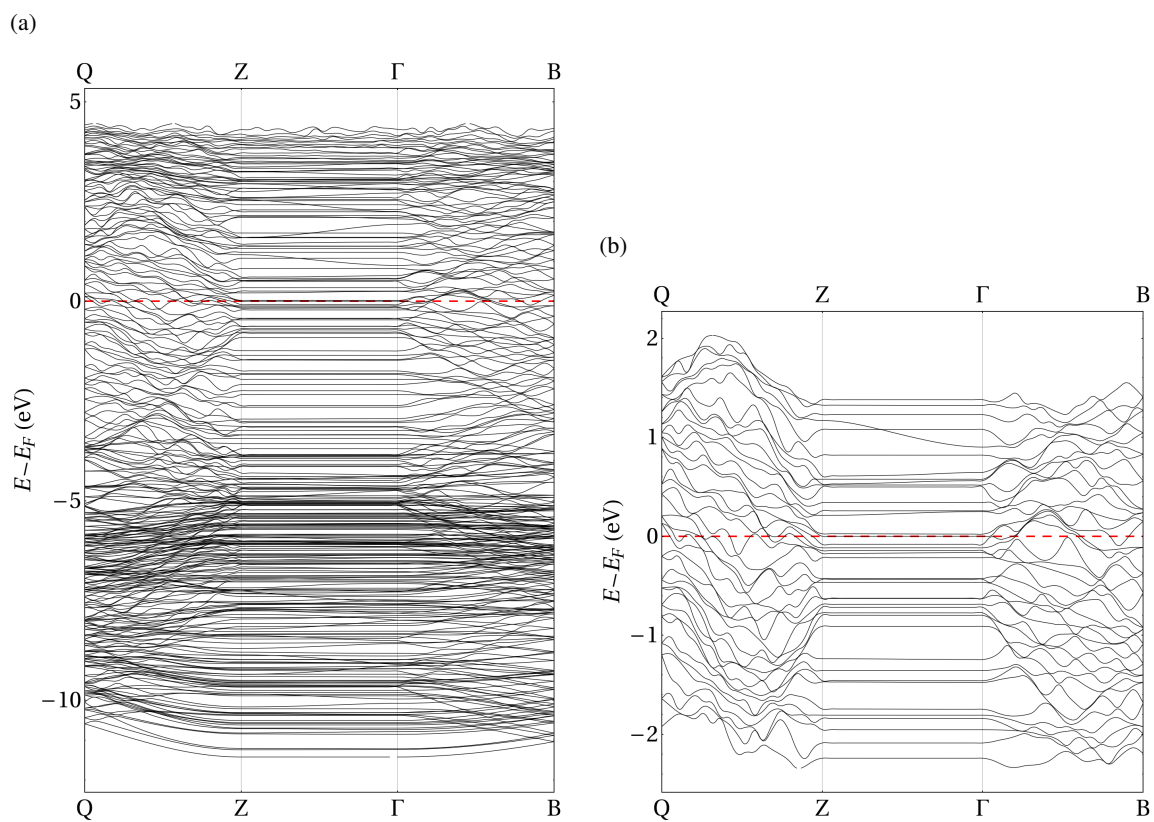


Figure A.23: Band structure of the final A2 interface a) for the upper valence band and the conduction band and b) bands near the Fermi level.

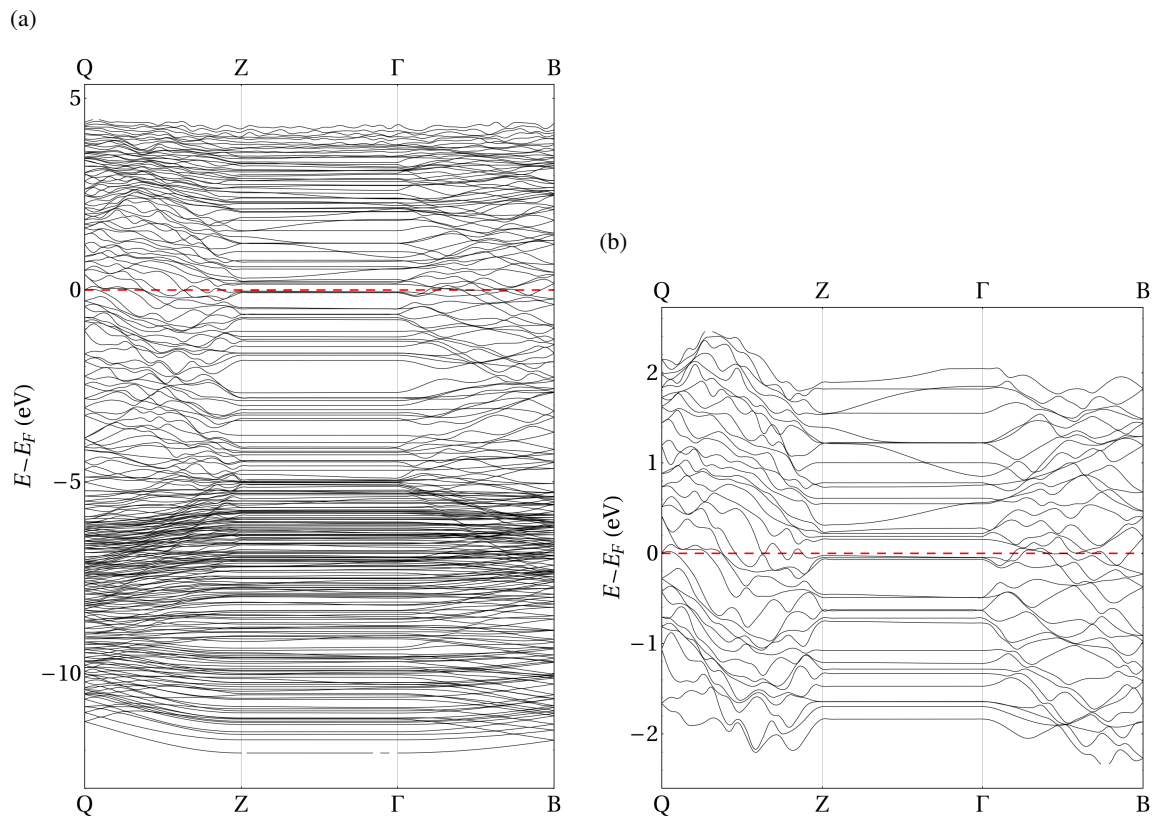


Figure A.24: Band structure of the final B1 interface a) for the upper valence band and the conduction band and b) bands near the Fermi level.

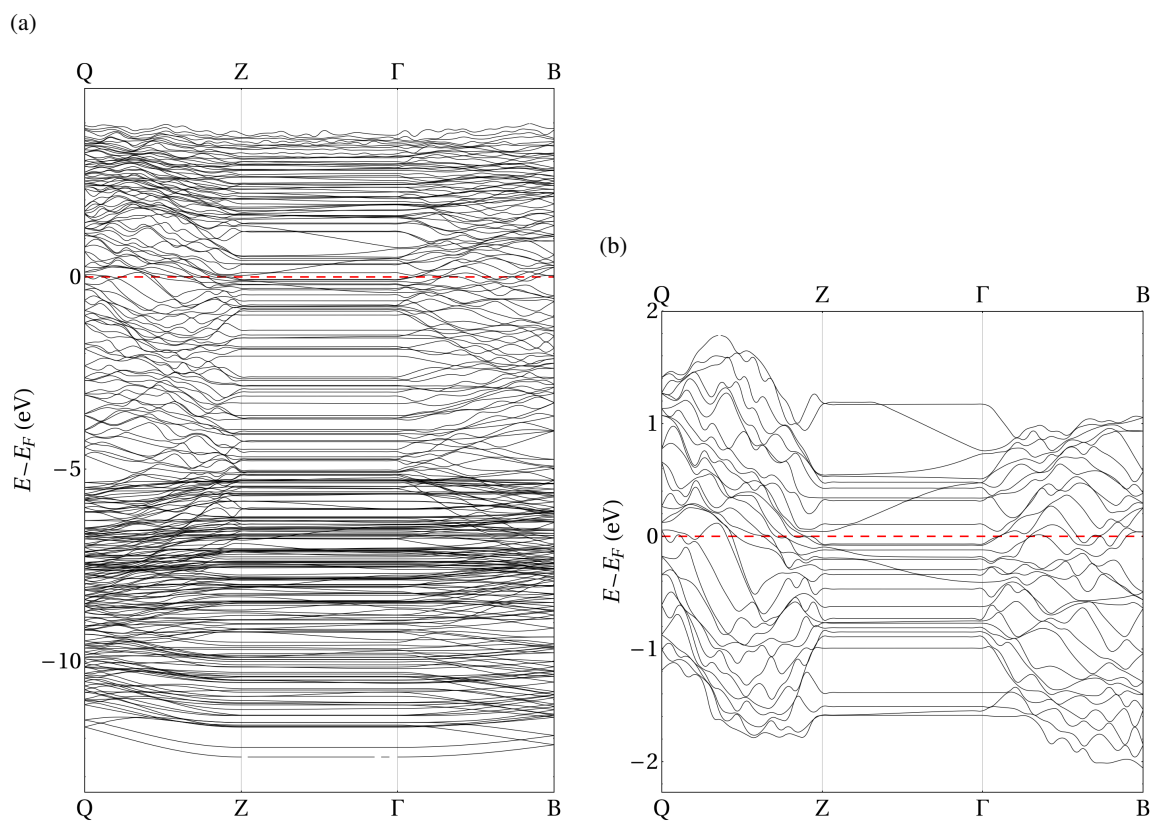


Figure A.25: Band structure of the final B2 interface a) for the upper valence band and the conduction band and b) bands near the Fermi level.

Bibliography

- [1] Chatain, D.,; Coudurier, L.,; Eustathopoulos, N., Wetting and interfacial bonding in ionocovalent oxide-liquid metal systems. *Rev. Phys. Appl. (Paris)* **1988**, *23*, 1055–1064.
- [2] Humenik Jr, M.; Kingery, W. D. Metal-Ceramic Interactions: III, Surface Tension and Wettability of Metal-Ceramic Systems. *Journal of the American Ceramic Society* **1954**, *37*, 18–23.
- [3] Finnis, M. W. The theory of metal - ceramic interfaces. *Journal of Physics: Condensed Matter* **1996**, *8*, 5811–5836.
- [4] Rühle, M.; Evans, A. G.; Hirth, J. P.; Ashby, M. F. *Metal-Ceramic Interfaces: Proceedings of an International Workshop*; Elsevier Science: Kent, 2014; OCLC: 1040602714.
- [5] Lyle, J. P.; Granger, D. A.; Sanders, R. E. In *Ullmann's Encyclopedia of Industrial Chemistry*; Wiley-VCH Verlag GmbH & Co. KGaA, Ed.; Wiley-VCH Verlag GmbH & Co. KGaA: Weinheim, Germany, 2000; p a01_481.
- [6] J. R. Davis & Associates,, ASM International,, Eds. *Aluminum and aluminum alloys*; ASM specialty handbook; ASM International: Materials Park, OH, 1993.
- [7] Leskelä, M.; Ritala, M. Atomic layer deposition (ALD): from precursors to thin film structures. *Thin solid films* **2002**, *409*, 138–146.
- [8] Raybaud, P.; Digne, M.; Iftimie, R.; Wellens, W.; Euzen, P.; Toulhoat, H. Morphology and Surface Properties of Boehmite (γ -AlOOH): A Density Functional Theory Study. *Journal of Catalysis* **2001**, *201*, 236–246.
- [9] El-Shaarawy, M.; Bayoumy, W. Doping effect on the electrical properties of amorphous Al₂O₃. *Materials Chemistry and Physics* **2003**, *78*, 405–411.

- [10] Goswami, R.; Pande, C.; Bernstein, N.; Johannes, M.; Baker, C.; Villalobos, G. A high degree of enhancement of strength of sputter deposited Al/Al₂O₃ multilayers upon post annealing. *Acta Materialia* **2015**, *95*, 378 – 385.
- [11] Pilania, G.; Thijsse, B. J.; Hoagland, R. G.; Lazić, I.; Valone, S. M.; Liu, X.-Y. Revisiting the Al/Al₂O₃ interface: coherent interfaces and misfit accommodation. *Scientific reports* **2014**, *4*, 4485.
- [12] Ayoola, H. O.; House, S. D.; Bonifacio, C. S.; Kisslinger, K.; Saidi, W. A.; Yang, J. C. Evaluating the accuracy of common γ -Al₂O₃ structure models by selected area electron diffraction from high-quality crystalline γ -Al₂O₃. *Acta Materialia* **2020**, *182*, 257–266.
- [13] Payne, M. C.; Teter, M. P.; Allan, D. C.; Arias, T. A.; Joannopoulos, J. D. Iterative minimization techniques for ab initio total-energy calculations: molecular dynamics and conjugate gradients. *Rev. Mod. Phys.* **1992**, *64*, 1045–1097.
- [14] Saiz, E.; Tomsia, A.; Sukanuma, K. Wetting and strength issues at Al/ α -alumina interfaces. *Journal of the European Ceramic Society* **2003**, *23*, 2787 – 2796, Ceramic and Metal Interfaces.
- [15] Smrčok, L.; Langer, V.; Křesťan, J. γ -Alumina: a single-crystal X-ray diffraction study. *Acta Crystallographica Section C Crystal Structure Communications* **2006**, *62*, i83–i84.
- [16] Digne, M.; Sautet, P.; Raybaud, P.; Euzen, P.; Toulhoat, H. Use of DFT to achieve a rational understanding of acid–basic properties of γ -alumina surfaces. *Journal of Catalysis* **2004**, *226*, 54 – 68.
- [17] Paglia, G.; Buckley, C. E.; Rohl, A. L.; Hunter, B. A.; Hart, R. D.; Hanna, J. V.; Byrne, L. T. Tetragonal structure model for boehmite-derived γ -alumina. *Phys. Rev. B* **2003**, *68*, 144110.
- [18] Pinto, H. P.; Nieminen, R. M.; Elliott, S. D. Ab initio study of γ -Al₂O₃ surfaces. *Phys. Rev. B* **2004**, *70*, 125402.
- [19] Kovarik, L.; Genc, A.; Wang, C.; Qiu, A.; Peden, C. H.; Szanyi, J.; Kwak, J. H. Tomography and high-resolution electron microscopy study of surfaces and porosity in a plate-like γ -Al₂O₃. *The Journal of Physical Chemistry C* **2013**, *117*, 179–186.
- [20] Schrödinger, E. An Undulatory Theory of the Mechanics of Atoms and Molecules. *Phys. Rev.* **1926**, *28*, 1049–1070.

- [21] Born, M.; Oppenheimer, R. Zur Quantentheorie der Molekeln. *Ann. Phys.* **1927**, *20*, 467.
- [22] Hartree, D. R. The Wave Mechanics of an Atom with a Non-Coulomb Central Field. Part I. Theory and Methods. *Math. Proc. Cambridge* **1928**, *24*, 89–110.
- [23] Slater, J. C. The Theory of Complex Spectra. *Physical Review* **1929**, *34*, 1293–1322.
- [24] Fock, V. Näherungsmethode zur Lösung des quantenmechanischen Mehrkörperproblems. *Z. Phys.* **1930**, *61*, 126–148.
- [25] Hohenberg, P.; Kohn, W. Inhomogeneous Electron Gas. *Phys. Rev.* **1964**, *136*, B864–B871.
- [26] Kohn, W.; Sham, L. J. Self-Consistent Equations Including Exchange and Correlation Effects. *Phys. Rev.* **1965**, *140*, A1133–A1138.
- [27] Sholl, D. S.; Steckel, J. A. *Density functional theory: a practical introduction*; Wiley: Hoboken, N.J, 2009; OCLC: ocn245025462.
- [28] Giustino, F. *Materials modelling using density functional theory: properties and predictions*, 1st ed.; Oxford University Press: Oxford, 2014; OCLC: ocn870986749.
- [29] Perdew, J. P.; Zunger, A. Self-interaction correction to density-functional approximations for many-electron systems. *Phys. Rev. B* **1981**, *23*, 5048–5079.
- [30] Perdew, J. P.; Wang, Y. Accurate and simple analytic representation of the electron-gas correlation energy. *Phys. Rev. B* **1992**, *45*, 13244–13249.
- [31] Jones, R. O.; Gunnarsson, O. The density functional formalism, its applications and prospects. *Rev. Mod. Phys.* **1989**, *61*, 689–746.
- [32] Sham, L. J.; Schlüter, M. Density-Functional Theory of the Energy Gap. *Phys. Rev. Lett.* **1983**, *51*, 1888–1891.
- [33] Perdew, J. P.; Burke, K.; Ernzerhof, M. Generalized Gradient Approximation Made Simple. *Phys. Rev. Lett.* **1996**, *77*, 3865–3868.
- [34] Perdew, J. P.; Burke, K.; Ernzerhof, M. Generalized Gradient Approximation Made Simple [Phys. Rev. Lett. *77*, 3865 (1996)]. *Phys. Rev. Lett.* **1997**, *78*, 1396–1396.

- [35] Preciado, M. R.; Mowbray, D. Theoretical optical absorption and electron energy loss spectroscopy using LCAO-TDDFT-K- Ω of chlorophyll and carbon nanotubes. B.S. Thesis, Universidad de Investigación de Tecnología Experimental Yachay, 2019.
- [36] Perdew, J. P.; Ruzsinszky, A.; Csonka, G. I.; Vydrov, O. A.; Scuseria, G. E.; Constantin, L. A.; Zhou, X.; Burke, K. Restoring the Density-Gradient Expansion for Exchange in Solids and Surfaces. *Phys. Rev. Lett.* **2008**, *100*, 136406.
- [37] Kittel, C. *Introduction to Solid State Physics*, 8th ed.; Wiley, 2004.
- [38] Ashcroft, N. W.; Mermin, N. D. *Solid State Physics*; Holt-Saunders, 1976.
- [39] Cohen, M. L.; Heine, V. In *The Fitting of Pseudopotentials to Experimental Data and Their Subsequent Application*; Ehrenreich, H., Seitz, F., Turnbull, D., Eds.; Solid State Physics; Academic Press, 1970; Vol. 24; pp 37 – 248.
- [40] Yin, M. T.; Cohen, M. L. Theory of ab initio pseudopotential calculations. *Phys. Rev. B* **1982**, *25*, 7403–7412.
- [41] Hafner, J. *Ab-initio* simulations of materials using VASP: Density-functional theory and beyond. *Journal of Computational Chemistry* **2008**, *29*, 2044–2078.
- [42] Louie, S. G.; Froyen, S.; Cohen, M. L. Nonlinear ionic pseudopotentials in spin-density-functional calculations. *Phys. Rev. B* **1982**, *26*, 1738–1742.
- [43] Blöchl, P. E. Projector augmented-wave method. *Phys. Rev. B* **1994**, *50*, 17953–17979.
- [44] Kresse, G.; Joubert, D. From ultrasoft pseudopotentials to the projector augmented-wave method. *Phys. Rev. B* **1999**, *59*, 1758–1775.
- [45] Hellmann, H. Zur Rolle der kinetischen Elektronenenergie für die zwischenatomaren Kräfte. *Zeitschrift für Physik* **1933**, *85*, 180–190.
- [46] Feynman, R. P. Forces in Molecules. *Phys. Rev.* **1939**, *56*, 340–343.
- [47] Car, R.; Parrinello, M. Unified Approach for Molecular Dynamics and Density-Functional Theory. *Phys. Rev. Lett.* **1985**, *55*, 2471–2474.
- [48] Kresse, G.; Hafner, J. Ab initio molecular dynamics for liquid metals. *Phys. Rev. B* **1993**, *47*, 558–561.

- [49] Kresse, G.; Hafner, J. Ab initio molecular-dynamics simulation of the liquid-metal–amorphous-semiconductor transition in germanium. *Phys. Rev. B* **1994**, *49*, 14251–14269.
- [50] Kresse, G.; Furthmüller, J. Efficiency of ab-initio total energy calculations for metals and semiconductors using a plane-wave basis set. *Computational Materials Science* **1996**, *6*, 15–50.
- [51] Kresse, G.; Furthmüller, J. Efficient iterative schemes for ab initio total-energy calculations using a plane-wave basis set. *Phys. Rev. B* **1996**, *54*, 11169–11186.
- [52] Kresse, G.; Marsman, M.; Furthmüller, J. *VASP the GUIDE*; 2018.
- [53] Krebs, E.; Daudin, A.; Raybaud, P., A DFT Study of CoMoS and NiMoS Catalysts: from Nano-Crystallite Morphology to Selective Hydrodesulfurization. *Oil & Gas Science and Technology - Rev. IFP* **2009**, *64*, 707–718.
- [54] Trueba, M.; Trasatti, S. P. γ -Alumina as a Support for Catalysts: A Review of Fundamental Aspects. *European Journal of Inorganic Chemistry* **2005**, *2005*, 3393–3403.
- [55] Lepot, N.; Bael, M. V.; den Rul, H. V.; D’Haen, J.; Peeters, R.; Franco, D.; Mullens, J. Synthesis of platelet-shaped boehmite and γ -alumina nanoparticles via an aqueous route. *Ceramics International* **2008**, *34*, 1971 – 1974.
- [56] Shayesteh, M.; Shafiee Afarani, M.; Samimi, A.; Khorram, M. Preparation of γ -Al₂O₃ and prioritization of affecting factors on the crystallite size using Taguchi method. *Transp Phenom Nano Micro Scales* **2013**, *1*, 45–52.
- [57] Birch, F. Finite Elastic Strain of Cubic Crystals. *Phys. Rev.* **1947**, *71*, 809–824.
- [58] Murnaghan, F. D. The Compressibility of Media under Extreme Pressures. *Proceedings of the National Academy of Sciences* **1944**, *30*, 244–247.
- [59] Knoop, F.; Peters, C.; Emerson, W. A sensitive pyramidal-diamond tool for indentation measurements. *Journal of Research of the National Bureau of Standards* **1939**, *23*, 39.
- [60] Pelleg, J. *Mechanical Properties of Ceramics*; Springer International Publishing: Cham, 2014; Vol. 213; pp 1–112.

- [61] Smith, R. L.; Sandly, G. An accurate method of determining the hardness of metals, with particular reference to those of a high degree of hardness. *Proceedings of the Institution of Mechanical Engineers* **1922**, *102*, 623–641.
- [62] Marinescu, I. D.; Rowe, B.; Ling, Y.; Wobker, H. G. In *Handbook of Ceramics Grinding and Polishing*; Marinescu, I. D., Doi, T. K., Uhlmann, E., Eds.; William Andrew Publishing: Boston, 2015; pp 67 – 132.
- [63] Li, K.; Wang, X.; Zhang, F.; Xue, D. Electronegativity Identification of Novel Superhard Materials. *Phys. Rev. Lett.* **2008**, *100*, 235504.
- [64] Lyakhov, A. O.; Oganov, A. R. Evolutionary search for superhard materials: Methodology and applications to forms of carbon and TiO₂. *Physical Review B* **2011**, *84*.
- [65] Brown, I. D. Chemical and steric constraints in inorganic solids. *Acta Crystallographica Section B* **1992**, *48*, 553–572.
- [66] Sung, C.-M.; Sung, M. Carbon nitride and other speculative superhard materials. *Materials Chemistry and Physics* **1996**, *43*, 1 – 18.
- [67] Holt, J.; Ho, C.; Mindlin, H. *Structural Alloys Handbook*; CINDAS/Purdue University, 1996.
- [68] Leger, J.; Haines, J.; Schmidt, M.; Petitet, J.; Pereira, A.; Da Jornada, J. Discovery of hardest known oxide. *Nature* **1996**, *383*, 401–401.
- [69] Mizutani, U.; Inukai, M.; Sato, H.; Zijlstra, E. In *Physical Metallurgy (Fifth Edition)*, fifth edition ed.; Laughlin, D. E., Hono, K., Eds.; Elsevier: Oxford, 2014; pp 103 – 202.
- [70] Butler, K. T.; Sai Gautam, G.; Canepa, P. Designing interfaces in energy materials applications with first-principles calculations. *npj Computational Materials* **2019**, *5*, 1–12.
- [71] Christensen, M.; Dudiy, S.; Wahnström, G. First-principles simulations of metal-ceramic interface adhesion: Co/WC versus Co/TiC. *Physical Review B* **2002**, *65*, 045408.
- [72] Gregersen, E., Ed. *The Britannica guide to matter*; Physics explained; Britannica Educational Pub. in association with Rosen Educational Services: New York, NY, 2011.
- [73] Mearini, G.; Hoffman, R. Tensile properties of aluminum/alumina multi-layered thin films. *Journal of electronic materials* **1993**, *22*, 623–629.

- [74] Ahuja, R.; Osorio-Guillén, J.; Almeida, J.; Holm, B.; Ching, W.-Y.; Johansson, B. Electronic and Optical Properties of γ -Al₂O₃ from Ab Initio Theory. *Journal of Physics: Condensed Matter* **2004**, *16*, 2891.
- [75] Dubrovinsky, L. S.; Saxena, S. K.; Lazor, P. High-pressure and high-temperature in situ X-ray diffraction study of iron and corundum to 68 GPa using an internally heated diamond anvil cell. *Physics and Chemistry of Minerals* **1998**, *25*, 434–441.
- [76] Kaxiras, E. *Atomic and electronic structure of solids*; Cambridge University Press: Cambridge, UK ; New York, 2003; OCLC: ocm50718056.
- [77] Persson, K. Materials Data on Al (SG:225) by Materials Project. 2015; An optional note.
- [78] Jain, A.; Ong, S. P.; Hautier, G.; Chen, W.; Richards, W. D.; Dacek, S.; Cholia, S.; Gunter, D.; Skinner, D.; Ceder, G.; Persson, K. a. The Materials Project: A materials genome approach to accelerating materials innovation. *APL Materials* **2013**, *1*, 011002.
- [79] Samain, L.; Jaworski, A.; Edén, M.; Ladd, D. M.; Seo, D.-K.; Garcia-Garcia, F. J.; Häussermann, U. Structural analysis of highly porous γ -Al₂O₃. *Journal of Solid State Chemistry* **2014**, *217*, 1 – 8.
- [80] Menéndez-Proupin, E.; Gutiérrez, G. Electronic properties of bulk γ -Al₂O₃. *Phys. Rev. B* **2005**, *72*, 035116.
- [81] Paglia, G.; Rohl, A. L.; Buckley, C. E.; Gale, J. D. Determination of the structure of γ -alumina from interatomic potential and first-principles calculations: The requirement of significant numbers of nonspinel positions to achieve an accurate structural model. *Phys. Rev. B* **2005**, *71*, 224115.
- [82] French, R. H. Electronic band structure of Al₂O₃, with comparison to Al₂O and AlN. *Journal of the American Ceramic Society* **1990**, *73*, 477–489.

Abbreviations

- α -Al** α -Aluminum x, xi, 2, 3, 21, 23–25, 28, 31, 32, 35, 37–39, 41–47, 49, 51, 62
- α -Al/ γ -Al₂O₃** α -Aluminum/ γ -Alumina iii, xi, 2, 3, 21, 23, 25, 46, 49
- γ -Al₂O₃** γ -Alumina iii, ix–xi, 1–3, 17, 18, 21–25, 28, 31, 33–39, 41–49, 52, 53, 63
- BM** Birch-Murnaghan 24, 26
- BOA** Born-Oppenheimer approximation 6
- DFT** density-functional theory 2, 3, 7, 8, 14–16, 21, 49
- DOS** density of states 17, 35, 38, 41, 43, 45
- EOS** equation of states 26
- GGA** generalized gradient approximation 11, 12
- HF** Hartree-Fock 6, 7
- HK** Hohenberg and Kohn 7, 8
- KH** Knoop hardness 26, 27, 35
- KS** Kohn-Sham 8–10, 15–17
- LDA** local density approximation 11
- LVB** lower valence band 36, 38, 41, 43, 45
- MD** Molecular Dynamics 16
- PAW** projector augmented wave 14–16, 21

PBE Perdew, Burke and Ernzerhof 12

PDOS partial density of states 17, 38, 39, 41, 43, 45

UVB upper valence band 36

VASP Vienna *ab initio* simulation package 16, 17, 21

xc exchange and correlation 8–11, 21